



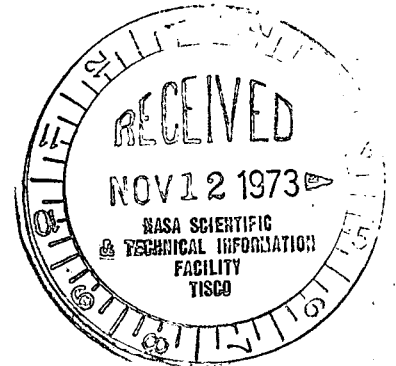
U.S. DEPARTMENT OF COMMERCE
National Technical Information Service
5285 Port Royal Road
Springfield, Virginia 22151

Date: November 9, 1973

Reply to
Attn of: 954.01

Subject: NASA Document Discrepancy Report 73-414

To: Mr. E. E. Baker
Deputy General Manager
Informatics TISCO
P. O. Box 33
College Park, Maryland 20740



Re: N73-29876

- ☐ 1. Page(s) are missing from microfiche and paper copy. Please provide a complete copy.
- ☐ 2. Portions of this document are illegible when reproduced. Please provide a reproducible copy.
- ☐ 3. A microfiche reproduction is not legible. The case file was not received. Please provide at least an acceptable microfiche.
- ☐ 4. Incorrectly priced at _____. It should be _____ for _____ pages. However, price will remain as announced in STAR.
- ☐ 5. Case file returned herewith. When correction has been made please return to NTIS or if corrections cannot be made note NASA records that the case file was returned.
- ☒ 6. Other:
Need a replacement. Card 2 of 2 runs off the edge of fiche.

11-14-73

Replacement fiche are attached.

Sincerely,

Barbara Reed

Phone: 703 -321-8517

BR/dip

E. E. Baker
E. E. Baker
Deputy General Manager

Response

Before	After
Issue Ch. of Status	Code
Code	Code
Comp. Ser.-No Act.	
Delay Ch. OF Status	
Post(ed) on Form 107	

PLEASE ATTACH COPY OF THIS LETTER WITH YOUR RESPONSE

2000

REPORT NO. GDC-DDE71-002, V. 1
CONTRACT NAS 8-26363

cg1

NASA-CR-124341) A METHOD FOR DETERMINING
THE RESPONSE OF SPACE SHUTTLE TO
ATMOSPHERIC TURBULENCE. VOLUME 1:
SPACE SHUTTLE (General Dynamics/Convair)
119 p HC \$8.00

N73-29876

Unclas

CSCL 22B G3/31 10479

A METHOD FOR DETERMINING THE RESPONSE OF SPACE SHUTTLE TO ATMOSPHERIC TURBULENCE

VOLUME I • SPACE SHUTTLE TURBULENCE RESPONSE

GENERAL DYNAMICS
Convair Aerospace Division

REPORT NO. GDC-DDE71-002

A METHOD FOR DETERMINING THE RESPONSE OF SPACE SHUTTLE TO ATMOSPHERIC TURBULENCE

VOLUME I • SPACE SHUTTLE TURBULENCE RESPONSE

1 November 1971

Prepared Under
Contract NAS8-26363

Submitted to
National Aeronautics and Space Administration
GEORGE C. MARSHALL SPACE FLIGHT CENTER
Huntsville, Alabama

Prepared by
CONVAIR AEROSPACE DIVISION OF GENERAL DYNAMICS
San Diego, California

Preceding page blank

FOREWORD

This report presents the first year results of an investigation being conducted under Contract NAS8-26363 for NASA George C. Marshall Space Flight Center under the technical direction of the Aero-Astro-dynamics Laboratory, Dynamics and Control Division. Dr. S. Winder is the technical monitor. The study is being performed by Convair Aerospace Division of General Dynamics under the direction of Mr. R. Huntington, project leader.

The author is indebted to Messrs. R. Peloubet and R. Haller for their assistance in developing the computer program and in performing the numerical analysis and to Mr. J. Kramer for converting the program to run on the Univac 1108 computer.

PRECEDING PAGE BLANK NOT FILMED

TABLE OF CONTENTS

Section		Page
1	INTRODUCTION	1-1
2	TECHNICAL DISCUSSION	2-1
	2.1 TURBULENCE RESPONSE	2-1
	2.1.1 Response to Random Disturbance	2-5
	2.1.2 Response to Discrete Disturbance	2-6
	2.2 STABILITY AUGMENTATION SYSTEM SIMULATION	2-7
	2.3 AERODYNAMICS	2-10
	2.4 PROPELLANT SLOSHING AND ENGINE DYNAMICS	2-15
3	COMPUTER PROGRAM DESCRIPTION	3-1
4	PRELIMINARY RESULTS OF SPACE SHUTTLE TURBULENCE RESPONSE ANALYSIS	4-1
	4.1 BOOSTER RETURN FLIGHT	4-1
	4.2 ASCENT FLIGHT	4-41
5	CONCLUSIONS AND RECOMMENDATIONS	5-1
6	REFERENCES	6-1

LIST OF FIGURES

Figure		Page
1-1	Evolution of Gust Design Criteria	1-2
1-2	Analytical Representation of Atmospheric Turbulence Spectra	1-3
2-1	SAS Block Diagram	2-8
2-2	Multiple Sensor SAS	2-9
2-3	$C_{N\beta}$ and $C_{y\beta}$ Versus Mach Number for Booster Showing Effects of Interference Effect Due to Orbiter	2-10
2-4	Typical Space Shuttle Configuration	2-11
2-5	$C_{N\alpha}$ Versus Mach Number for the Booster With and Without Wings	2-12
2-6	Typical Space Shuttle Booster Dynamic Pressure Versus Mach Number	2-12
2-7	Pressure Difference Distribution on B-58 Wing for Wing-Fuselage-Fin Configuration ($\alpha = 4$ deg, Mach 0.8)	2-16
2-8	Fuselage Pressure Distribution for B-58 Wing-Fuselage-Fin Configuration ($\alpha = 4$ deg, Mach 0.8, $\beta = 0$ deg)	2-16
2-9	Fin Pressure Distribution for B-58 Wing-Fuselage-Fin Configuration ($\alpha = 4$ deg, Mach 0.8, $\beta = 0$ deg)	2-16
2-10	Engine Gimbal Sign Convention	2-17
4-1	Booster Configuration	4-2
4-2	Pitch Plane Sign Convention	4-3
4-3	Booster Flyback Pitch Plane SAS	4-4
4-4	Booster Canard Structural Idealization	4-6
4-5	Booster Wing Structural Idealization	4-8
4-6	Booster Return Flight, First Symmetric Mode	4-9
4-7	Booster Return Flight, Second Symmetric Mode	4-9
4-8	Booster Return Flight, Third Symmetric Mode	4-10
4-9	Booster Return Flight, Fourth Symmetric Mode	4-10
4-10	Booster Return Flight, Fifth Symmetric Mode	4-11
4-11	Booster Return Flight, Sixth Symmetric Mode	4-11
4-12	Booster Return Flight, Seventh Symmetric Mode	4-12
4-13	Booster Return Flight, Eighth Symmetric Mode	4-12
4-14	Booster Return Flight Fuselage Acceleration \bar{A} and N_0 (SAS Off, Symmetric)	4-13
4-15	Booster Return Flight Fuselage Acceleration Transfer Function (SAS Off, Symmetric) at Crew Station	4-14

LIST OF FIGURES, Contd

Figure		Page
4-16	Booster Return Flight Fuselage Acceleration Transfer Function (SAS Off, Symmetric) at LO ₂ Tank	4-15
4-17	Booster Return Flight Fuselage Acceleration Transfer Function (SAS Off, Symmetric) at LH ₂ Tank	4-16
4-18	Booster Return Flight Fuselage Acceleration PSD (SAS Off, Symmetric) at Crew Station	4-17
4-19	Booster Return Flight Fuselage Acceleration PSD (SAS Off, Symmetric) at LO ₂ Tank	4-18
4-20	Booster Return Flight Fuselage Acceleration PSD (SAS Off, Symmetric) at LH ₂ Tank	4-19
4-21	Booster Return Flight Fuselage Shear Transfer Function at FS 2800 (SAS Off, Symmetric)	4-20
4-22	Booster Return Flight Fuselage Bending Moment Transfer Function at FS 2800 (SAS Off, Symmetric)	4-21
4-23	Booster Return Flight Fuselage Shear PSF at FS 2800 (SAS Off, Symmetric)	4-22
4-24	Booster Return Flight Fuselage Bending Moment PSD at FS 2800 (SAS Off, Symmetric)	4-23
4-25	Booster Return Flight Wing Root Shear Transfer Function (SAS) Off, Symmetric)	4-24
4-26	Booster Return Flight Wing Root Bending Moment Transfer Function (SAS Off, Symmetric)	4-25
4-27	Booster Return Flight Wing Root Torque About FS 3488.5 Transfer Function (SAS Off, Symmetric)	4-26
4-28	Booster Return Flight Wing Root Shear PSD (SAS Off, Symmetric)	4-27
4-29	Booster Return Flight Wing Root Bending Moment PSD (SAS Off, Symmetric)	4-28
4-30	Booster Return Flight Wing Root Torque About FS 3488.5 PSD (SAS Off, Symmetric)	4-29
4-31	Booster Return Flight A-Matrix Determinant Magnitude and Phase Angle (SAS Off, Symmetric)	4-30
4-32	Booster Return Flight A-Matrix Determinant Polar Plot (SAS Off, Symmetric)	4-31
4-33	Booster Return Flight Fuselage Acceleration Transfer Function (SAS On, Symmetric) at Crew Station	4-32
4-34	Booster Return Flight Fuselage Acceleration Transfer Function (SAS On, Symmetric) at LO ₂ Tank	4-33

LIST OF FIGURES, Contd

Figure		Page
4-35	Booster Return Flight Fuselage Acceleration Transfer Function (SAS On, Symmetric) at LH ₂ Tank	4-34
4-36	Booster Return Flight Fuselage Acceleration PSD (SAS On, Symmetric) at Crew Station	4-35
4-37	Booster Return Flight Fuselage Acceleration PSD (SAS On, Symmetric) at LO ₂ Tank	4-36
4-38	Booster Return Flight Fuselage Acceleration PSD (SAS On, Symmetric) at LH ₂ Tank	4-37
4-39	Booster Return Flight Fuselage Acceleration \bar{A} and N_o (SAS On, Symmetric)	4-38
4-40	Booster Return Flight A-Matrix Determinant Magnitude and Phase Angle (SAS On, Symmetric)	4-39
4-41	Booster Return Flight A-Matrix Determinant Polar Plot (SAS On, Symmetric)	4-40
4-42	Ascent Symmetric Flight Sign Convention	4-41
4-43	Ascent Symmetric Flight SAS Block Diagram	4-42
4-44	Ascent Antisymmetric Flight Sign Convention	4-42
4-45	Ascent Antisymmetric Flight SAS Block Diagram	4-43
4-46	Booster Vertical Stabilizer Structural Idealization	4-46
4-47	Booster/Orbiter Attachment Stiffnesses	4-47
4-48	Ascent Flight First Symmetric Mode	4-48
4-49	Ascent Flight Second Symmetric Mode	4-48
4-50	Ascent Flight Third Symmetric Mode	4-49
4-51	Ascent Flight Fourth Symmetric Mode	4-49
4-52	Ascent Flight Fifth Symmetric Mode	4-50
4-53	Ascent Flight Sixth Symmetric Mode	4-50
4-54	Ascent Flight First Antisymmetric Mode	4-51
4-55	Ascent Flight Second Antisymmetric Mode	4-52
4-56	Ascent Flight Third Antisymmetric Mode	4-53
4-57	Ascent Flight Fourth Antisymmetric Mode	4-54
4-58	Ascent Flight Fifth Antisymmetric Mode	4-55
4-59	Ascent Flight Sixth Antisymmetric Mode	4-56
4-60	Ascent Flight Seventh Antisymmetric Mode	4-57
4-61	Ascent Flight, Fuselage Normal Acceleration \bar{A} and N_o (SAS Off, Symmetric)	4-60
4-62	Ascent Flight Fuselage Normal Acceleration Transfer Function (SAS Off, Symmetric)	4-61
4-63	Ascent Flight Fuselage Normal Acceleration PSD (SAS Off, Symmetric)	4-62

LIST OF FIGURES, Contd

Figure		Page
4-64	Ascent Flight A-Matrix Determinant Magnitude and Phase Angle (SAS Off, Symmetric)	4-63
4-65	Ascent Flight A-Matrix Determinant Polar Plot (SAS Off, Symmetric)	4-64
4-66	Ascent Flight Wing Root RMS Shear and Bending Moment Versus RMS Turbulence Level (SAS On, Symmetric)	4-66
4-67	Ascent Flight Fuselage Normal Acceleration Transfer Function (SAS On, Symmetric)	4-67
4-68	Ascent Flight Fuselage Normal Acceleration PSD (SAS On, Symmetric)	4-68
4-69	Ascent Flight A-Matrix Determinant Magnitude and Phase Angle (SAS On, Symmetric)	4-69
4-70	Ascent Flight A-Matrix Determinant Polar Plot (SAS On, Symmetric)	4-70
4-71	Ascent Flight Fuselage Lateral Acceleration \bar{A} and N_o (SAS Off, Antisymmetric)	4-72
4-72	Ascent Flight Fuselage Lateral Acceleration Transfer Function (SAS Off, Antisymmetric)	4-73
4-73	Ascent Flight Fuselage Lateral Acceleration PSD (SAS Off, Antisymmetric)	4-74
4-74	Ascent Flight A-Matrix Determinant Magnitude and Phase Angle (SAS Off, Antisymmetric)	4-75
4-75	Ascent Flight A-Matrix Determinant Polar Plot (SAS Off, Antisymmetric)	4-76
4-76	Ascent Flight Fuselage Lateral Acceleration Transfer Function (SAS On, Antisymmetric)	4-78
4-77	Ascent Flight Fuselage Lateral Acceleration PSD (SAS On, Antisymmetric)	4-79
4-78	Ascent Flight A-Matrix Determinant Magnitude and Phase Angle (SAS On, Antisymmetric)	4-80
4-79	Ascent Flight A-Matrix Determinant Polar Plot (SAS On, Antisymmetric)	4-81

LIST OF TABLES

Table		Page
2-1	Applicability of Referenced Theories to Significant Effects	2-14
2-2	Comparison of Quasi-Steady and Experimental Flutter Results at Mach 1.09	2-15
2-3	Comparison of Quasi-Steady, Unsteady, and Experimental Flutter Results at Mach 1.37	2-15
4-1	Data for the Booster Return Flight Analysis	4-5
4-2	Booster Return Flight Load Summary (SAS Off, Symmetric)	4-7
4-3	Sloshing Parameters	4-44
4-4	Basic Data - Symmetric Ascent Flight	4-44
4-5	Basic Data - Antisymmetric Ascent Flight	4-45
4-6	Booster Ascent Flight Load Summary (SAS Off, Symmetric)	4-59
4-7	Booster Ascent Flight Load Summary (SAS On, Symmetric)	4-65
4-8	Booster Ascent Flight Load Summary (SAS Off, Antisymmetric)	4-71
4-9	Booster Ascent Flight Load Summary (SAS On, Antisymmetric)	4-77

SUMMARY

A computer program was developed and demonstrated that can analyze the response of space shuttle to atmospheric turbulence. The method developed accounts for propellant slosh, gimbaled engine, and stability augmentation system (SAS) coupling with the elastic vehicle. Statistical outputs are generated that relate vehicle loads and accelerations to level of random turbulence. For discrete turbulence descriptions, response time-histories are computed.

The response problem is formulated in the frequency domain, thereby permitting the use of any quasi-steady or unsteady aerodynamic theory based on harmonic motion. Gust penetration effects are readily accounted for. The quasi-steady approach using the Woodward aerodynamic method for subsonic and supersonic flows appears promising for the space shuttle turbulence response problem. Properly predicting flow interference, thickness, angle-of-attack, and body effects is more important for space shuttle than including aerodynamic lag effects for the reduced-frequency range of interest.

Preliminary turbulence response analyses of space shuttle were conducted for one ascent and one booster flyback subsonic flight condition. The ascent case considered both symmetric and antisymmetric boundary conditions, while only the symmetric analysis was conducted for booster flyback. The three conditions were analyzed with SAS active and inactive, but apparent instabilities with SAS active (arising from improper gains) invalidated the results. Load and acceleration responses in all cases, however, were well within vehicle design limits.

It is recommended that future response studies be preceded by stability checks to ensure that the elastic vehicle/SAS is stable and that the gains used in the response analysis are correct. It is also recommended that the study be expanded to include other subsonic and supersonic flight conditions.

SECTION 1

INTRODUCTION

This report presents the results of the first year's work under Contract NAS8-26363, "Aeroelastic Effects on Shuttle Vehicle Dynamics". The objective of this portion of the effort was to develop and demonstrate a computer program to analyze the response of space shuttle to atmospheric turbulence.

Section 2 contains the equations of motion, a discussion of unsteady and quasi-steady aerodynamic theories, and a description of methods for handling propellant slosh and engine dynamics. The computer program is described briefly in Section 3; a detailed user's guide is contained in Reference 1.

To check out and demonstrate the computer program, a typical space shuttle configuration was analyzed in the ascent and booster return conditions. The results are presented in Section 4.

Application of random turbulence response techniques to launch vehicles has been very limited prior to the advent of space shuttle. For expendable systems in which fatigue life is not an important consideration and exposure to atmospheric turbulence is of short duration, discrete gust concepts have proven adequate for design. The space shuttle, however, will be subjected to many reuses and will encounter turbulence during ascent and flyback that may produce design loads, fatigue damage, and ride discomfort.

Gust criteria for structural design have evolved from simple descriptions of atmospheric turbulence to more sophisticated concepts that correlate closely with measurements. Early design concepts treated the vertical (lateral) component of the gust velocity as a step function as shown in Figure 1-1. The aircraft was assumed to travel instantaneously from a region with zero gust velocity into a constant gust velocity region. Subsequent refinements considered the effect of gradual penetration of the vehicle into the gust field.

Later concepts considered one-dimensional discrete profiles such as the (1-cosine) wave shape shown in Figure 1-1. Efforts were then largely directed toward defining the wave length and peak velocity of the gust for aircraft design purposes. It was soon recognized that the average peak gust velocity associated with large wave lengths was greater than that for small wave lengths.

The next step in the evolution of gust criteria treated the vertical (lateral) component of the gust velocity as being random in the flight direction while continuing to retain the concept of constant gust velocity in the direction perpendicular to the flight path (Figure 1-1). With the introduction of the random concept, gust velocity was defined

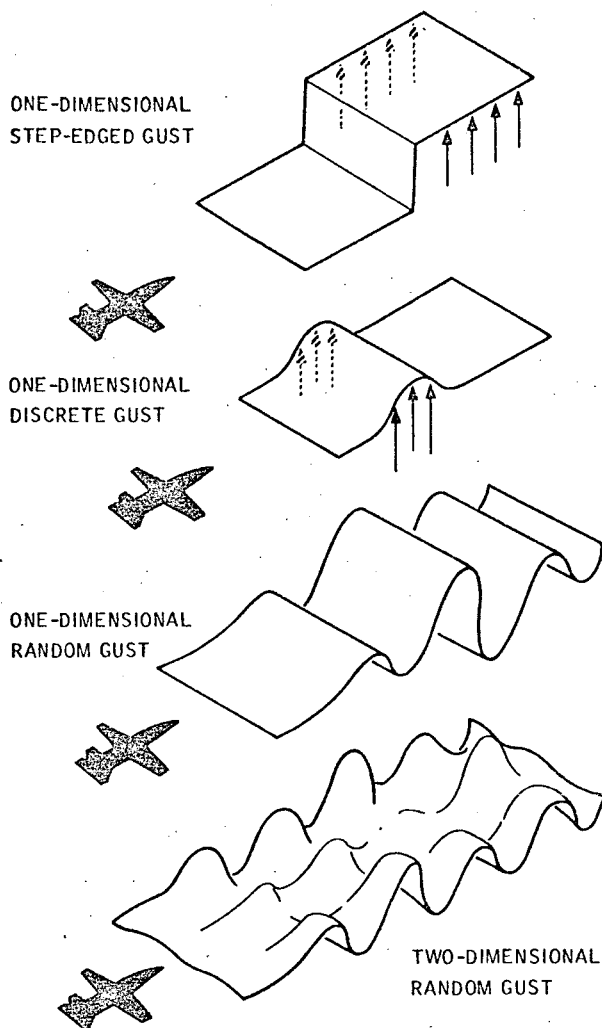


Figure 1-1. Evolution of Gust Design Criteria

by certain averages, such as root mean square (rms) and power spectral density (PSD). The observed fact that even the average values of turbulence vary with such parameters as atmospheric condition, geographic location, season of the year, and distance above the earth's surface was described in terms of the probability of encountering turbulence with specified rms values. By describing the aircraft response characteristics in terms of transfer functions, its response to one-dimensional random turbulence could be computed. The random response was also described in terms of averages, and it was possible to compute the average or expected number of times that the response exceeded any specified level. These concepts have been developed to the point that they are now widely accepted as the preferred manner in which to determine the effects of atmospheric turbulence on aircraft.

Numerous Air Force sponsored gust-measuring programs have been conducted and some are currently being performed. The results of these investigations have led to the generally accepted conclusion that the measured gust spectra can be best described by the Von Karman gust spectrum (compared in Figure 1-2 with

the Dreyden spectrum) with a scale of turbulence (L) that varies from 500 feet near sea level to 2500 feet at higher altitudes. The probability of encountering rms gust velocities of any given value in clear air or thunderstorm turbulence is specified by the altitude-dependent variance of the rms gust velocities. The percentage of time that clear-air turbulence or thunderstorm turbulence is encountered is described by fractions, which also vary with altitude.

The latest development of these concepts considers each component of turbulence to vary in any plane through the flight path of the vehicle. This concept, identified as two-dimensional random turbulence in Figure 1-1, is refinement of the one-dimensional turbulence model. It has been found, however, that the improvement in the results is worth the added computational effort only when the gust wave lengths of importance are comparable to the wing span or less. Although only the normal component of gust velocity is illustrated in Figure 1-1, lateral and longitudinal gust velocities are treated

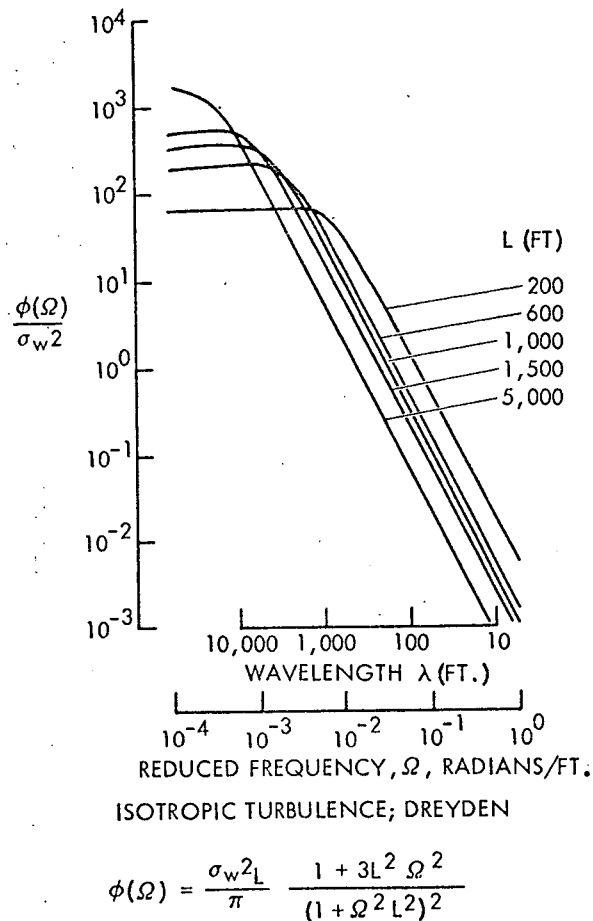
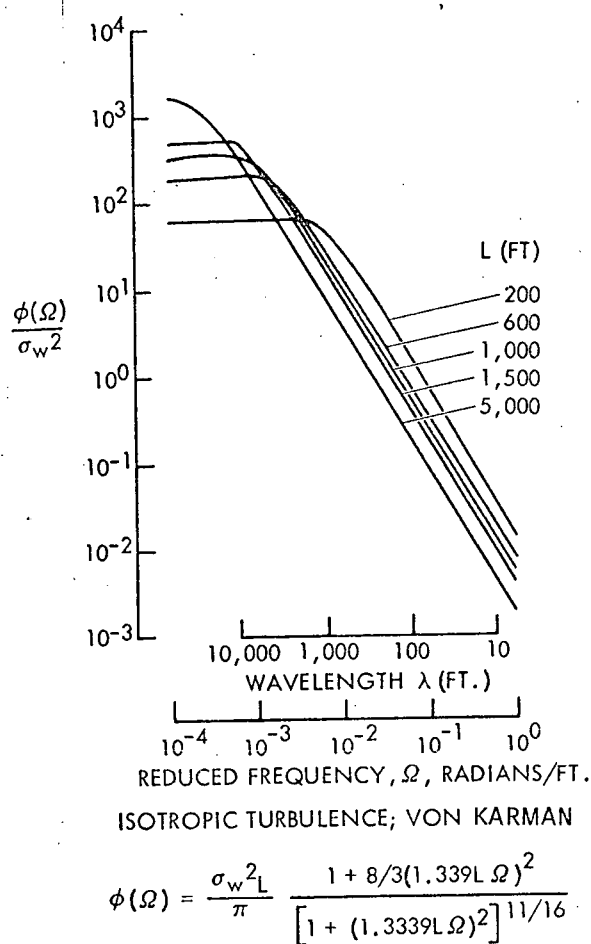


Figure 1-2. Analytical Representation of Atmospheric Turbulence Spectra

in the same manner. Longitudinal gust velocity effects on aircraft are usually considered negligible.

Launch vehicle gust criteria development has paralleled the aircraft gust criteria in many ways. The initial emphasis was placed on determining the response to discrete gust velocities. The missile flight path is characterized by continuously changing velocity and altitude, whereas an aircraft is often at a fixed airspeed and altitude for long periods of time. The vertical path of the missile through varying wind shears produces significant gust loads, whereas only the turbulence produced by wind shears affects the airplane loads. These considerations have led to the concept of computing gust loads on missiles due to flight through a wind-shear profile on a deterministic basis. While this method may have been adequate for missiles where fatigue life was not an important consideration, due to the large number of shuttle flights expected

it is suggested and recommended that gust loads be determined on a probabilistic basis for space shuttle. Although the method described would require that the flight path be segmented in sufficiently small increments to permit airspeed, altitude, and mass properties to be considered constant over the increment, this disadvantage appears to be more than offset by the advantages of the probabilistic approach. In the present study, one-dimensional turbulence described by the Von Karman spectrum is assumed.

The concept of computing response characteristics of the vehicle in the frequency domain is attractive from the unsteady aerodynamic complexity viewpoint. In general, it is easier to compute the unsteady aerodynamic pressure produced by oscillatory motion of the vehicle or oscillatory gust velocity than to compute the response of the vehicle to a step function change in downwash. (The latter step is the usual preliminary step before applying Duhamel's integral for determining the response to an arbitrary variation in the downwash.) By assuming harmonic motion, all recently developed oscillatory aerodynamic theories can be used to compute the frequency response functions. Subsequently, the frequency response functions can be combined with the random gust spectra to obtain response spectra, or they can be used to obtain a Fourier series solution of the response in the time domain to a discrete gust of arbitrary shape. Hence, solutions in both the frequency domain and time domain can be obtained.

SECTION 2

TECHNICAL DISCUSSION

This section presents a discussion of the equations of motion included in the computer program. The method is general, and may be applied to any vehicle whose motion is described in terms of modal generalized coordinates.

2.1 TURBULENCE RESPONSE

Vehicle response is computed by solving sets of simultaneous equations obtained by applying Lagranges' equation of motion:

$$\frac{d}{dt} \left(\frac{\partial L}{\partial \dot{q}_r} \right) - \frac{\partial L}{\partial q_r} + \frac{\partial \mathcal{D}}{\partial \dot{q}_r} = \bar{Q}_r \quad r = 1, 2, \dots, n \quad (2-1)$$

where

$$L = T - P$$

$$T = \text{kinetic energy}$$

$$P = \text{potential energy}$$

$$\mathcal{D} = \text{dissipation function}$$

$$\bar{Q}_r = r^{\text{th}} \text{ generalized force}$$

$$q_r = r^{\text{th}} \text{ generalized coordinate}$$

The deflection (h) at any point on the vehicle is given by:

$$h(x, y, z, t) = \sum_{r=1}^n h_r(x, y, z) q_r(t) \quad (2-2)$$

where h_r is the normalized deflection at the point in the r^{th} mode shape.

Using normal (with respect to the stiffness matrix) modes of vibration as generalized coordinates, the r^{th} equation of motion is of the form:

$$M_{rr} \ddot{q}_r + D_{rr} \dot{q}_r + M_{rr} \omega_r^2 q_r + \sum_{s=1}^n \delta_{rs}^* M_{rs} \ddot{q}_s = \bar{Q}_r \quad (2-3)$$

where

M_{rs} = generalized mass

D_{rr} = generalized damping

ω_r = frequency of mode r

$\delta_{rs}^* = \begin{cases} 0, r=s \\ 1, r \neq s \end{cases}$

For the vehicle in the absence of a stability augmentation system, the generalized force includes the force produced by the gust and the force caused by the vehicle response. This can be written as:

$$\bar{Q}_r = \underbrace{\sum_{s=1}^n q_s \bar{Q}_{rs}}_{\text{Response}} + \underbrace{q_f \bar{Q}_{rf}}_{\text{Gust}} \quad (2-4)$$

where \bar{Q}_{rs} is the r^{th} generalized aerodynamic force due to a unit value of the vehicle displacement in mode s , q_f is the gust amplitude, and \bar{Q}_{rf} is the r^{th} generalized aerodynamic force due to a unit gust.

For harmonic motion, the equations of motion can be written in matrix form as:

$$\{\bar{q}(\omega)\} = -[A(\omega)]^{-1} \{A_f(\omega)\} \quad (2-5)$$

where

$$A_{rs} = \left[1 - \delta_{rs} \left(\frac{\omega_r}{\omega} \right)^2 (1 + i g_r) \right] M_{rs} + Q_{rs} \quad (2-5a)$$

$$\delta_{rs} = \begin{cases} 1, r=s \\ 0, r \neq s \end{cases}$$

$$i = \sqrt{-1}$$

g_r = structural damping coefficient for mode r

ω = gust frequency

\bar{q}_r = amplitude of the r^{th} generalized coordinate

$$\bar{M}_{rs} = \frac{M_{rs}}{4 \rho b^3} \quad (2-6)$$

$$A_{rf}(\omega) = \frac{q_f \bar{Q}_{rf}(\omega)}{4 \rho b^3 \omega^2} \quad (2-7)$$

$$Q_{rs}(\omega) = \frac{1}{4 \rho b^3 \omega^2} \int_S h_r(x, y, z) \Delta p_s(x, y, z, \omega) dS \quad (2-8)$$

where ρ is air density, b is the reference length, Δp_s is the net unsteady pressure acting on the vehicle due to oscillation in mode s , and the integration is over the surface of the vehicle. Methods available for determining the unsteady pressure distribution are described briefly in Section 2.3.

The generalized force due to the unit sinusoidal gust is given by:

$$\bar{Q}_{rf}(\omega) = \int_S h_r(x, y, z) \Delta p_f(x, y, z, \omega) dS \quad (2-9)$$

where Δp_f is the net pressure over the vehicle surface due to the downwash produced by a continuous sinusoidal gust wave traveling across the vehicle. This sinusoidal gust velocity may be expressed as:

$$\begin{aligned} W_f &= q_f e^{i\omega t} \\ &= q_f (\cos \omega t + i \sin \omega t) \end{aligned} \quad (2-10)$$

The downwash on an oscillating airfoil in a flow of velocity (V) is given by:

$$w(t) = V \alpha(t) - \dot{h}(t) \quad (2-11)$$

where α is the angle of attack and \dot{h} is the plunging velocity. For harmonic motion, the complex downwash may be written:

$$\bar{w} = V \bar{\alpha} - i \omega \bar{h} \quad (2-12)$$

Equating 2-10 and 2-12 yields:

$$\begin{aligned} W_f &= \bar{w} \\ \bar{\alpha} &= \frac{q_f}{V} \cos \omega t \end{aligned} \quad (2-13)$$

$$\bar{h} = -\frac{q_f}{\omega} \sin \omega t \quad (2-14)$$

If x_i is the distance from a gust reference axis to the downwash at point i on the vehicle and k is the reduced frequency

$$\left(k = \frac{b \omega}{V}\right) \quad (2-15)$$

then Equations 2-13 and 2-14 become:

$$\bar{\alpha}_i = \frac{q_f}{V} \cos k \bar{x}_i \quad (2-16)$$

$$\bar{h}_i = -\frac{q_f b}{V k} \sin k \bar{x}_i \quad (2-17)$$

where

$$\bar{x}_i = \frac{x_i}{b}$$

From the $\bar{\alpha}$ and \bar{h} distributions, the net pressure distribution (Δp_f) due to the gust is obtained using the same unsteady aerodynamic theory employed to compute pressure distribution due to vehicle motion.

Response transfer functions are readily obtained from the generalized coordinates computed in Equation 2-5. The acceleration transfer function is given by:

$$H_A(x, y, z, \omega) = -\frac{1}{q_f} \sum_{r=1}^n \omega_r^2 h_r(x, y, z) \bar{q}_r(\omega) \quad (2-18)$$

Loading transfer functions can be obtained by modal displacement or load summation. The modal displacement technique is based on the concept that the deformed shape of a body defines the load (shear, moment, and torque) distributions. Assuming that n generalized coordinates are sufficient to define the deformed shape, the load transfer functions are of the form:

$$H(x, y, z, \omega) = \frac{1}{q_f} \sum_{r=1}^n F_r(x, y, z) \bar{q}_r(\omega) \quad (2-19)$$

where F_r is the load (shear, moment, or torque) due to a unit value of \bar{q}_r .

The load summation method combines the loads due to inertia forces and air forces. The load transfer function is given by:

$$H(x, y, z, \omega) = \frac{\omega^2}{q_f} \sum_{r=1}^n F_r'(x, y, z) \bar{q}_r(\omega) + \frac{1}{q_f} \sum_{r=1}^n \bar{F}_r(x, y, z, \omega) \bar{q}_r(\omega) + \frac{F_f(x, y, z, \omega)}{q_f} \quad (2-20)$$

where F_r' is the inertia load (shear, moment, or torque) due to the r^{th} degree of freedom oscillating at a unit frequency, \bar{F}_r is the load due to the aerodynamic pressure distribution developed by a unit amount of the r^{th} generalized coordinate oscillating at frequency ω , and F_f is the load due to the aerodynamic pressure distribution produced by a gust wave of frequency ω .

2.1.1 RESPONSE TO RANDOM DISTURBANCE. The response power spectral density (PSD), ϕ_x , is related to the gust PSD, ϕ , and the transfer function magnitude, $|H|$, by the equation:

$$\phi_x(\omega) = |H(\omega)|^2 \phi(\omega) \quad (2-21)$$

The two most common gust PSD forms are shown in Figure 1-2, where $\Omega = \omega/V$, L is the scale of turbulence measured in feet, and σ_w is the rms turbulence velocity in feet per second.

The ratio of rms response to rms gust velocity is given by:

$$\bar{A} = \left[\int_0^{\omega_c} \phi_x(\omega) d\omega \right]^{1/2} \quad (2-22)$$

where ω_c is the integration cutoff frequency. The "characteristic frequency" of the response, or number of zero crossings with positive slope per second, is expressed by:

$$N_0 = \frac{1}{2\pi\bar{A}} \left[\int_0^{\omega_c} \omega^2 \phi_x(\omega) d\omega \right]^{1/2} \quad (2-23)$$

The total number of response peaks per second is given by:

$$N_1 = \frac{1}{\bar{A} N_0} \left[\int_0^{\omega_c} \omega^4 \phi_x(\omega) d\omega \right]^{1/2} \quad (2-24)$$

2.1.2 RESPONSE TO DISCRETE DISTURBANCE. The Fourier series technique is used to represent the discrete forcing function. This is written:

$$f(t) = a_0 + \sum_{m=1}^M (a_m \cos \bar{\omega}_m t + b_m \sin \omega_m t) \quad (2-25)$$

where

$f(t)$ is the forcing function

M is the number of terms in the series

t = time

$$\omega_m = m \pi / T$$

$$a_0 = \frac{1}{2T} \int_{-T}^T f(t) dt$$

$$a_m = \frac{1}{T} \int_{-T}^T f(t) \cos \bar{\omega}_m t dt$$

$$b_m = \frac{1}{T} \int_{-T}^T f(t) \sin \bar{\omega}_m t dt$$

The resulting force time-history $f(t)$ is periodic with period $2T$.

As prescribed by Equation 2-25, the force is stationary. It is often more convenient to think of the vehicle as being fixed, with the disturbance moving over it. This is described by substituting $(x/V - t)$ for t in Equation 2-25, which yields:

$$f(t) = a_0 + \sum_{m=1}^M a_m \cos (k_m \bar{x} - \omega_m t) + b_m \sin (k_m \bar{x} - \omega_m t) \quad (2-26)$$

where

$$k_m = \omega_m b / V$$

$$\bar{x} = x/b$$

b is the reference length

V is the vehicle velocity

x is the distance from a point on the vehicle to the gust reference axis

By considering that the cosine terms are symmetric and the sine terms are antisymmetric, Equation 2-26 can be written:

$$f(t) = a_o + \sum_{m=1}^M \left[a_m \cos(\omega_m t - k_m \bar{x}) - b_m \sin(\omega_m t - k_m \bar{x}) \right] \quad (2-27)$$

In complex form, Equation 2-27 can be written as:

$$f(t) = a_o + \operatorname{Re} \left[\sum_{m=1}^M a_m e^{i(\omega_m t - k_m \bar{x})} \right] - \operatorname{Im} \left[\sum_{m=1}^M b_m e^{i(\omega_m t - k_m \bar{x})} \right] \quad (2-28)$$

The vehicle response to this disturbance is given by

$$Z(t) = \sum_{m=1}^M \left[(a_m H_{R_m} + b_m H_{I_m}) \cos \bar{\omega}_m t + (b_m H_{R_m} - a_m H_{I_m}) \sin \bar{\omega}_m t \right] \quad (2-29)$$

where H_{R_m} and H_{I_m} are the real and imaginary components of the m^{th} transfer function evaluated at frequency $\bar{\omega}_m$, i.e.:

$$H_m = H_{R_m} + iH_{I_m} \quad (2-30)$$

2.2 STABILITY AUGMENTATION SYSTEM SIMULATION

For a vehicle having a stability augmentation system (SAS), Equation 2-5 is modified to include the control surface aerodynamic and inertia forces so that the equation becomes:

$$[A(\omega)] \left\{ \bar{q}(\omega) \right\} = - \left\{ A_f(\omega) \right\} - \left\{ M_\delta + Q_\delta(\omega) \right\} \delta(\omega) \quad (2-31)$$

where M_{r_δ} is the generalized mass term coupling the r^{th} vehicle mode to the control surface unit rotation, and Q_{r_δ} is defined by:

$$Q_{r_\delta}(\omega) = \frac{1}{4 \rho b^3 \omega^2} \int_S h_r(x, y, z) \Delta p_\delta(x, y, z, \omega) dS \quad (2-32)$$

where the integration is over the entire vehicle surface and Δp_δ is the net unsteady pressure distribution acting on the vehicle due to unit amplitude oscillation of the control surface at frequency ω .

It is interesting to note that the vehicle response to a time-dependent control surface motion can be obtained by applying the Fourier series method outlined in Section 2.1.2 to Equation 2-31 to describe $\delta(t)$ and setting A_f equal to zero.

The general block diagram for a vehicle with a one-channel SAS is shown in Figure 2-1.

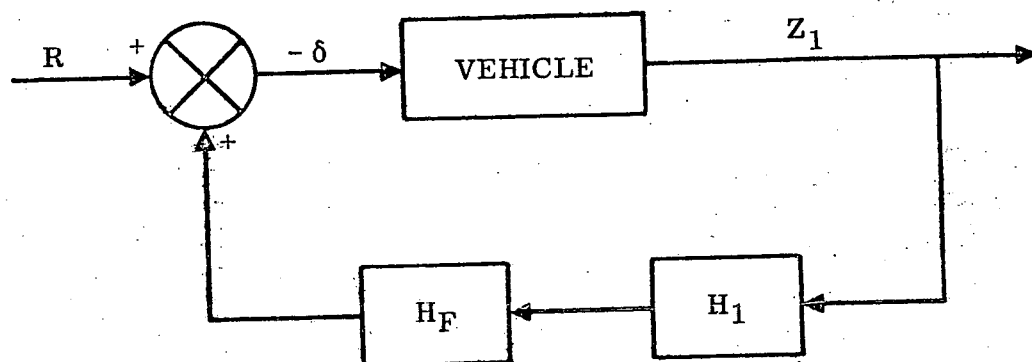


Figure 2-1. SAS Block Diagram

Control surface rotation is given by:

$$\delta(\omega) = -R(\omega) - H_F(\omega) H_1(\omega) Z_1(\omega) \quad (2-33)$$

where $R(\omega)$ is the control input, H_F and H_1 are system transfer functions, and Z_1 is the response. The response is given by:

$$Z_1(\omega) = \sum_{r=1}^n h_r^{(1)} \bar{q}_r(\omega) \quad (2-34)$$

where $h_r^{(1)}$ is the normalized deflection at point (1) in the r^{th} mode shape and $\bar{q}_r(\omega)$ is the r^{th} generalized coordinate evaluated at frequency ω . Substituting Equation 2-34 into 2-33 yields in matrix form:

$$\delta(\omega) = -R(\omega) - [G(\omega)] \{\bar{q}(\omega)\} \quad (2-35)$$

where

$$[G(\omega)] = H_F(\omega) H_1(\omega) [h^{(1)}] \quad (2-36)$$

Substituting Equation 2-35 into 2-31 yields the following expression for the generalized coordinate response.

$$\{\bar{q}\} = - [A] - \{F_\delta\} [G]^{-1} \left\{ \{A_f\} - \{F_\delta\} R \right\} \quad (2-37)$$

where

$$\{F_\delta(\omega)\} = \{M_\delta + Q_\delta(\omega)\} \quad (2-38)$$

It can be seen from Equation 2-37 that the effect of an automatic control system is to modify the A-matrix. For a vehicle with an SAS and no control input command ($R=0$), Equation 2-31 may be written:

$$\{\bar{q}\} = - [A^*]^{-1} \{A_f\} \quad (2-39)$$

where

$$[A^*] = [A] - \{F_\delta\} [G]$$

Equation 2-39 has exactly the same form as Equation 2-5, the response of the unaugmented vehicle.

For a system with multiple sensors such as shown in Figure 2-2, the expression for $g(\omega)$ becomes:

$$[G(\omega)] = H_F(\omega) \sum_{j=1}^m H_j(\omega) [h^{(j)}] \quad (2-40)$$

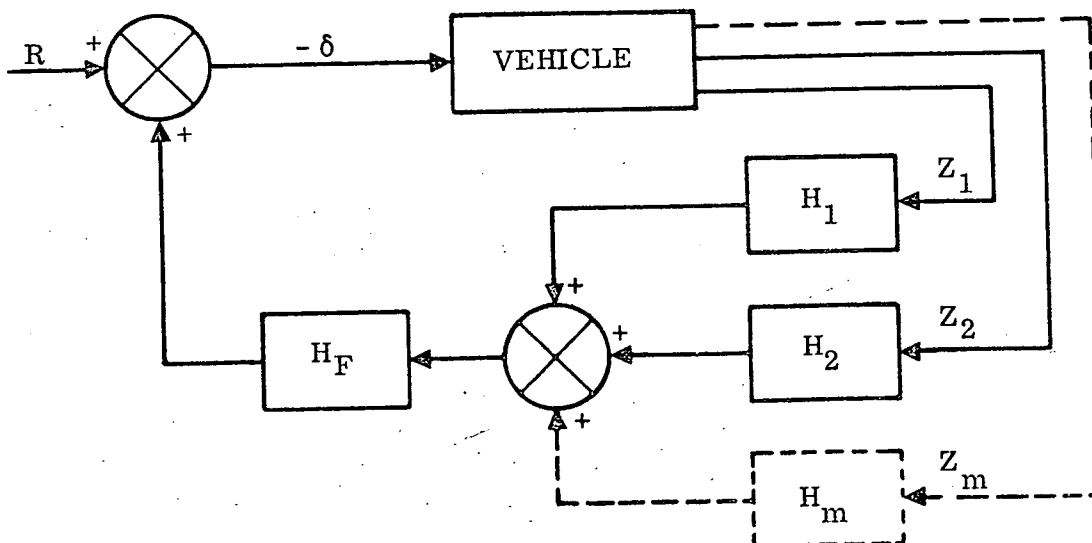


Figure 2-2. Multiple Sensor SAS

For a system having m independent control surfaces, the generalized coordinate response is given by:

$$\{\ddot{q}\} = - \left[[A] - \sum_{j=1}^m \left\{ F_{\delta}^{(j)} \right\} \left[G^{(j)} \right] \right]^{-1} \left\{ \left\{ A_f \right\} - \sum_{j=1}^m \left\{ F_{\delta}^{(j)} \right\} R_j \right\} \quad (2-41)$$

In other words, additional control channels are additive to the single control surface case given by Equation 2-37.

2.3 AERODYNAMICS

Parallel-mounted vehicles, such as those being proposed for the space shuttle, present unique problems to the aeroelastician. Interference effects between the booster and orbiter vehicles in the mated configuration have been found in wind tunnel tests to be significant, particularly in the yaw plane. Figure 2-3 shows the derivatives of the

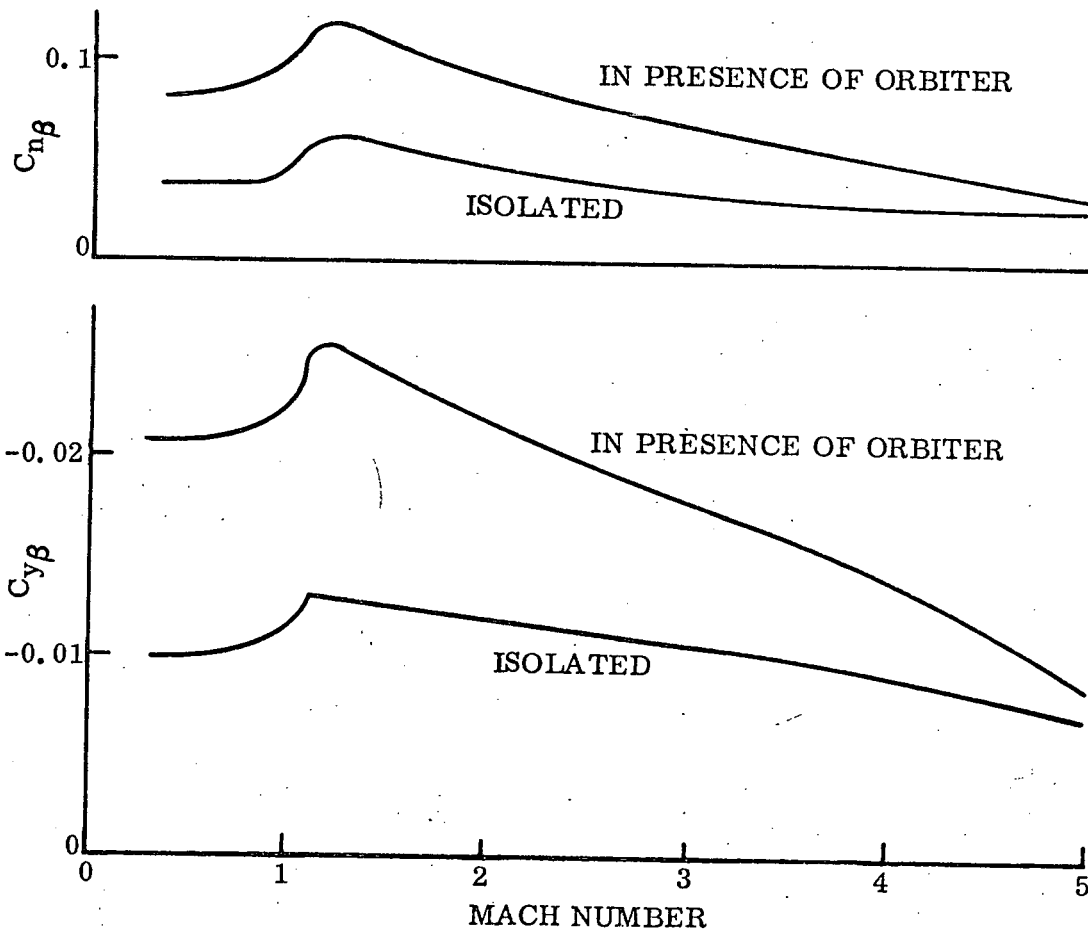


Figure 2-3. $C_{n\beta}$ and $C_{y\beta}$ Versus Mach Number for Booster Showing Effects of Interference Effect Due to Orbiter

yawing moment ($C_{n\beta}$) and the side force coefficient ($C_{y\beta}$) as a function of Mach number for the configuration shown in Figure 2-4. Interference effects tend to double the isolated values at the lower Mach numbers.

The space shuttle is characterized by a large body relative to the wing and tail surfaces. This is because lifting surfaces are required only when the propellant is depleted and the vehicle is light. Figure 2-5 shows the derivative of normal force coefficient ($C_{N\alpha}$) as a function of Mach number for the booster. The top curve is a plot of wind tunnel data for the complete booster, the middle curve for the same configuration with the wings removed, and the bottom curve the difference between the two. Subsonically, $C_{N\alpha}$ for the body-tail is about 85 percent of the total. Transonically, the body-tail $C_{N\alpha}$ is about half of the total, increasing to about 70 percent of the total supersonically.

The nature of the space shuttle mission is such that it flies at subsonic, transonic, supersonic, and hypersonic speeds. Figure 2-6 shows a typical plot of dynamic pressure versus Mach number during boost and entry flight. Angle of attack during boost flight ranges from about plus 5 degrees to minus 10 degrees. The separated vehicles enter at very high angle of attack and then transition to airplane-type flight at low supersonic or subsonic speeds. The requirement for subsonic cruise to the landing site is the reason that the airfoils tend to be thick (10 to 20 percent) and have subsonic planforms.

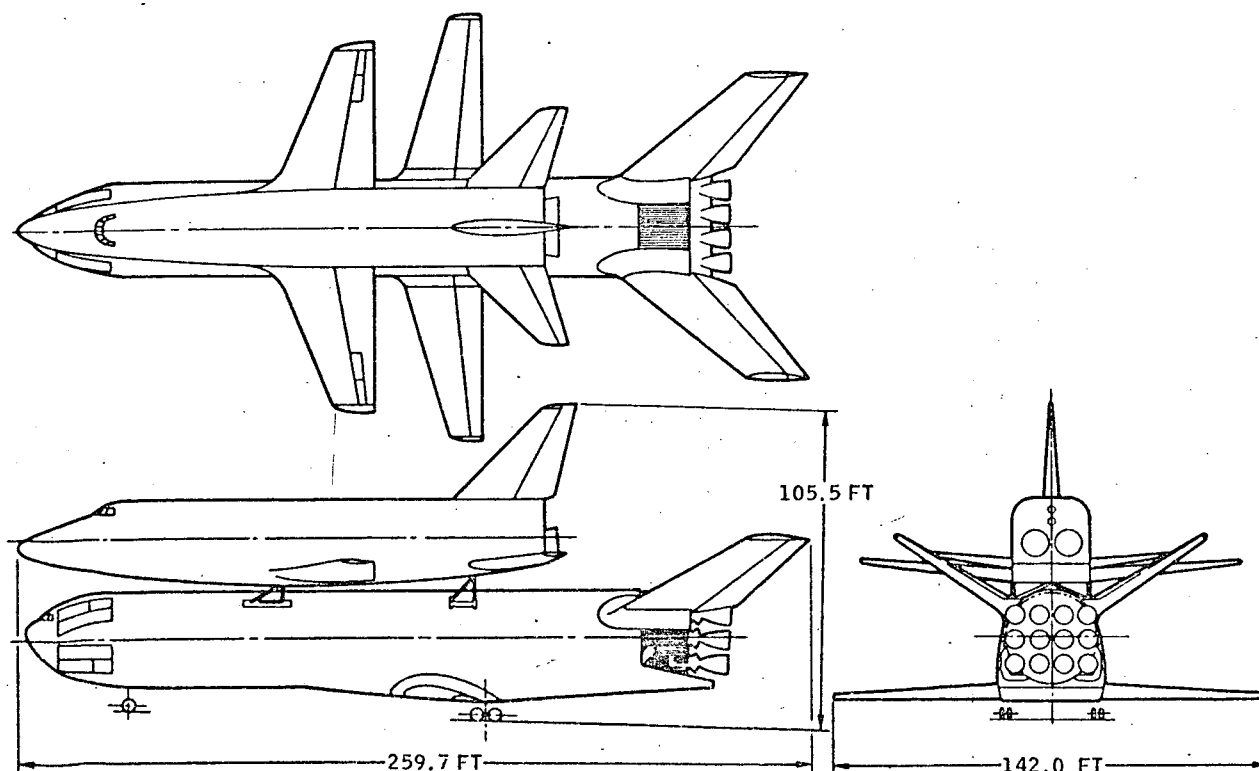


Figure 2-4. Typical Space Shuttle Configuration

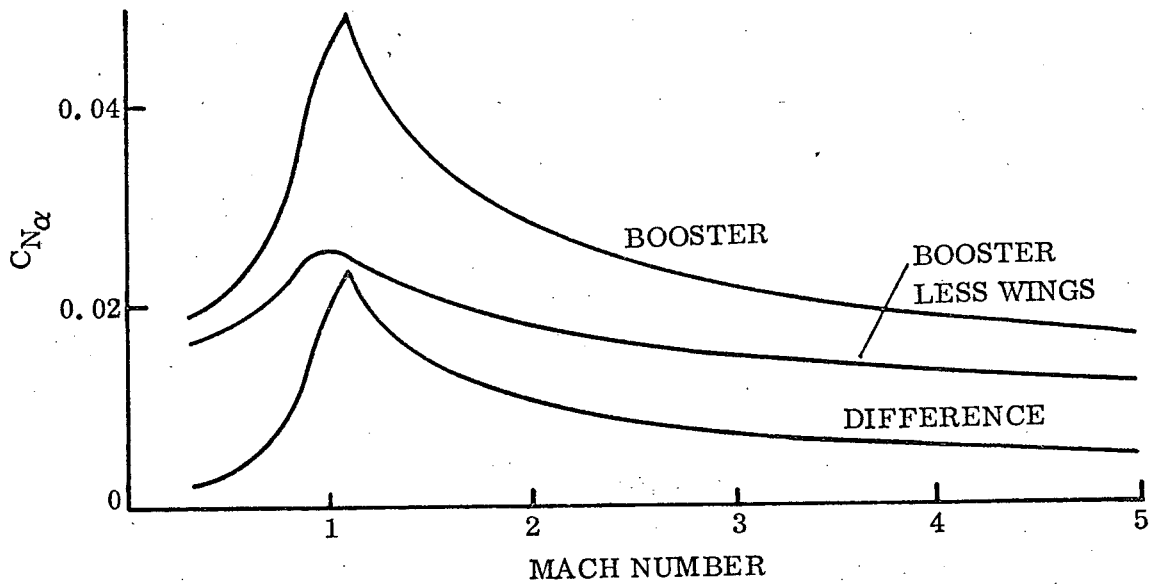


Figure 2-5. C_{N_α} Versus Mach Number for the Booster With and Without Wings

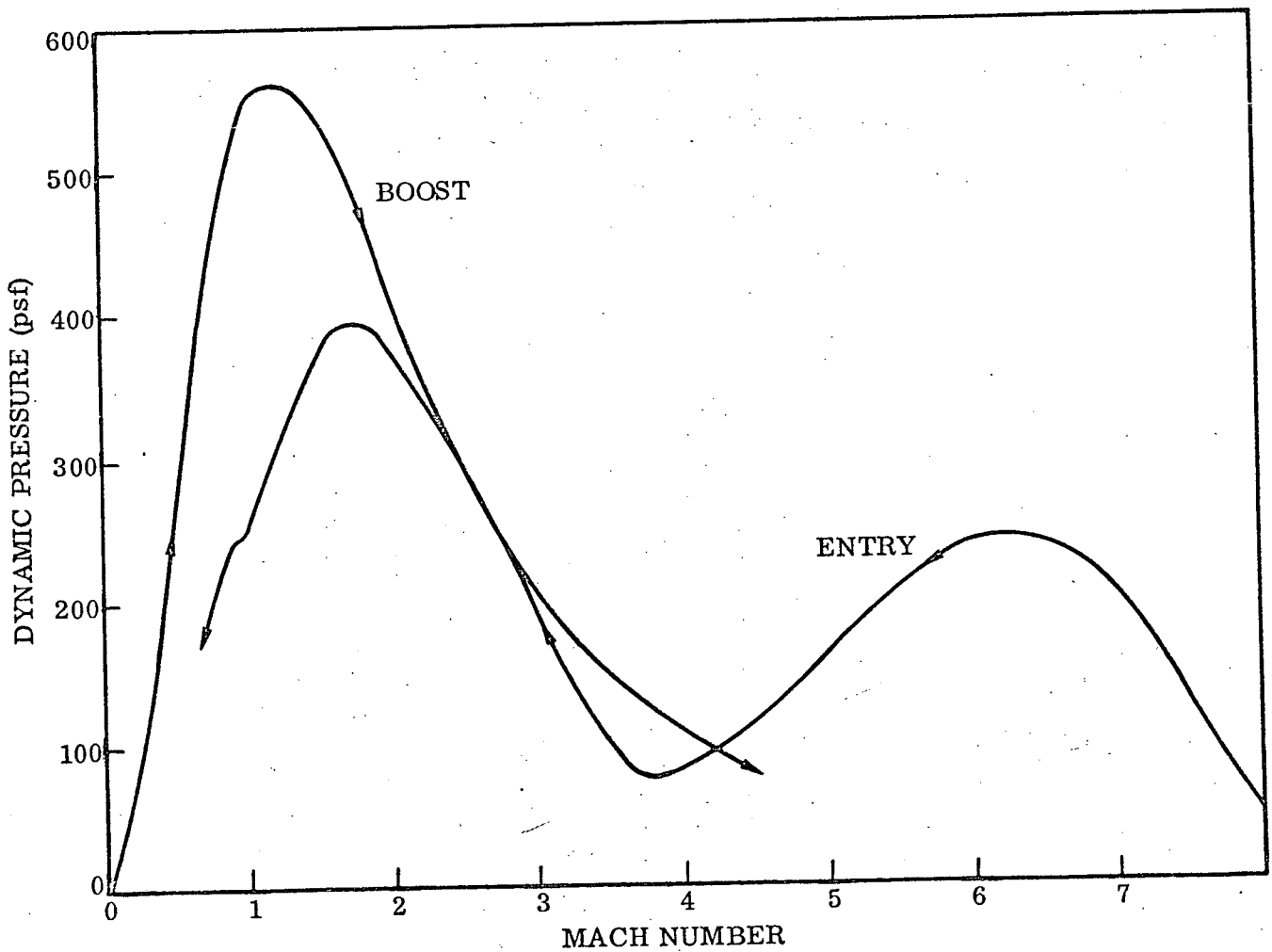


Figure 2-6. Typical Space Shuttle Booster Dynamic Pressure Versus Mach Number

From the preceeding discussion, it is obvious that any aerodynamic theory employed to predict space shuttle response to atmospheric disturbance should account for body aerodynamics, aerodynamic interference effects, thickness effects, and angle of attack. A survey of available unsteady and quasi-steady aerodynamic theories has been conducted to determine their applicability to the space shuttle aeroelasticity problem. Theories investigated include:

a. Unsteady theories

Subsonic

- Strip theory (Reference 2)
- Kernel function (Reference 3)
- Doublet lattice (Reference 4)

Transonic

- Transonic box (Reference 5)

Supersonic

- Mach box (Reference 6)

Hypersonic

- Piston theory (Reference 7)

b. Quasi-steady methods

- Woodward method (Reference 8)
- Modified strip theory (Reference 9)

Table 2-1 summarizes the applicability of these theories when the following effects are significant.

- a. Large body with small aerodynamic surfaces
- b. Airfoil thickness
- c. Body/body and body/wing interference
- d. Control surfaces
- e. Angle-of-attack
- f. High (low) aspect ratios

Table 2-1 indicates that the present state-of-the-art in unsteady aerodynamics is inadequate for analyzing complex configurations such as space shuttle. The Air Force and NASA are continuing to sponsor research in this area and hopefully the picture will brighten in the future. For the meantime, however, when interference effects,

Table 2-1. Applicability of Referenced Theories to Significant Effects

	Theory	Effect					
		a	b	c	d	e	f
Subsonic	Strip Theory	No	No	No	Yes	No	M-H
	Kernel Function	No	No	No	Yes	No	All
	Doublet Lattice	No	No	No	Yes	No	All
Transonic	Box	No	No	No	Yes	No	L-M
Supersonic	Mach Box	No	No	No	Yes	No	L-M
Hypersonic	Piston Theory	Yes	Yes	No*	Yes	Yes	All
Quasi-steady	Woodward	Yes	Yes	Yes	Yes	Yes	All
	Modified Strip Theory	No	No	No	Yes	No	M-H

*Interference effects become small hypersonically

thickness, angle-of-attack, etc. are significant factors and the reduced frequency range of interest is not so high that unsteady lag effects dominate, it is recommended that Woodward's steady aerodynamic method be employed at speeds below hypersonic. Piston theory appears adequate in the hypersonic Mach number range.

The common approach when using steady-state aerodynamics to derive generalized forces for flutter and dynamic response problems is to compute the complex downwash at a point j due to a unit amount of the k^{th} generalized coordinate from the equation:

$$w_{jk} = V\alpha_{jk} + i\omega_k h_{jk} \quad (2-42)$$

where the first term is the downwash due to the flight velocity, V , and the modal angle of attack, α , and the second term is the downwash induced by the surface plunging motion of amplitude h and frequency ω .

The steady-state method of Woodward was applied by Brignac and Shelton (Reference 10) to flutter analysis of the F-111 horizontal stabilizer. Analytical and experimental results were compared for flutter Mach numbers of 1.09 and 1.37. The results are shown in Tables 2-2 and 2-3. At Mach 1.09, where no applicable unsteady aerodynamic theory was available, the predicted flutter velocity using Woodward aerodynamics was 8 percent low and the flutter frequency was 2 percent high. This is remarkable correlation considering the transonic Mach number and the relatively high reduced frequency at flutter (about 0.8 based on the mean semi-chord). At Mach 1.37, the predicted flutter speed using the Woodward method agreed exactly with test results. The predicted flutter frequency was 16 percent high. Unsteady Mach box theory applied to this condition yielded a 3 percent higher flutter speed.

Table 2-2. Comparison of Quasi-Steady and Experimental Flutter Results at Mach 1.09

	Mach No.	Mass-Density Ratio (μ)	$\frac{V_F}{V_F \text{ (test)}}$	$\frac{f_F}{f_F \text{ (test)}}$
Test	1.09	13.10	1.00	1.00
Analysis (Quasi-Steady)	1.09	13.10	0.92	1.02

Table 2-3. Comparison of Quasi-Steady, Unsteady, and Experimental Flutter Results at Mach 1.37

	Mach No.	Mass-Density Ratio (μ)	$\frac{V_F}{V_F \text{ (test)}}$	$\frac{f_F}{f_F \text{ (test)}}$
Test	1.37	12.88	1.0	1.00
Unsteady (Mach Box)	1.37	12.88	1.03	1.00
Quasi-Steady (Woodward)	1.37	12.8	1.00	1.16

It becomes evident that in some cases the use of steady-state aerodynamics yields more accurate flutter calculations than does unsteady aerodynamic theory. Apparently, unsteady lag effects are sometimes less important than the proper definition of steady-state effects due to interference, thickness, angle of attack, etc. The problem then becomes one of defining the steady-state aerodynamic pressure distribution. As shown in Figures 2-7 through 2-9 taken from Reference 11, the Woodward method appears to have excellent potential in this regard.

2.4 PROPELLANT SLOSHING AND ENGINE DYNAMICS

Propellant sloshing is accounted for using the method presented in Reference 12, which defines a "sloshing mass" distribution along the length of the tank. A spring-mass representation is applied at the center of gravity of the sloshing mass. Spring stiffness, k_s , is given by:

$$k_s = m_s \omega_s^2 \quad (2-43)$$

where m_s is the sloshing mass and ω_s is the slosh frequency.

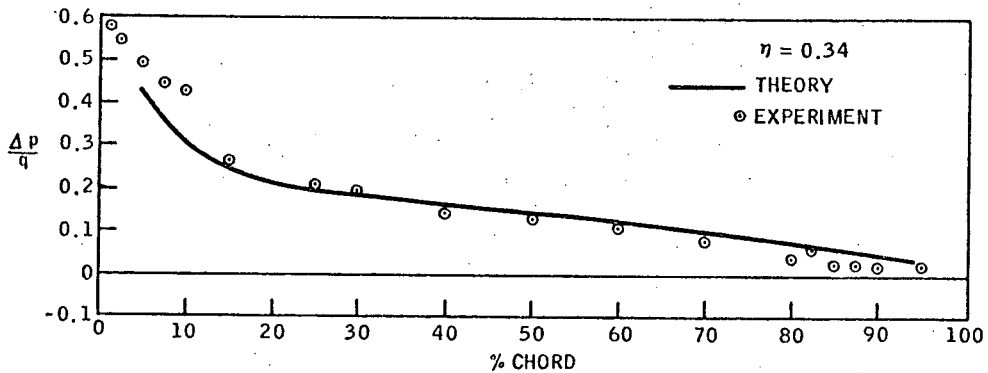
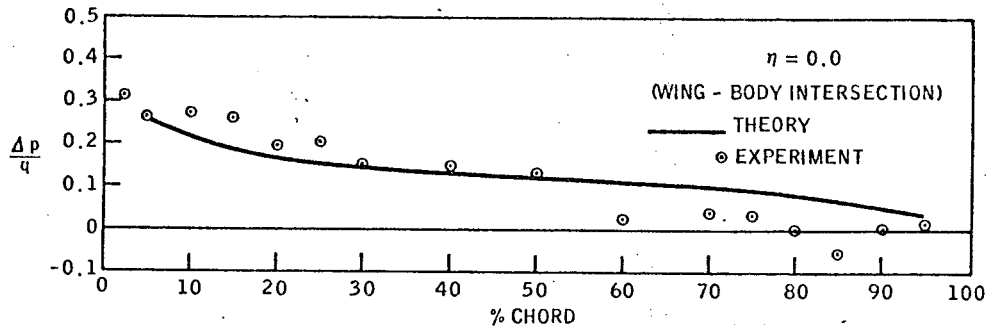


Figure 2-7. Pressure Difference Distribution on B-58 Wing for Wing-Fuselage-Fin Configuration ($\alpha = 4$ deg, Mach 0.8)

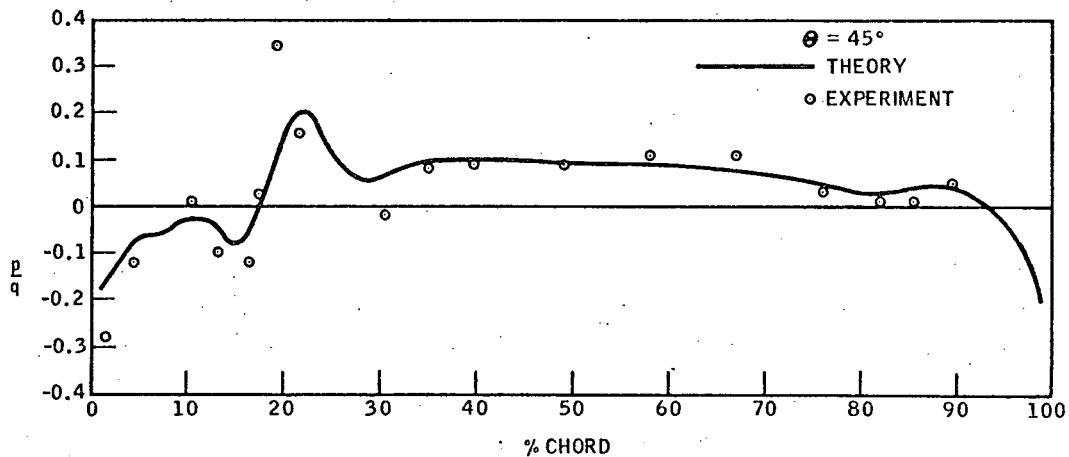


Figure 2-8. Fuselage Pressure Distribution for B-58 Wing-Fuselage-Fin Configuration ($\alpha = 4$ deg, Mach 0.8, $\beta = 0$ deg)

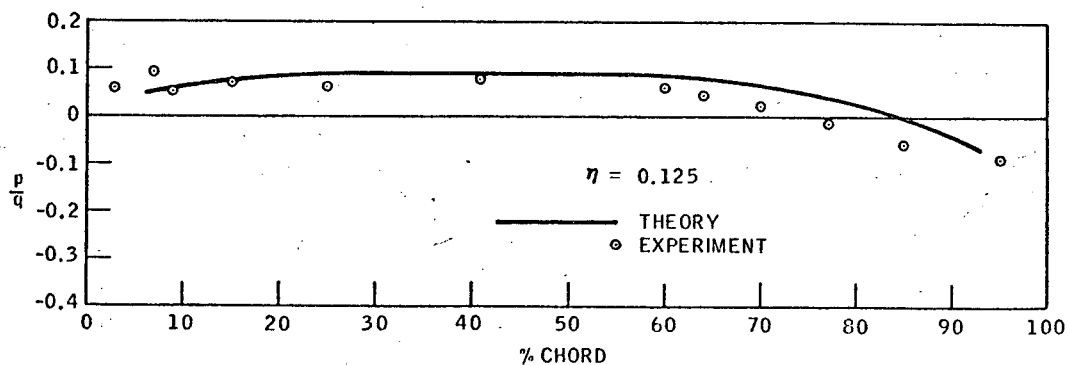


Figure 2-9. Fin Pressure Distribution for B-58 Wing-Fuselage-Fin Configuration ($\alpha = 4$ deg, Mach 0.8, $\beta = 0$ deg)

There are two methods for including sloshing in the vehicle dynamics. The slosh spring-mass system can be included in the mathematical model used for the vehicle modal analysis, or it can be mass-coupled to the normal modes derived based on rigid propellant. In the latter technique, the terms in the generalized mass matrix that couple the vehicle modes to the slosh modes are given by:

$$M_{is} = m_s \phi_{is} \quad (2-44)$$

where M_{is} is the generalized mass term coupling the i^{th} vehicle mode to the slosh mode and ϕ_{is} is the deflection of the slosh mass due to vehicle mode i .

The thrust force acting normal to the booster centerline (assuming small angles) is:

$$F_T = -T (\theta + \delta) \quad (2-45)$$

where T is the engine thrust, θ is the slope at the gimbal point, and δ is the engine gimbal angle relative to the deformed centerline as shown in Figure 2-10.

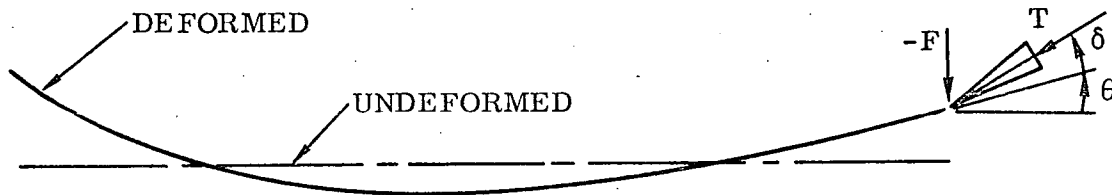


Figure 2-10. Engine Gimbal Sign Convention

The slope of the deformed centerline at the gimbal point is given by:

$$\theta(t) = \sum_{r=1}^n h'_r q_r(t) \quad (2-46)$$

where h'_r is the r^{th} modal slope at the gimbal point and q_r is the r^{th} generalized coordinate.

Substituting Equation 2-46 into 2-45 yields:

$$F_T = -T \left(\sum_{r=1}^n h'_r q_r + \delta \right) \quad (2-47)$$

The i^{th} generalized force due to thrust is given by:

$$\bar{Q}_{T_i} = -T \left(\sum_{r=1}^n h_r' q_r + \delta \right) h_i \quad (2-48)$$

where h_i is the i^{th} modal deflection at the gimbal point.

The inertia force at the engine cg due to engine gimbaling is:

$$F_I = -m \ell \ddot{\delta} \quad (2-49)$$

where m is the mass of the engine and ℓ is the distance from the gimbal point to the engine cg.

The inertia moment about the engine cg is:

$$M_I = I \ddot{\delta} \quad (2-50)$$

where I is the engine mass moment of inertia about the engine cg. The generalized inertia force acting on mode i is written:

$$\bar{Q}_{I_i} = F_I (h_i - \ell h_i') + M_I h_i' \quad (2-51)$$

Substituting Equations 2-49 and 2-50 into 2-51 yields:

$$\bar{Q}_{I_i} = \left[-m \ell h_i + (m \ell^2 + I) h_i' \right] \ddot{\delta} \quad (2-52)$$

which can be rewritten:

$$\bar{Q}_{I_i} = (-m \ell h_i + I_g h_i') \ddot{\delta}$$

where I_g is the engine mass moment of inertia about the gimbal point, i.e.:

$$I_g = m \ell^2 + I \quad (2-53)$$

The total generalized force acting on mode i due to the gimballed engine is then:

$$\begin{aligned} \bar{Q}_i &= \bar{Q}_{T_i} + \bar{Q}_{I_i} = -T \left(\sum_{r=1}^n h_r' q_r + \delta \right) h_i \\ &\quad + (-m \ell h_i + I_g h_i') \ddot{\delta} \end{aligned} \quad (2-54)$$

Assuming harmonic motion and dividing Equation 2-54 by $4 \rho b^3 \omega^2$ yields:

$$Q_i(\omega) = \frac{\bar{Q}_i(\omega)}{4 \rho b^3 \omega^2}$$

$$= \frac{1}{4 \rho b^3} \left[- \frac{T \sum_{r=1}^n h_r' q_r(\omega) h_i}{\omega^2} + \left(m \ell h_i - I_g h_i' - \frac{T}{\omega^2} \right) \delta(\omega) \right] \quad (2-55)$$

which can be written in matrix form as:

$$\{Q(\omega)\} = \{M_{\delta_1}\} \delta_1(\omega) + \{Q_{\delta_2}(\omega)\} \delta_2(\omega) \quad (2-56)$$

where:

$$\{M_{\delta_1}\} = \{h\}$$

$$\delta_1(\omega) = - \frac{T}{4 \rho b^3 \omega^2} [h'] \{\bar{q}(\omega)\}$$

$$\{Q_{\delta_2}(\omega)\} = \frac{1}{4 \rho b^3} \left\{ m \ell \{h\} - I_g \{h'\} - \frac{T}{\omega^2} \{1\} \right\}$$

$$\delta_2(\omega) = \delta(\omega)$$

Incorporating these expressions into the equations of motion parallels exactly the method outlined in Section 2.2.

SECTION 3

COMPUTER PROGRAM DESCRIPTION

A computer program, based on the equations presented in Chapter 2, has been written to calculate the response of an elastic aerospace vehicle to random and discrete turbulence. The program, documented in Reference 1, is written in Fortran IV for the UNIVAC 1108 and CDC 6400 computers.

Inputs to the program consist of modal data, generalized aerodynamic forces, control system description, flight data, and discription of the disturbing function. Program outputs include tabulations of \bar{A} and N_0 and SC 4020 plots of transfer functions, response power spectral densities, and Nyquist stability traces. Response time histories are plotted for the discrete turbulence case. The program is dimensioned to have the following capabilities.

- 20 generalized coordinates,
- 20 structural response parameters,
- 20 reduced frequencies,
- 10 interpolated points between input reduced frequencies
(for a total of 210 response frequencies).

The following features add to the usefulness of the program.

- a. Most large data blocks can be input or output on magnetic tape.
- b. Most of the equations contain input scalar multipliers.
- c. Several standard input power spectral density functions are available in the program; in addition, the user may construct his own using straight-line segments.
- d. Several common time-varying forces are available or the user may construct his own.
- e. Extensive use is made of the SC 4020 plotter.
- f. A comprehensive error routine assists in finding input errors.
- g. Provisions are made to compute quasi-steady forces from steady-state aerodynamic input data.
- h. Ten types of control system elements are available for defining the stability augmentation system (SAS).

The digital computer program is divided into six main parts:

Part 0 computes the dynamic matrix representing the vehicle SAS.

Part 1 interpolates the aerodynamic terms and calculates the response of the generalized coordinates.

Part 2 computes the transfer functions.

Part 3 determines the response to a random input.

Part 4 calculates the response to a discrete input.

Part 5 plots the results of Parts 2, 3, and/or 4 on the SC 4020 plotter.

The program is set up such that Part 0 is run independently and Parts 1 through 5 are run independently or in series.

The input to the program can consist of problem cards and magnetic tape. Program output consists of user-specified combinations of printed information, punched cards, magnetic tape, and SC 4020 plots.

Section 4 presents the results of an application of this program to the turbulence response analysis of a typical space shuttle configuration.

SECTION 4

PRELIMINARY RESULTS OF SPACE SHUTTLE TURBULENCE RESPONSE ANALYSIS

A typical space shuttle configuration was analyzed to determine its response to random turbulence. The configuration consists of the delta wing booster and the straight wing orbiter shown in Figure 4-1. During ascent flight, prior to separation, the orbiter is carried "piggyback" by the booster.

Symmetric and antisymmetric responses were computed at a point on the ascent trajectory corresponding to 0.9 Mach and 22,800 feet altitude. Symmetric response of the booster during flyback was determined at 0.9 Mach and 40,000 feet altitude.

For both the ascent and the booster return flight analyses, the Von Karman gust spectrum was assumed with a 2500-foot scale of turbulence.

The analyses were conducted with the stability augmentation system (SAS) both operative and inoperative. Autopilot gains and sensor locations were assumed without the aid of an elastic vehicle control stability analysis. The unaugmented vehicle results are therefore more realistic. No attempt was made in the present study to optimize the SAS. In some SAS-on cases, instabilities are suggested by plots of the stability determinant.

Vibration modes were computed using a finite element method developed at Convair Aerospace. For these mode shapes, unsteady aerodynamic forces were generated using the kernel function theory (Reference 3) for the aerodynamic surfaces and slender body quasi-steady aerodynamics (Reference 7) for the body.

4.1 BOOSTER RETURN FLIGHT

Referring to Figure 4-2, the rigid body equations of motion are as follows for transient pitch plane disturbances:

$$\ddot{Z} - \dot{\theta} V = - \frac{QSg}{W} \left(C_{L\alpha} \alpha + C_{L\delta_E} \delta_E \right) \quad (4-1)$$

$$\ddot{\theta} = \frac{QS\bar{c}}{I} \left(C_{M\alpha} \alpha + C_{M\delta_E} \delta_E \right) \quad (4-2)$$

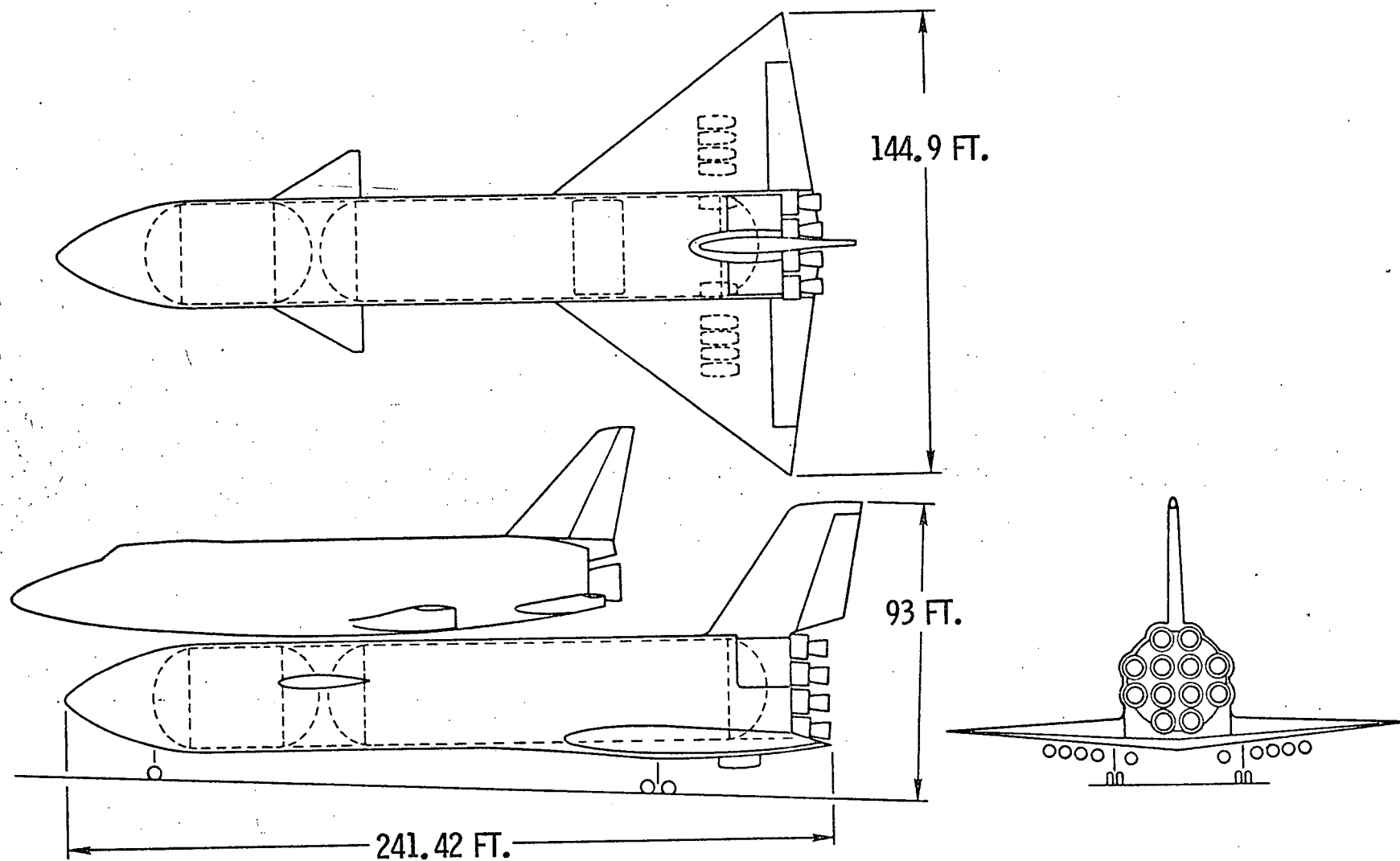


Figure 4-1. Booster Configuration

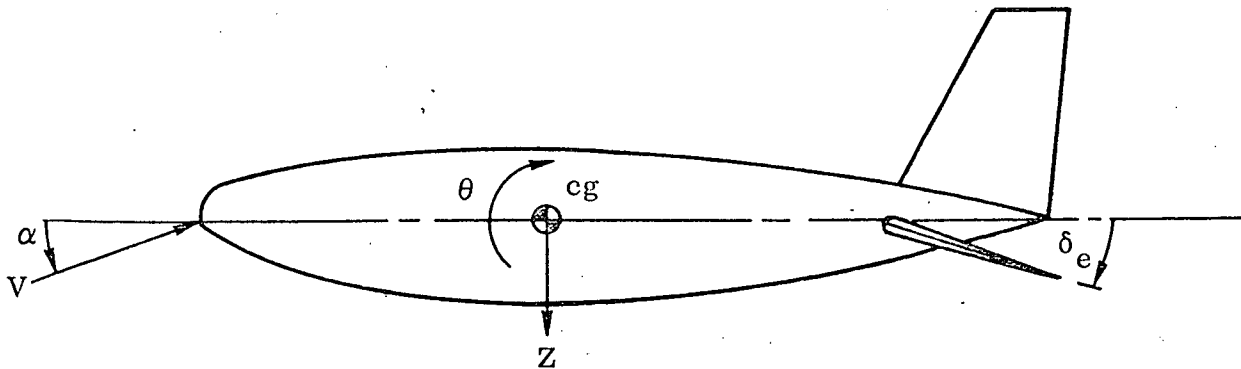


Figure 4-2. Pitch Plane Sign Convention

where

\ddot{Z} is normal acceleration of the cg (ft/sec²)

$\ddot{\theta}$ is pitch acceleration (rad/sec²)

Q is dynamic pressure (lb/ft²)

S is reference area (ft²)

g is acceleration due to gravity (ft/sec²)

W is weight (lb)

\bar{c} is reference length (ft)

I is mass moment of inertia about the cg (slug-ft²)

$C_{L_{\alpha}}$ is the derivative of the lift coefficient with respect to angle of attack (per rad)

$C_{L_{\delta_E}}$ is the derivative of the lift coefficient with respect to elevon deflection angle (per rad)

$C_{M_{\alpha}}$ is the derivative of the pitching moment coefficient with respect to angle of attack (per rad)

$C_{M_{\delta_E}}$ is the derivative of the pitching moment coefficient with respect to elevon deflection angle (per rad)

V is the flight velocity (ft/sec)

δ_E is elevon deflection angle (rad)

α is the angle of attack (rad)

$$\alpha = \frac{\dot{Z}}{V} + \alpha_{\text{gust}}$$

The booster flyback pitch plane SAS block diagram is shown in Figure 4-3. The control equation is:

$$\tau_A \dot{\delta}_E + \delta_E = K_A (K_\theta \theta + K_{\dot{\theta}} \dot{\theta} - K_{\ddot{Z}} \ddot{Z}) \quad (4-3)$$

where

τ_A is the elevon actuator time constant (sec)

K_A is the elevon actuator gain (rad/rad)

K_θ is the pitch displacement gain (rad/rad)

$K_{\dot{\theta}}$ is the pitch rate gain (rad/rad/sec)

$K_{\ddot{Z}}$ is the normal acceleration feedback gain (rad/ft/sec²)

It is assumed that the canard is used for trim only and that the SAS sensors are located at the cg.

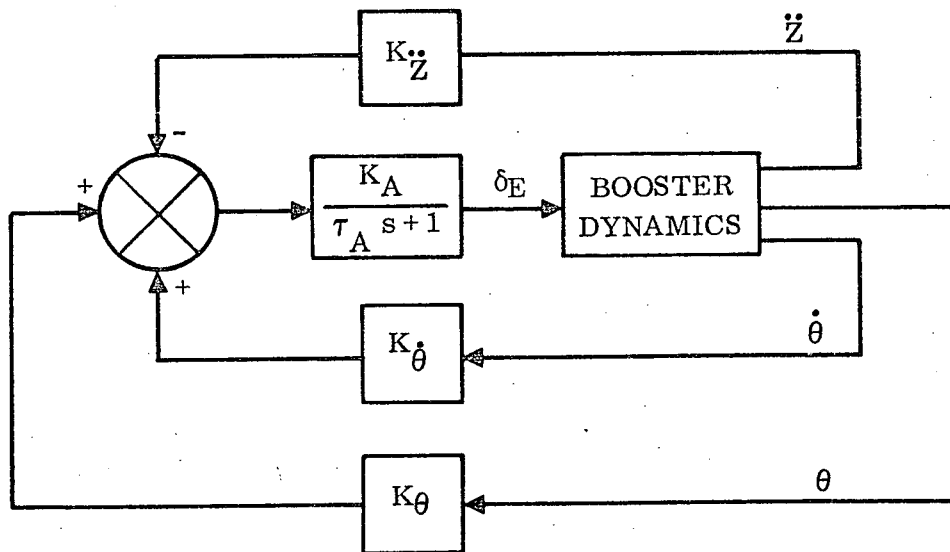


Figure 4-3. Booster Flyback Pitch Plane SAS

Numerical values for the booster flyback configuration are listed in Table 4-1.

The booster finite element model used for the modal analysis represents the aerodynamic surfaces as a redundant network of spars and ribs and the fuselage as a 12 grid-point beam. Canard idealization is shown in Figure 4-4. Beam segments represent spars and ribs. Plate elements are used for the cover skins. Solid lines represent locations of physical members and dashed lines indicate members added for analysis purposes. The solid circles show locations of masses in the simulation. The member extending inboard from grid point 167 is the pivot shaft.

Table 4-1. Data for the Booster Return Flight Analysis

Mach Number	0.9	$C_{L\alpha}$	2.3 per rad
Altitude	40,000 ft	$C_{M\alpha}$	-0.029 per rad
Q	224 lb/ft ²	$C_{L\delta_E}$	0.435 per rad
V	874 ft/sec	$C_{M\delta_E}$	-0.326 per rad
S	7791 ft ²	τ_A	0.0667 sec
\bar{c}	71.69 ft	K_A	4.0 rad/rad
W	694,435 lb	K_θ	1.0 rad/rad
I	84.307×10^6 slug-ft ²	$K_{\dot{\theta}}$	1.0 rad/rad/sec
cg Location	2013 inches aft of nose	$K_{\ddot{z}}$	0.124 rad/ft/sec ²

Wing idealization is shown in Figure 4-5. Grid points 124, 127, 130, 133, and 136 represent the airbreathing engines. The actual wing is covered with corrugated skin. It was assumed that the skin was fully ineffective in bending and only partially effective in carrying shear. The idealized wing is suspended from the fuselage by springs located at grid points 19, 21, 23, and 27.

The first eight symmetric mode shapes for the booster return configuration are shown in Figures 4-6 through 4-13. The first mode is wing bending, and the second and third are combinations of wing torsion and fuselage bending. The fourth mode is canard pitch.

Results of the turbulence response analysis for booster return symmetric flight without the SAS are summarized in Table 4-2. For the one-degree-of-freedom (DOF) analysis, only rigid-body vertical translation is considered. For the two-DOF analysis, the rigid body pitch mode is included. The 10-DOF case considers the two rigid body modes and first eight elastic modes of the vehicle. As can be seen in the table, elastic modes are required to predict the response properly.

Figure 4-14 shows \bar{A} and N_0 for normal acceleration at points along the fuselage. Except for the nose region, the two-DOF case adequately predicts the \bar{A} distribution but not the N_0 values.

To lend more physical insight to the results shown in Figure 4-14, assume a design rms gust velocity of 50 feet per second. The rms normal acceleration at the booster nose is then 0.5 g.

Acceleration transfer functions for three points on the fuselage are shown in Figures 4-15 through 4-17. Corresponding PSD plots are given in Figures 4-18 through 4-20.

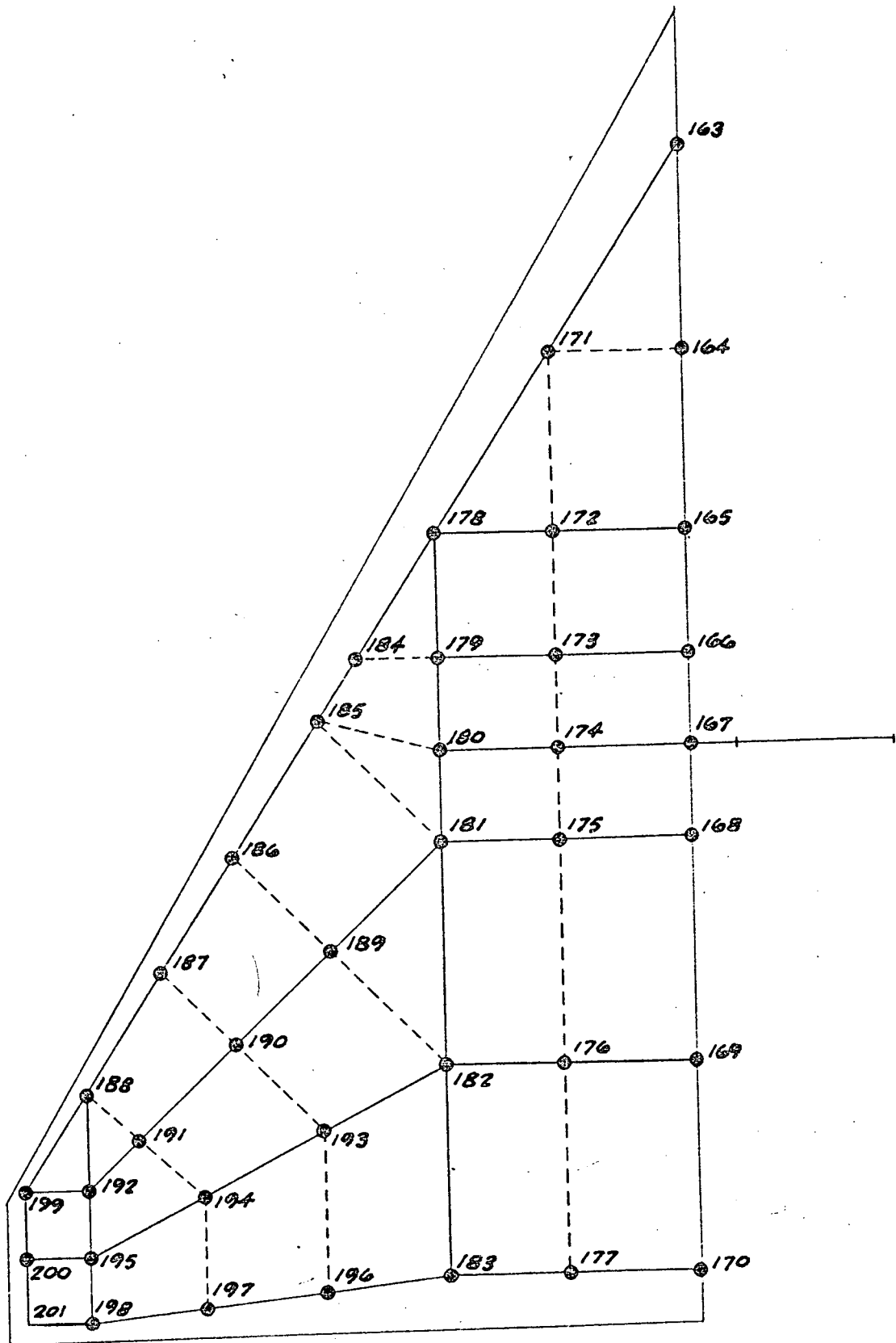


Figure 4-4. Booster Canard Structural Idealization

Table 4-2. Booster Return Flight Load Summary (SAS Off, Symmetric)

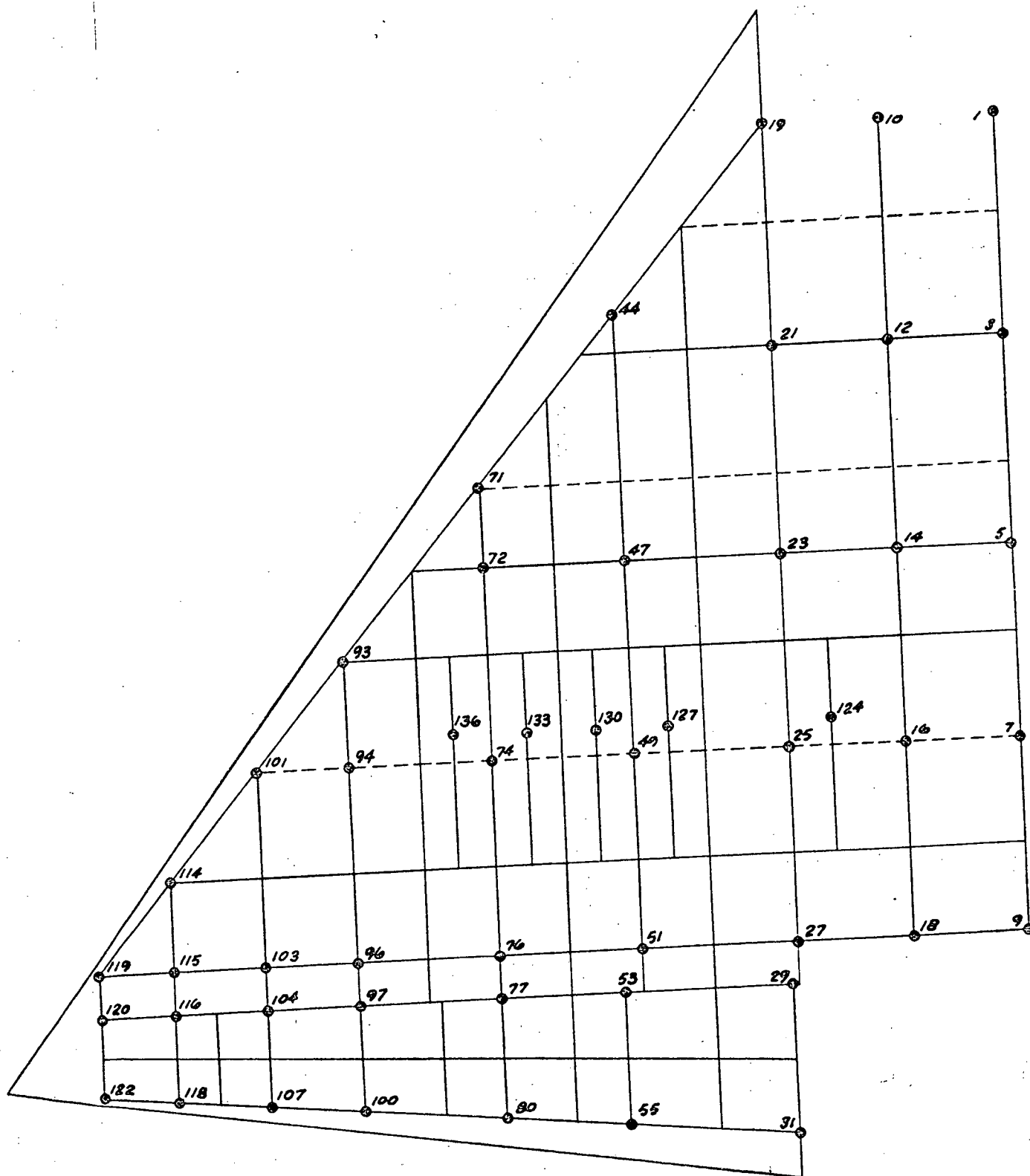
Response Item	1 DOF		2 DOF		10 DOF	
	\bar{A}	N_o (Hz)	\bar{A}	N_o (Hz)	\bar{A}	N_o (Hz)
Wing Root Shear (lb)	1008.0	0.780	1331.1	0.577	1174.6	1.217
Wing Root Bending Moment (in-lb)	290,000	0.835	382,810	0.622	334,730	1.318
Wing Root Torque About FS 3488.5 (in-lb)	41,424	2.789	48,819	2.38	157,760	3.828
Fuselage Shear at FS 2800 (lb)	729.6	0.983	915.28	0.964	843.5	1.422
Fuselage Bending Moment at FS 2800 (in-lb)	350,000	1.511	251,780	1.181	413,210	3.829

The transfer functions for fuselage shear and bending moment at fuselage station (FS) 2800 are shown in Figures 4-21 and 4-22, respectively. The corresponding PSD curves are contained in Figures 4-23 and 4-24. Wing root shear, bending moment, and torque about FS 3488.5 are shown in Figures 4-25 through 4-27, respectively. Figures 4-28 through 4-30 are the corresponding response PSD plots.

An indication of the vehicle stability with SAS off is shown in Figures 4-31 and 4-32. Figure 4-31 is a plot of the magnitude and phase angle of the determinant of the A-matrix evaluated over the frequency range of interest, where the A-matrix is defined by Equation 2-5a. A polar plot of the same information is given in Figure 4-32, which is analogous to a Nyquist stability diagram. The continuous counterclockwise encirclements of the origin indicate that the system is stable throughout the frequency range (Reference 13).

Calculations with the SAS on considered the rigid body vertical translation and pitch modes and the first six elastic modes. Acceleration transfer functions for the three fuselage points are shown in Figures 4-33 through 4-35. The corresponding PSD curves are given in Figure 4-36 through 4-38. Figure 4-39 shows the \bar{A} and N_o values for fuselage normal acceleration versus fuselage station. Comparing the accelerations with those shown in Figure 4-14 for SAS off indicates that SAS suppresses the elastic mode response. With SAS on, nose acceleration is reduced to one-half the SAS-off value and the characteristic frequency over the forward three-fourths of the vehicle is reduced considerably.

The SAS-on A-matrix determinant characteristics are shown in Figure 4-40 and 4-41. Erratic behavior in the range of 4 to 4.5 Hz suggests a system instability.



Frequency = 3.18 Hz

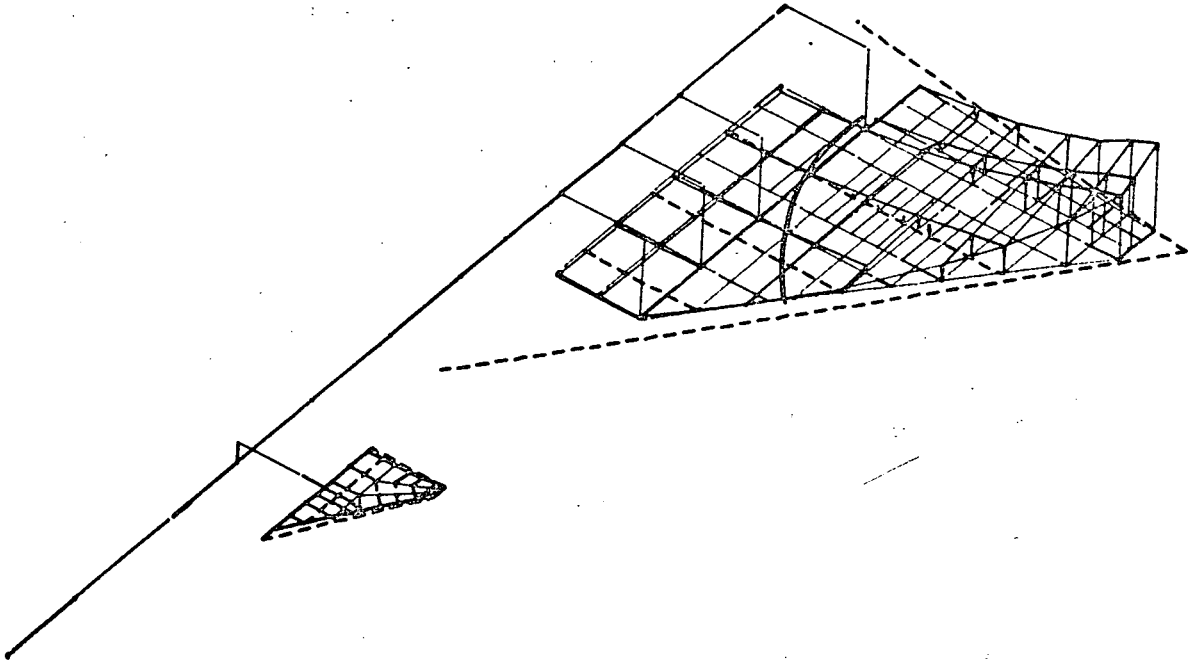


Figure 4-6. Booster Return Flight, First Symmetric Mode

Frequency = 4.27 Hz

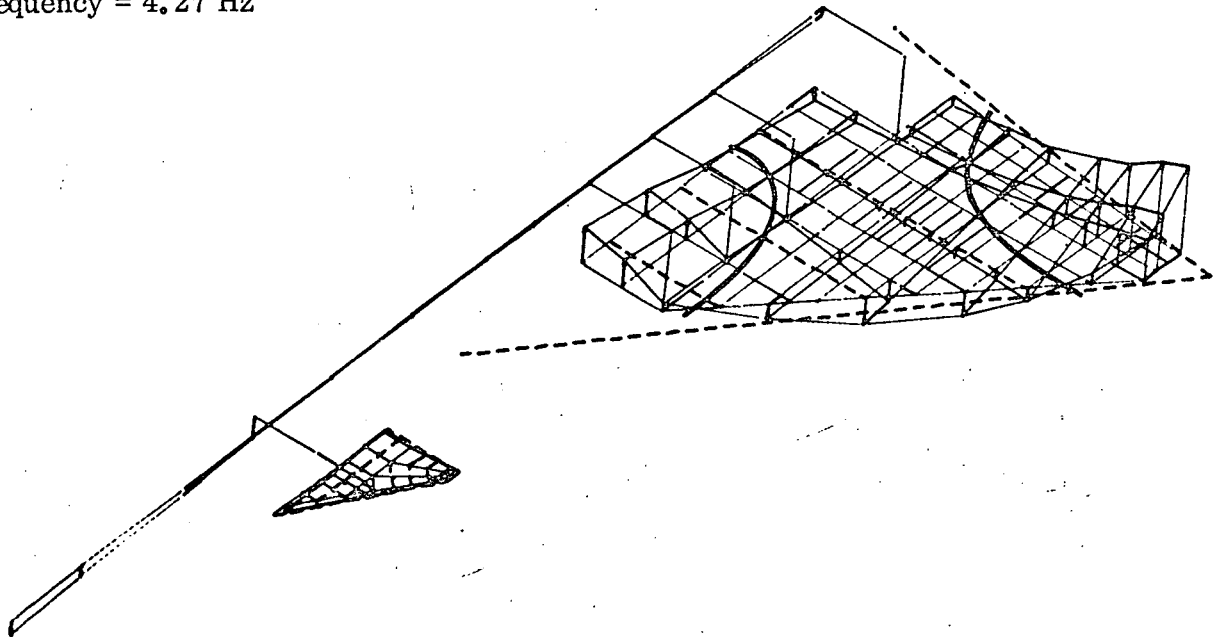


Figure 4-7. Booster Return Flight, Second Symmetric Mode

Frequency = 5.47 Hz

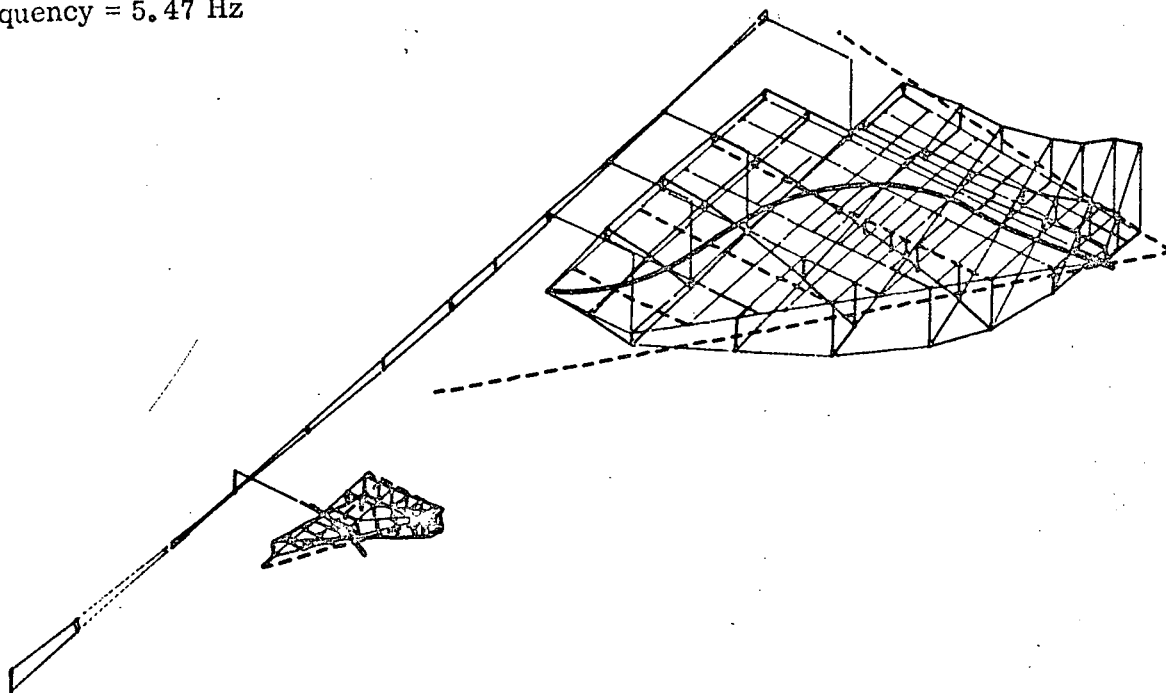


Figure 4-8. Booster Return Flight, Third Symmetric Mode

Frequency = 6.28 Hz

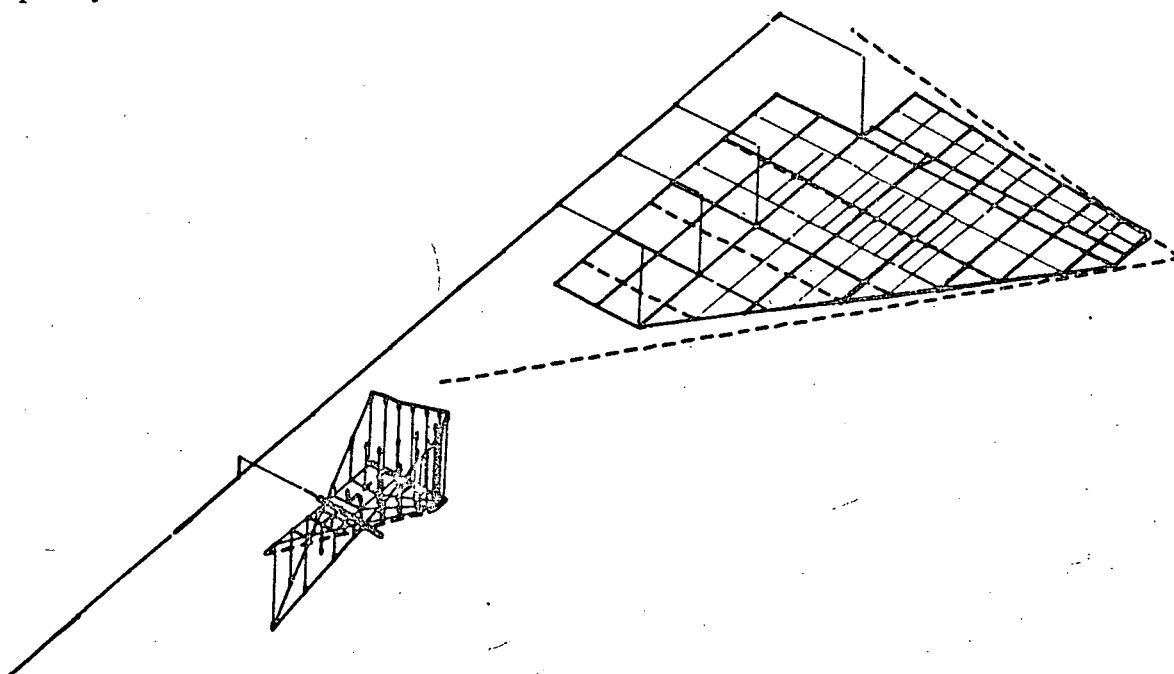


Figure 4-9. Booster Return Flight, Fourth Symmetric Mode

Frequency = 7.04 Hz

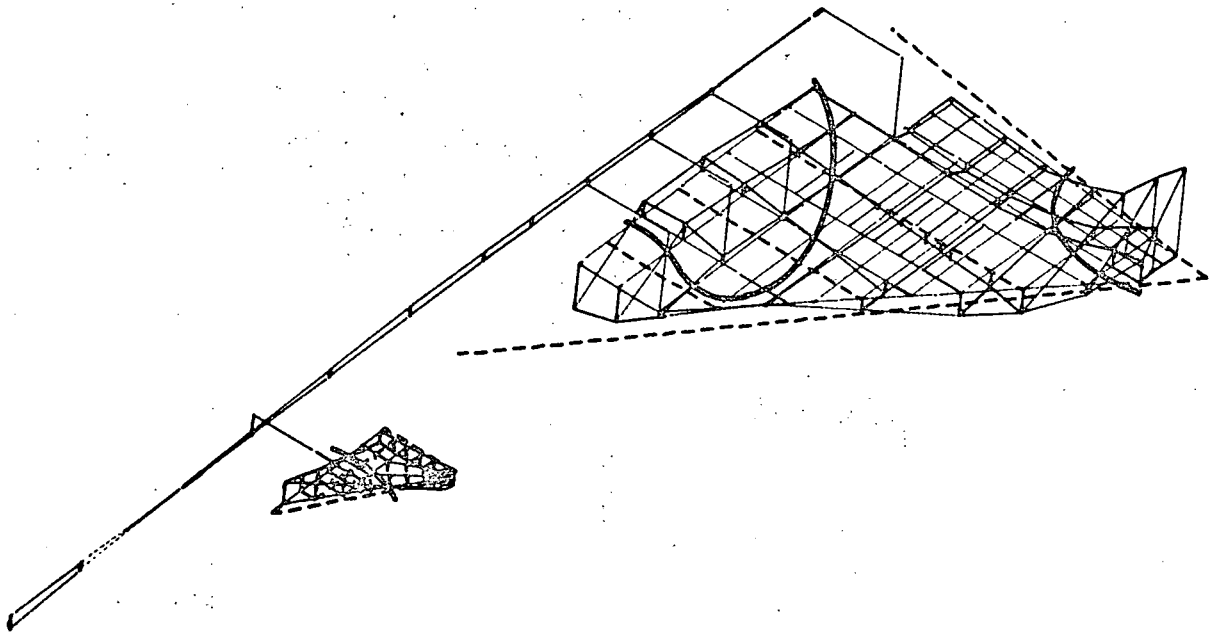


Figure 4-10. Booster Return Flight, Fifth Symmetric Mode

Frequency = 7.22 Hz

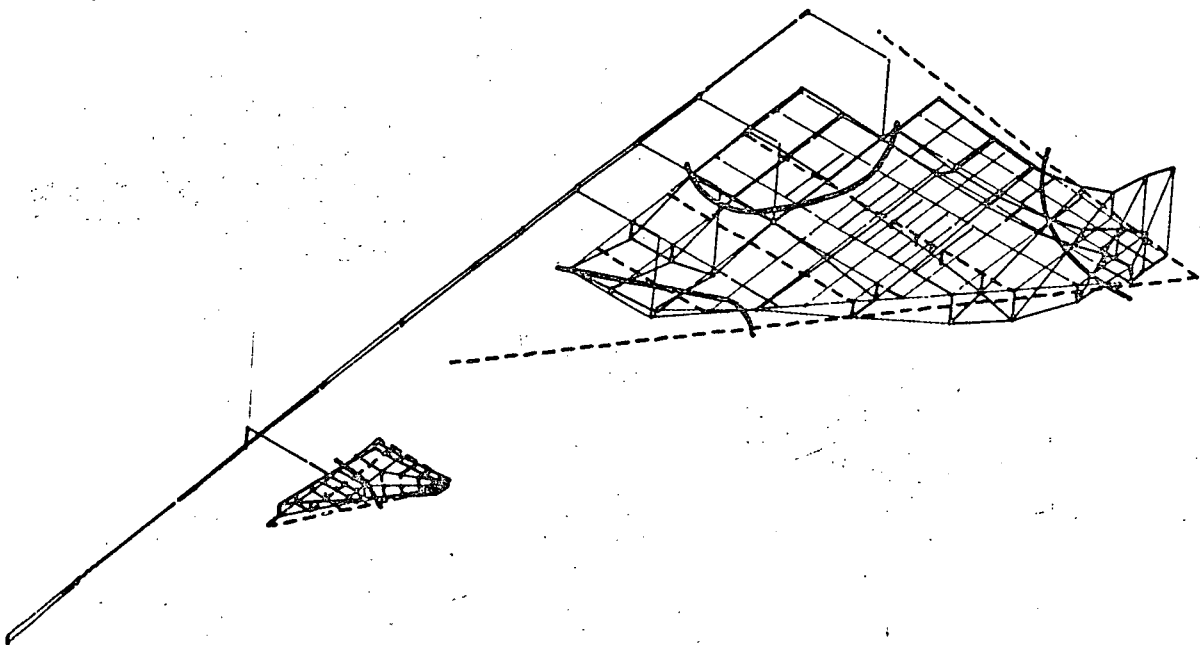


Figure 4-11. Booster Return Flight, Sixth Symmetric Mode

Frequency = 9.57 Hz

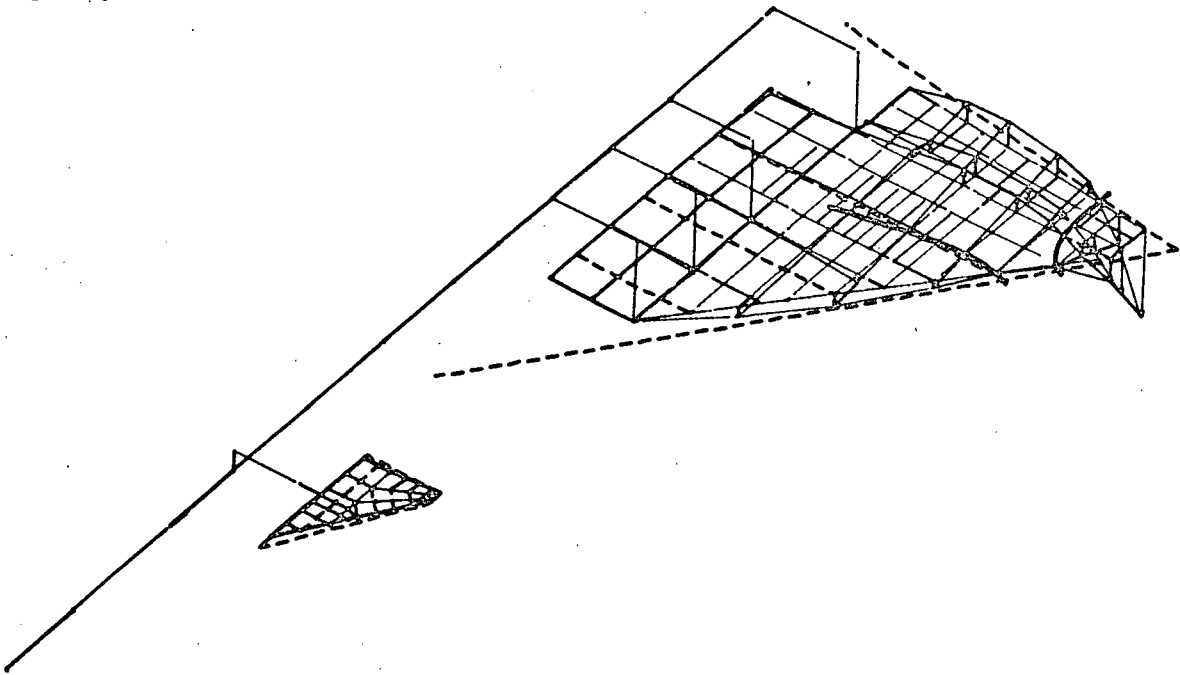


Figure 4-12. Booster Return Flight, Seventh Symmetric Mode

Frequency = 13.03 Hz

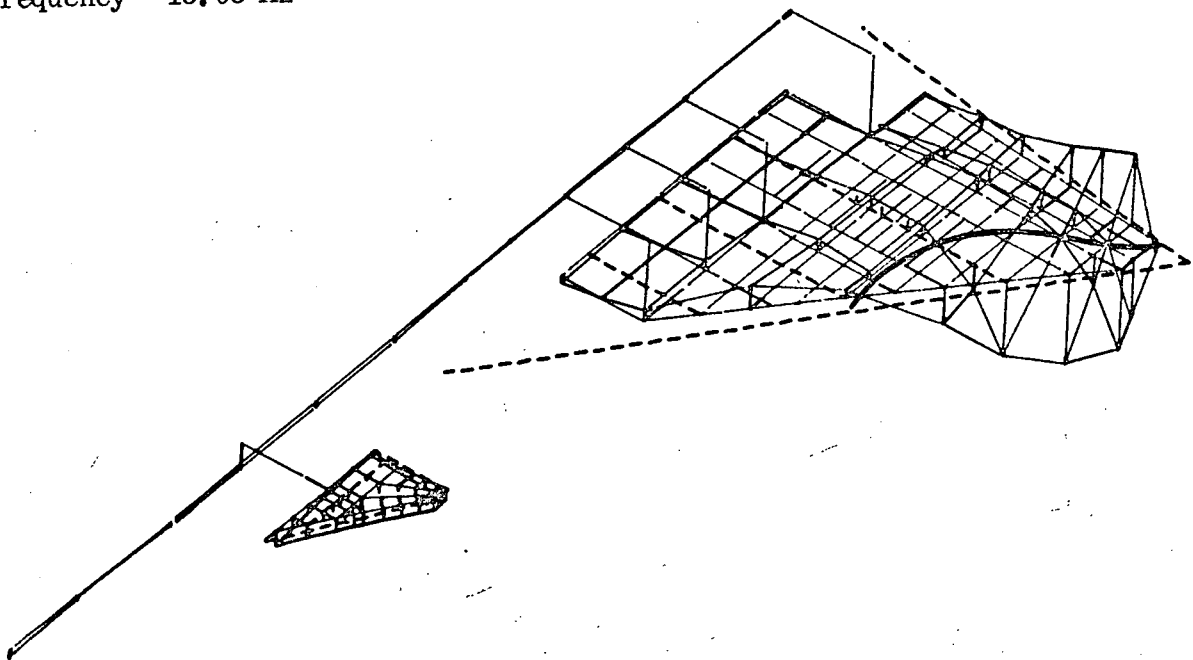


Figure 4-13. Booster Return Flight, Eighth Symmetric Mode

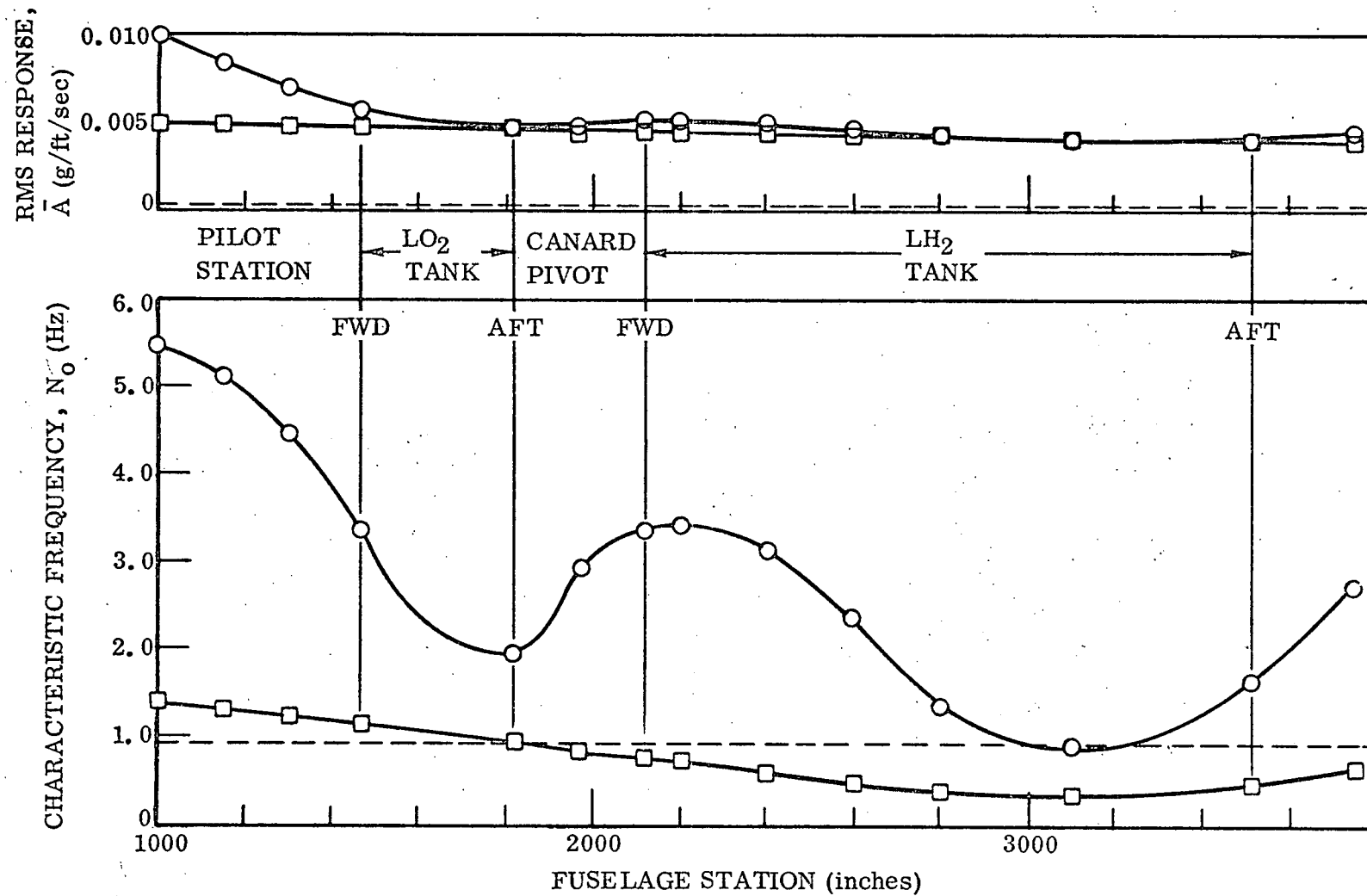


Figure 4-14. Booster Return Flight Fuselage Acceleration \bar{A} and N_0 (SAS Off, Symmetric)

PT. 2 ACC. AT F.S. 1150 CREW STATION
 CIRCLE = 1 DOF PLUS = 2 DOF X = 10 DOF

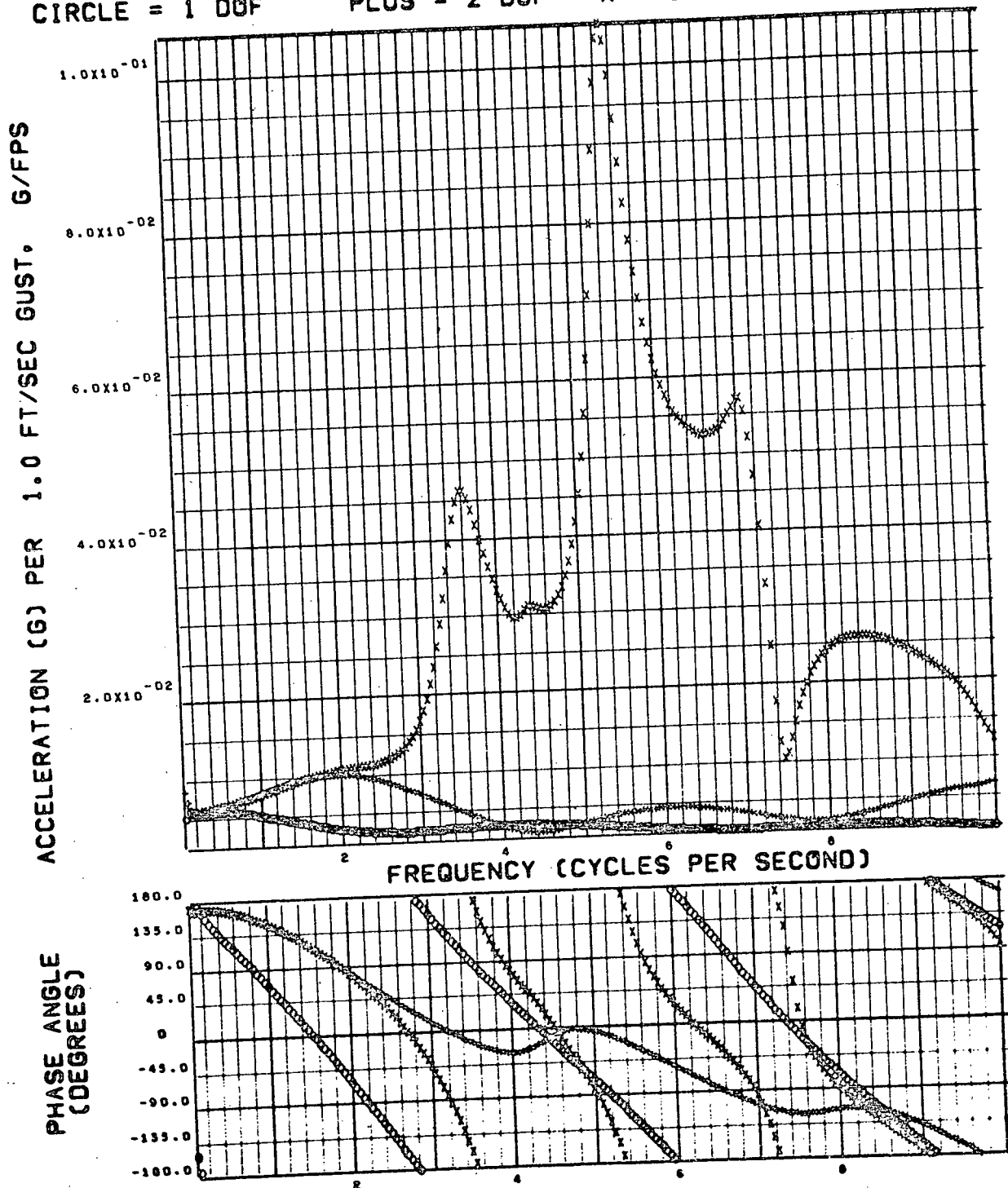


Figure 4-15. Booster Return Flight Fuselage Acceleration Transfer Function (SAS Off, Symmetric) at Crew Station

PT. 5 ACC. AT F.S. 1814 LOX TANK - AFT BLK
 CIRCLE = 1 DOF PLUS = 2 DOF X = 10 DOF

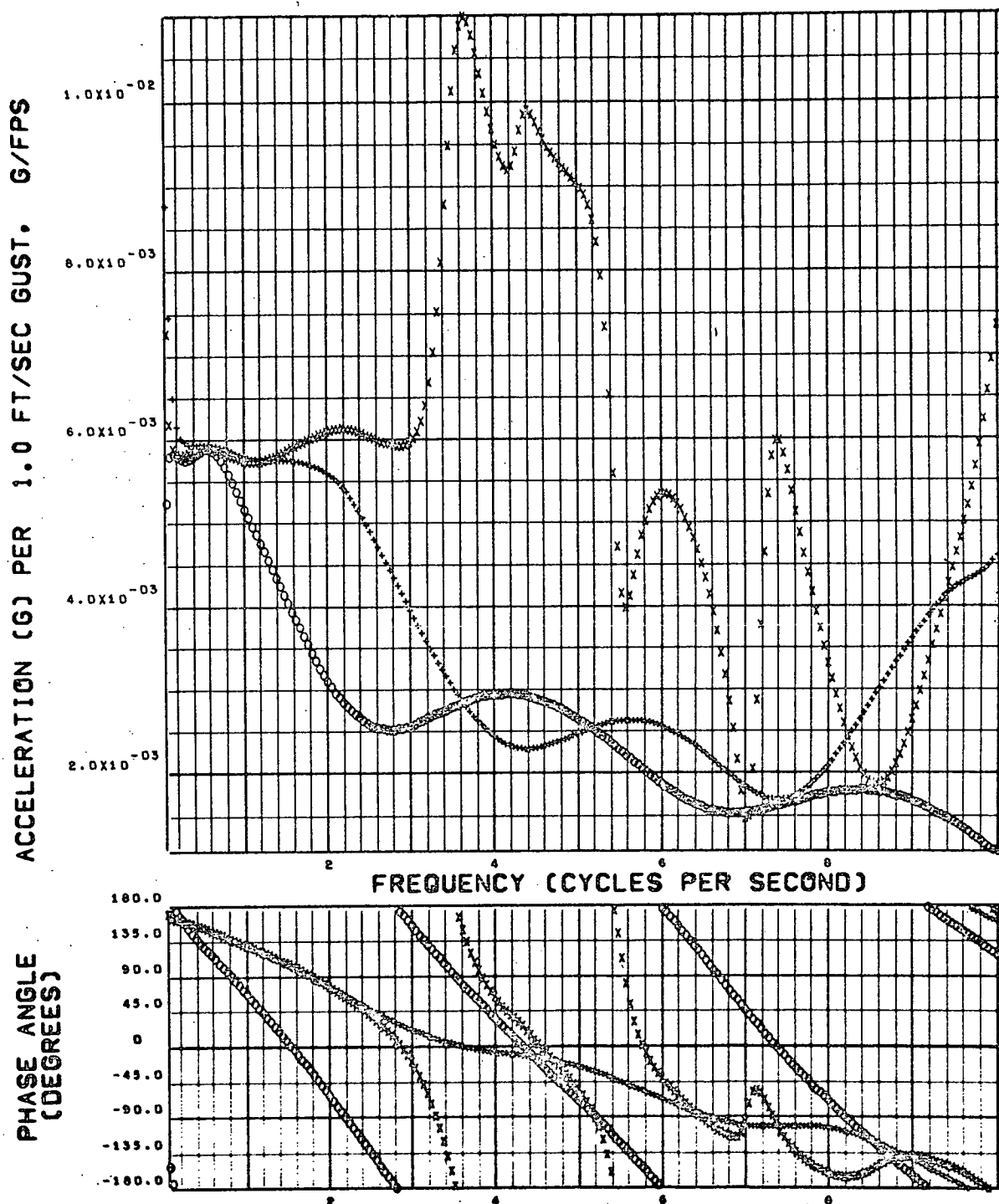


Figure 4-16. Booster Return Flight Fuselage Acceleration Transfer Function (SAS Off, Symmetric) at LO₂ Tank

PT. 13 ACC. AT F.S. 3514 LH2 TANK - AFT BLK
 CIRCLE = 1 DOF PLUS = 2 DOF X = 10 DOF

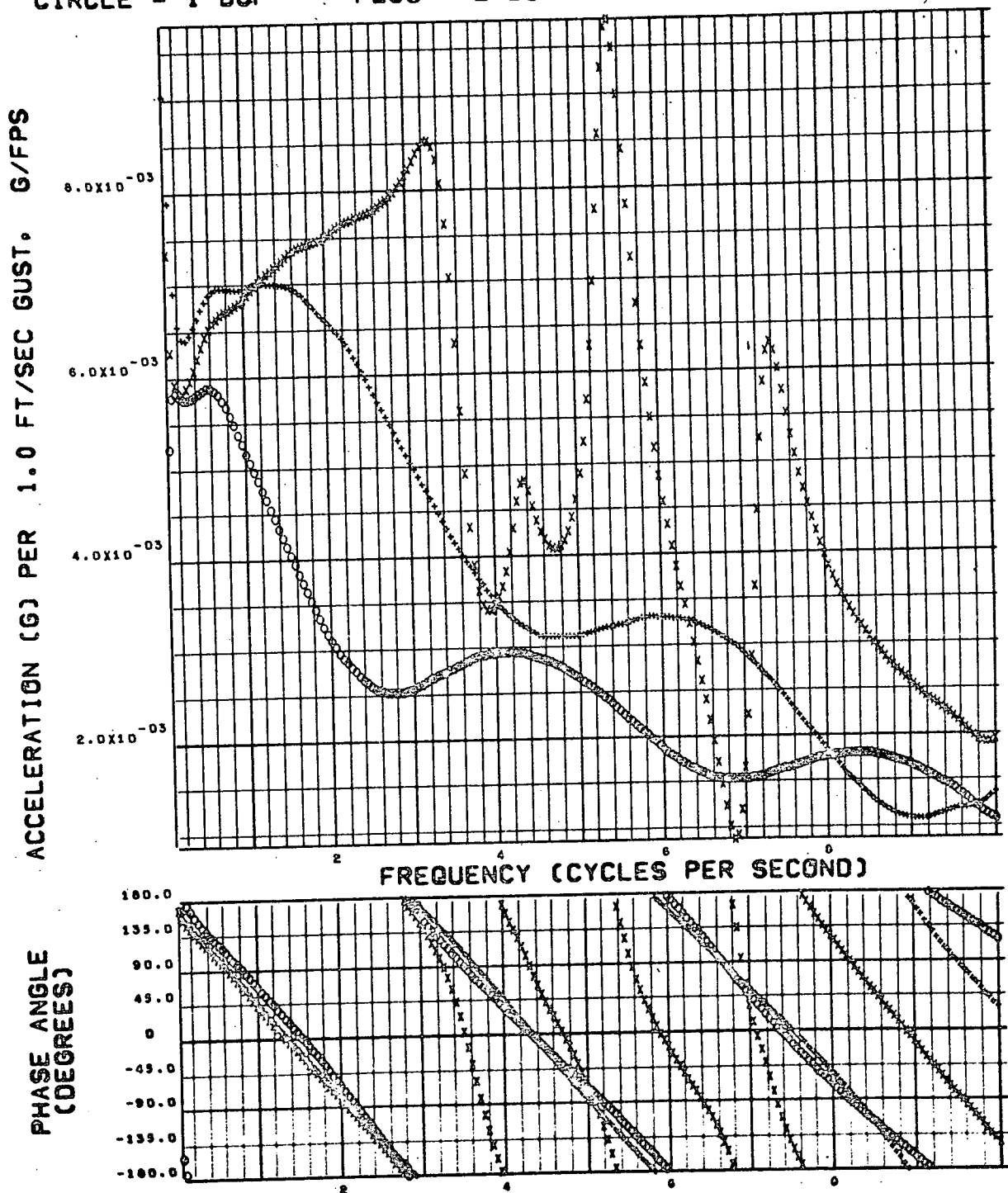


Figure 4-17. Booster Return Flight Fuselage Acceleration Transfer Function (SAS Off, Symmetric) at LH₂ Tank

PT. 2 ACC. AT F.S. 1150 CREW STATION
 CIRCLE = 1 DOF PLUS = 2 DOF X = 10 DOF

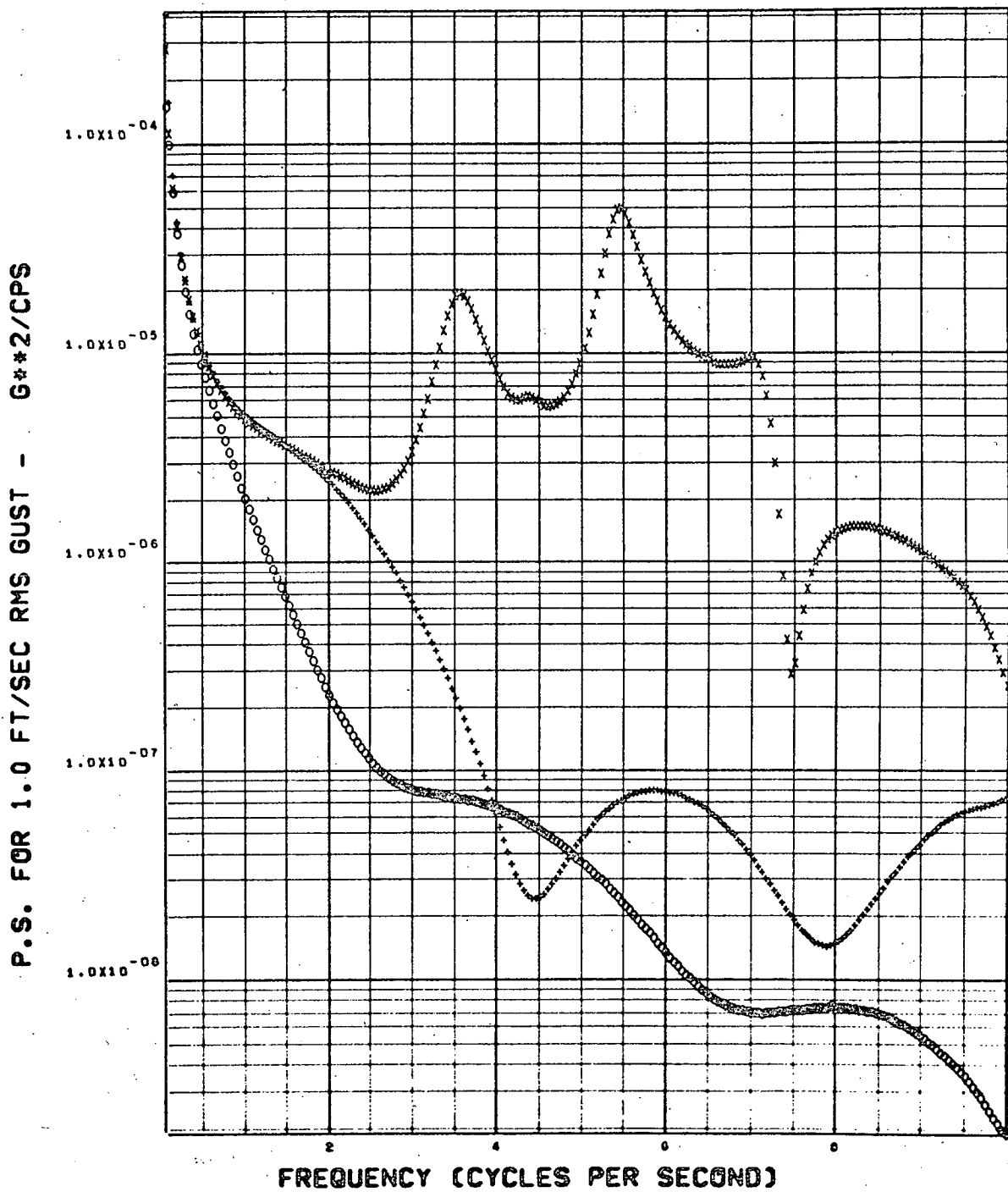


Figure 4-18. Booster Return Flight Fuselage Acceleration
 PSD (SAS Off, Symmetric) at Crew Station

PT. 5 ACC. AT F.S. 1814 LOX TANK - AFT BLK
 CIRCLE = 1 DOF PLUS = 2 DOF X = 10 DOF

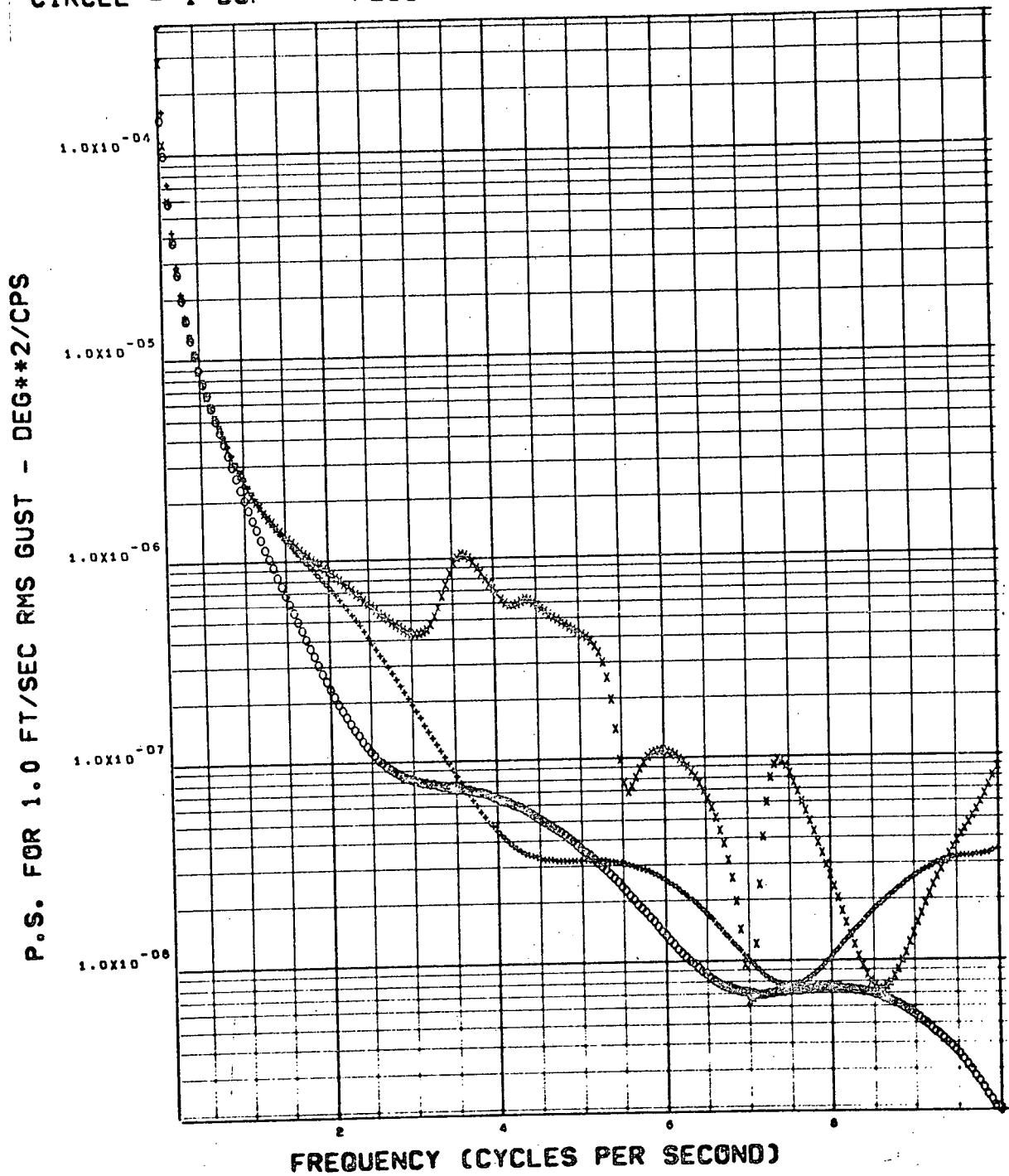


Figure 4-19. Booster Return Flight Fuselage Acceleration
 PSD (SAS Off, Symmetric) at LO₂ Tank

PT. 13 ACC. AT F.S. 3514 LH2 TANK - AFT BLK
 CIRCLE = 1 DOF PLUS = 2 DOF X = 10 DOF

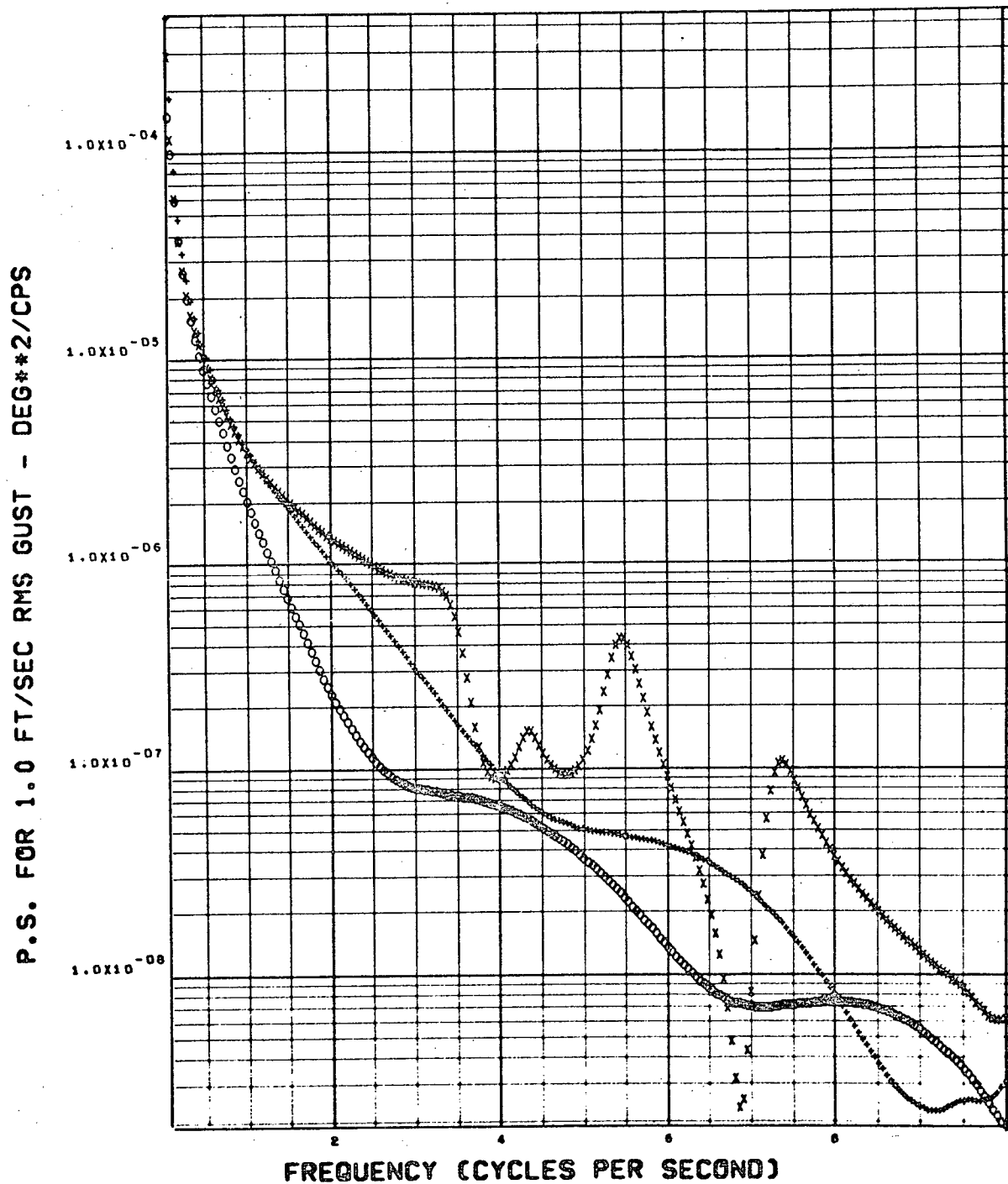


Figure 4-20. Booster Return Flight Fuselage Acceleration
 PSD (SAS Off, Symmetric) at LH₂ Tank

FUSELAGE SHEAR AT F.S. 2800
 CIRCLE = 1 DOF PLUS = 2 DOF X = 10 DOF

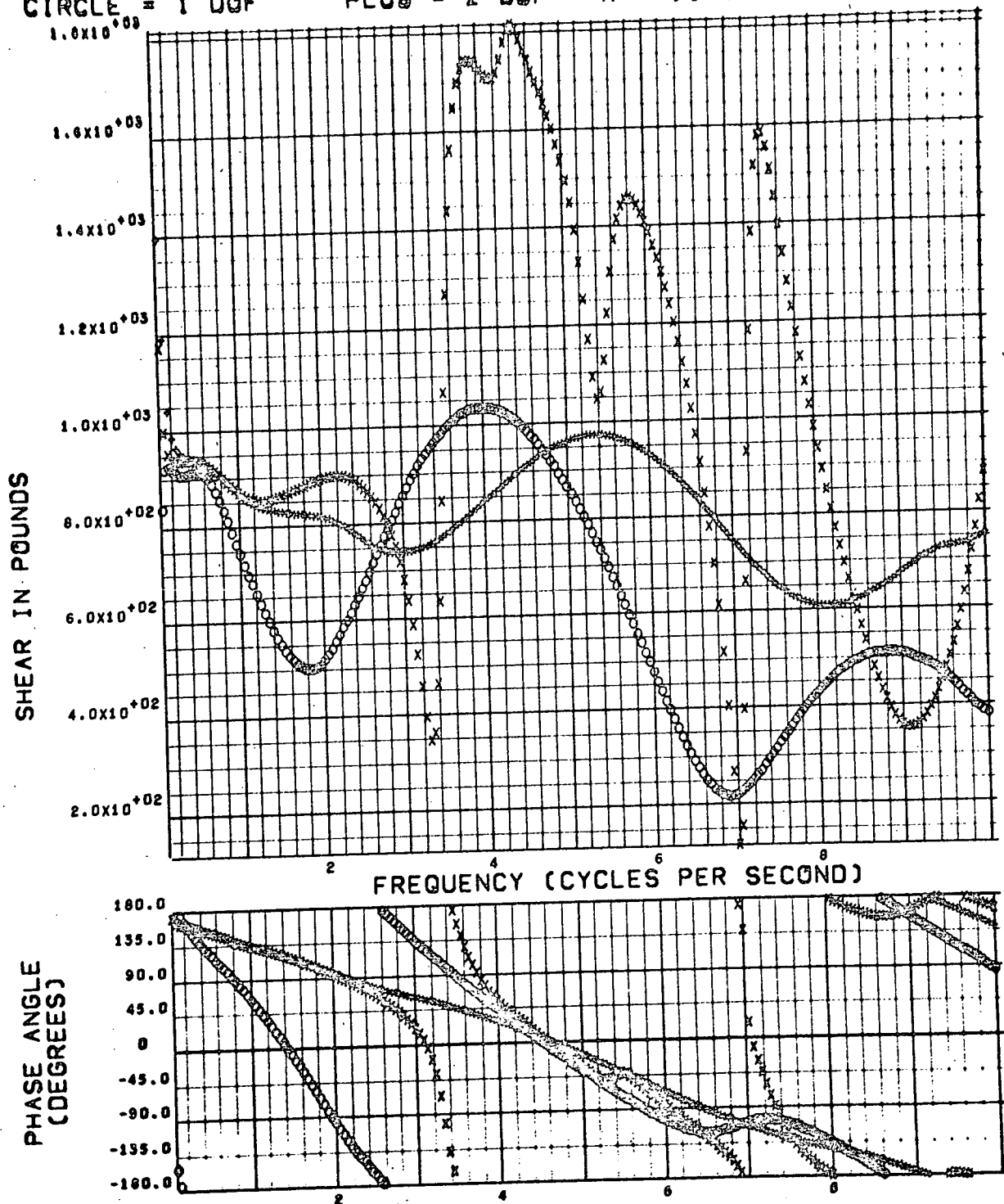


Figure 4-21. Booster Return Flight Fuselage Shear Transfer Function at FS 2800 (SAS Off, Symmetric)

FUSELAGE BENDING MOMENT AT F.S. 2000
 CIRCLE = 1 DOF PLUS = 2 DOF X = 10 DOF

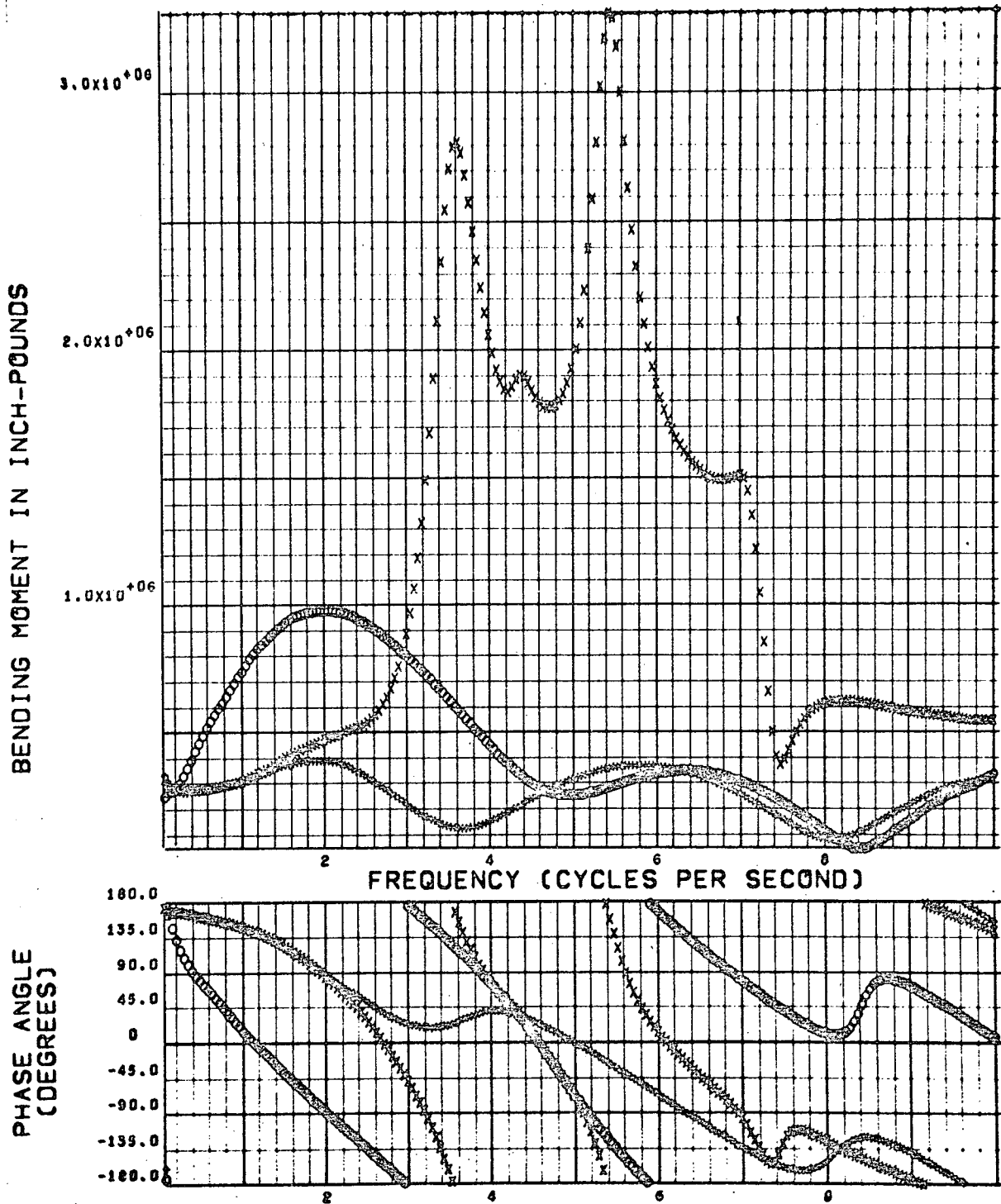


Figure 4-22. Booster Return Flight Fuselage Bending Moment Transfer Function at FS 2800 (SAS Off, Symmetric)

FUSELAGE SHEAR AT F.S. 2800
 CIRCLE = 1 DOF PLUS = 2 DOF X = 10 DOF

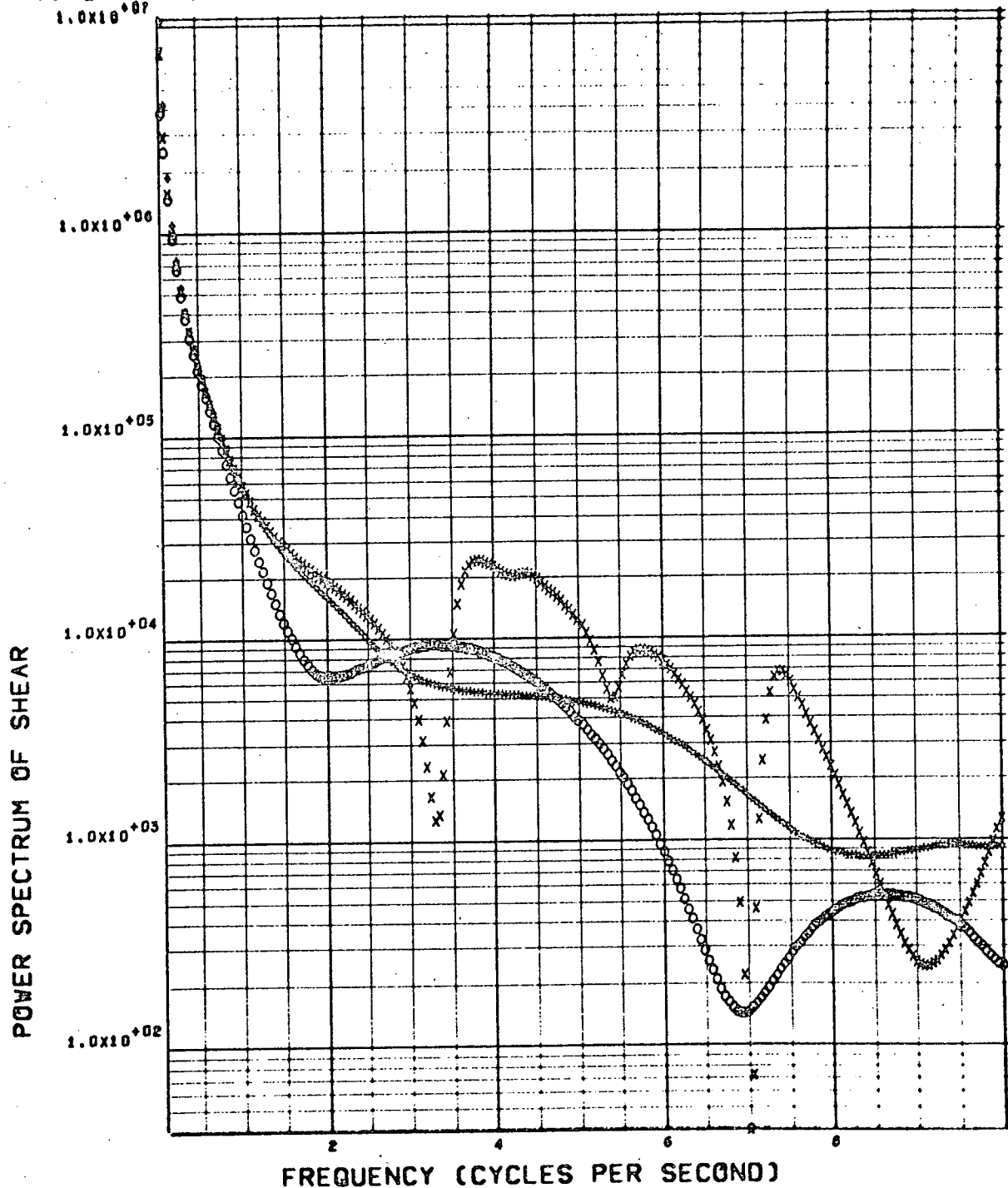


Figure 4-23. Booster Return Flight Fuselage Shear
 PSF at FS 2800 (SAS Off, Symmetric)

FUSELAGE BENDING MOMENT AT F.S. 2000
 CIRCLE = 1 DOF PLUS = 2 DOF X = 10 DOF

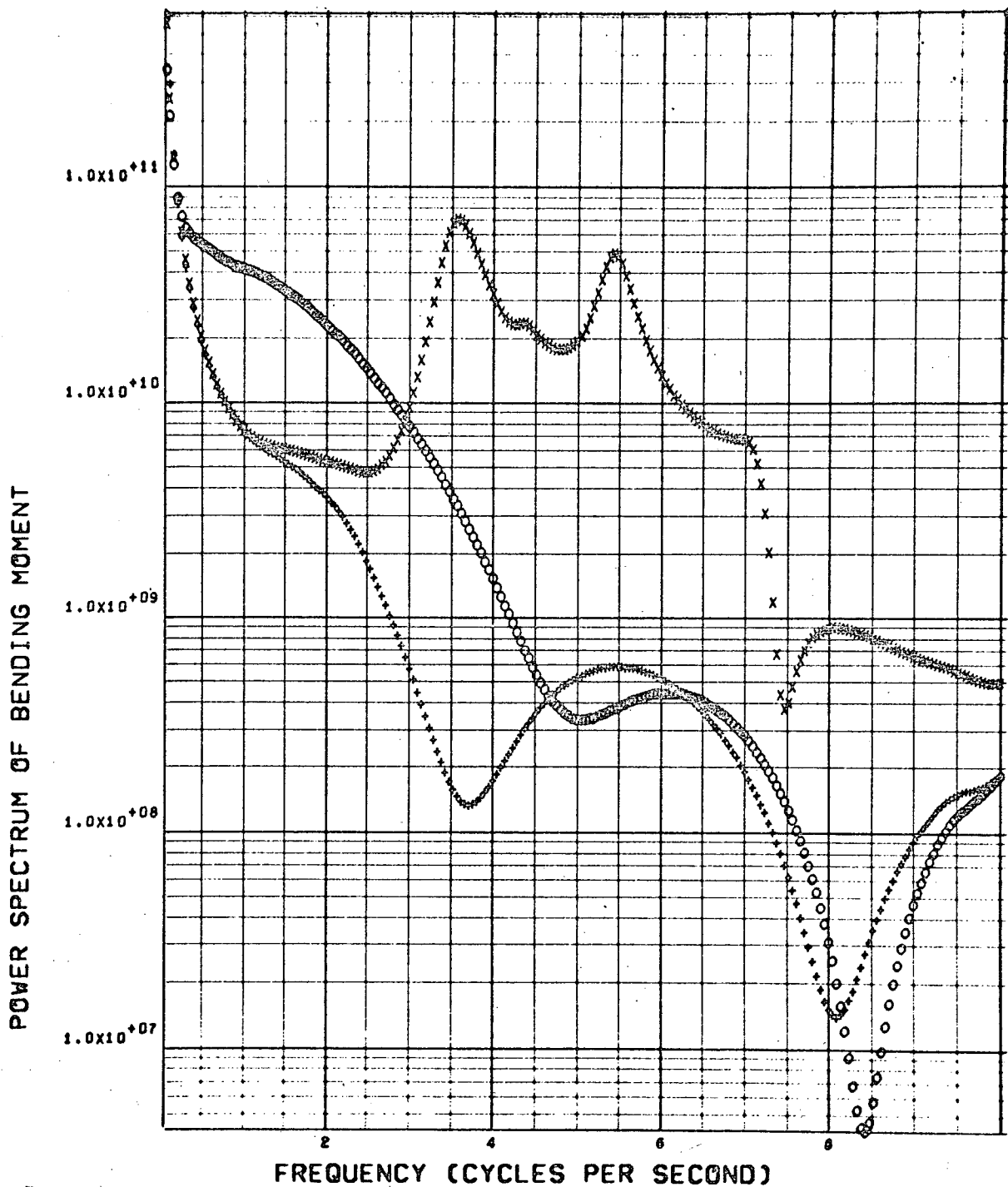


Figure 4-24. Booster Return Flight Fuselage Bending Moment
 PSD at FS 2800 (SAS Off, Symmetric)

WING SHEAR AT WING ROOT CHORD
 CIRCLE = 1 DOF PLUS = 2 DOF X = 10 DOF

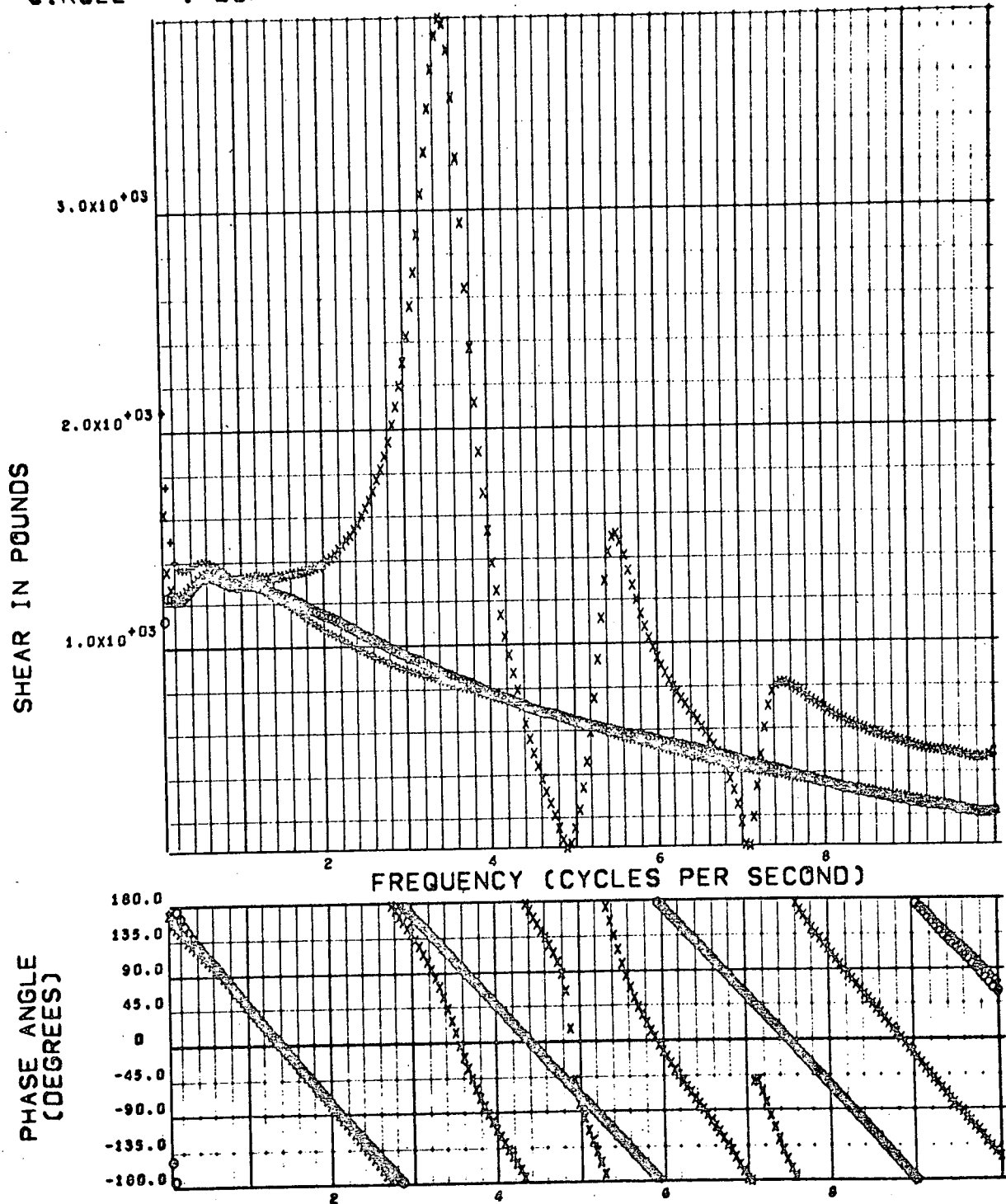


Figure 4-25. Booster Return Flight Wing Root Shear Transfer Function (SAS Off, Symmetric)

WING BENDING MOMENT AT WING ROOT CHORD
 CIRCLE = 1 DOF PLUS = 2 DOF X = 10 DOF

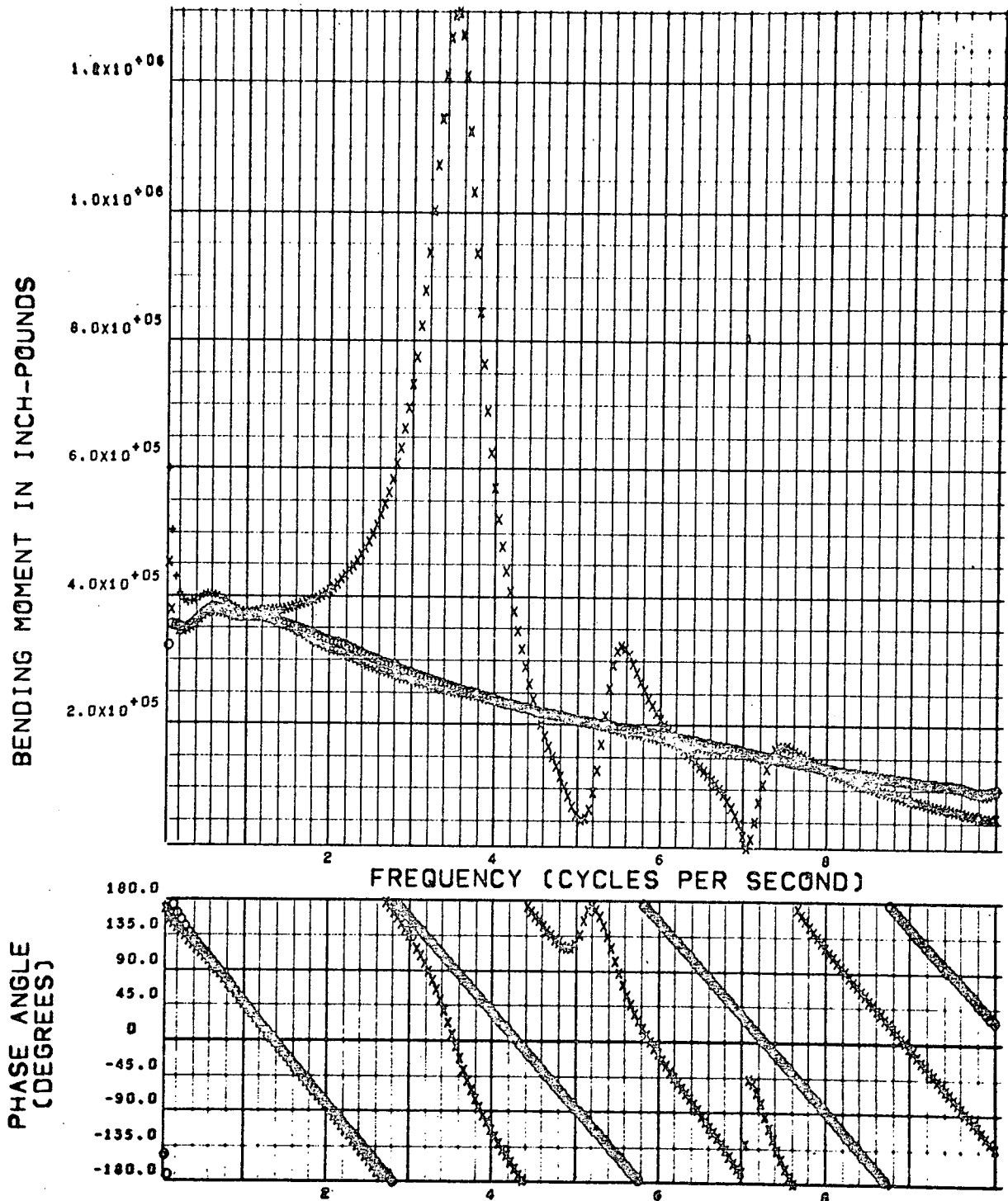


Figure 4-26. Booster Return Flight Wing Root Bending Moment Transfer Function (SAS Off, Symmetric)

WING TORQUE ABOUT F.S. 3488.5 WING ROOT
 CIRCLE = 1 DOF PLUS = 2 DOF X = 10 DOF

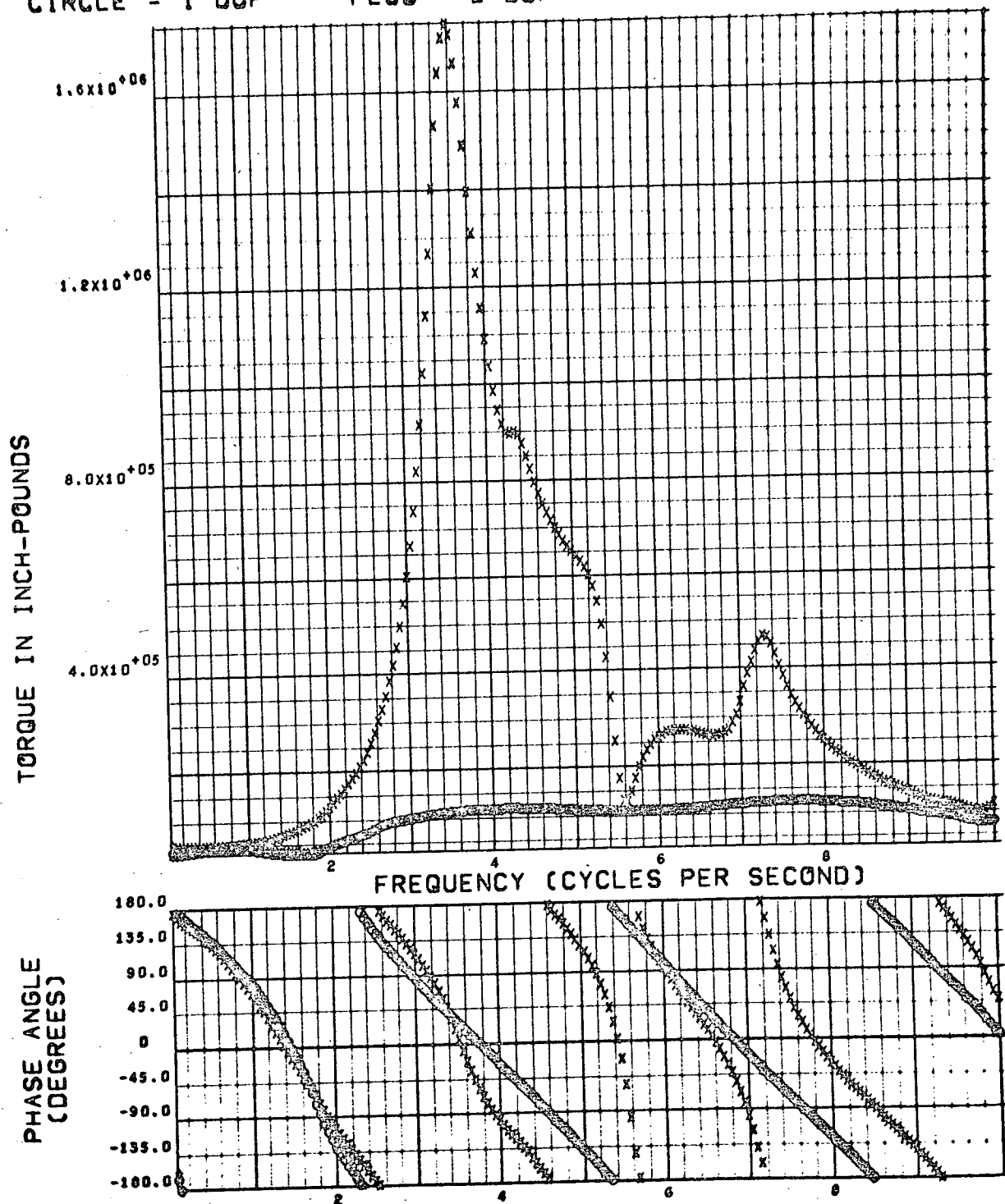


Figure 4-27. Booster Return Flight Wing Root Torque About FS 3488.5 Transfer Function (SAS Off, Symmetric)

WING SHEAR AT WING ROOT CHORD
 CIRCLE = 1 DOF PLUS = 2 DOF X = 10 DOF

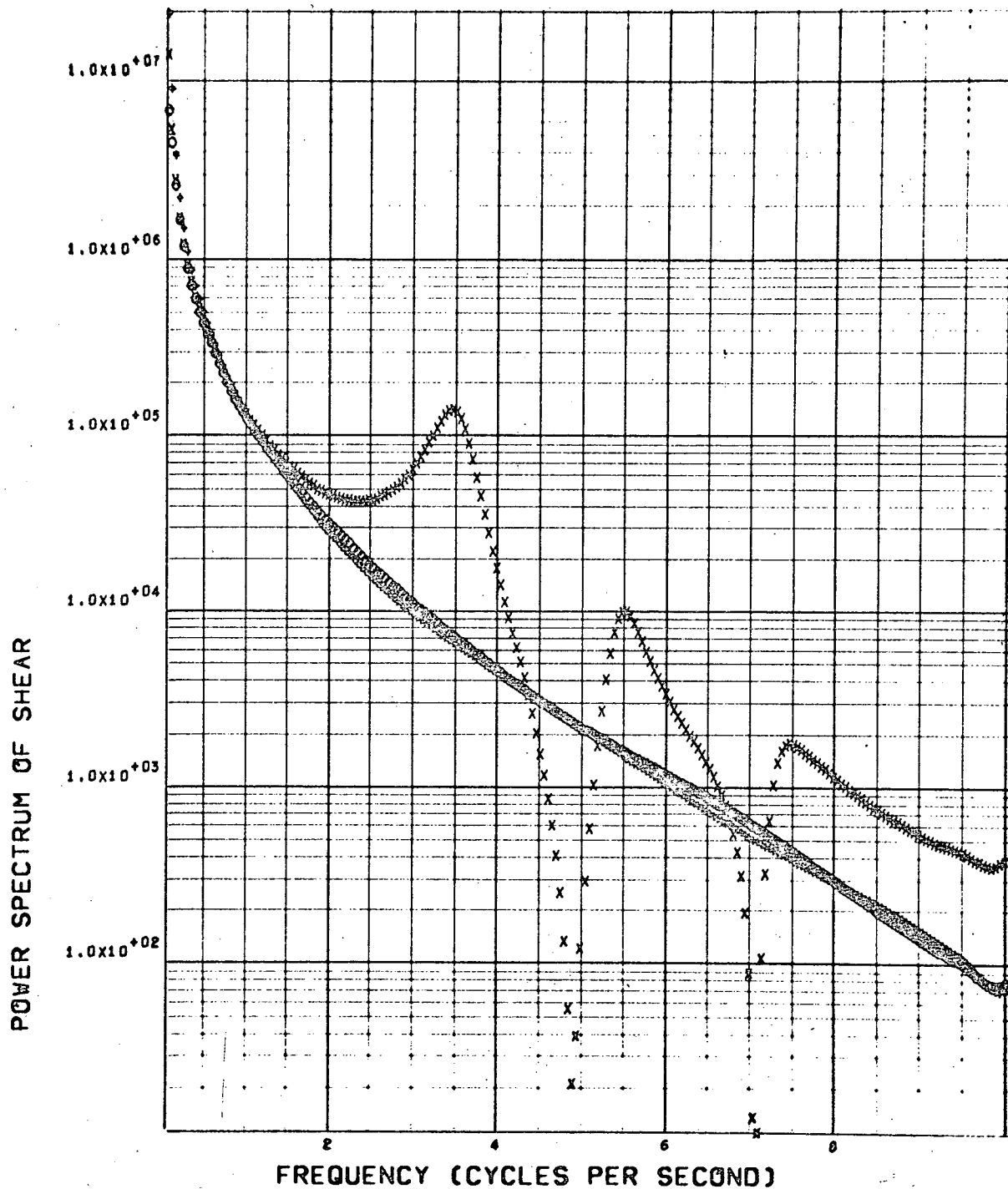


Figure 4-28. Booster Return Flight Wing Root Shear PSD (SAS Off, Symmetric)

WING BENDING MOMENT AT WING ROOT CHORD
 CIRCLE = 1 DOF PLUS = 2 DOF X = 10 DOF

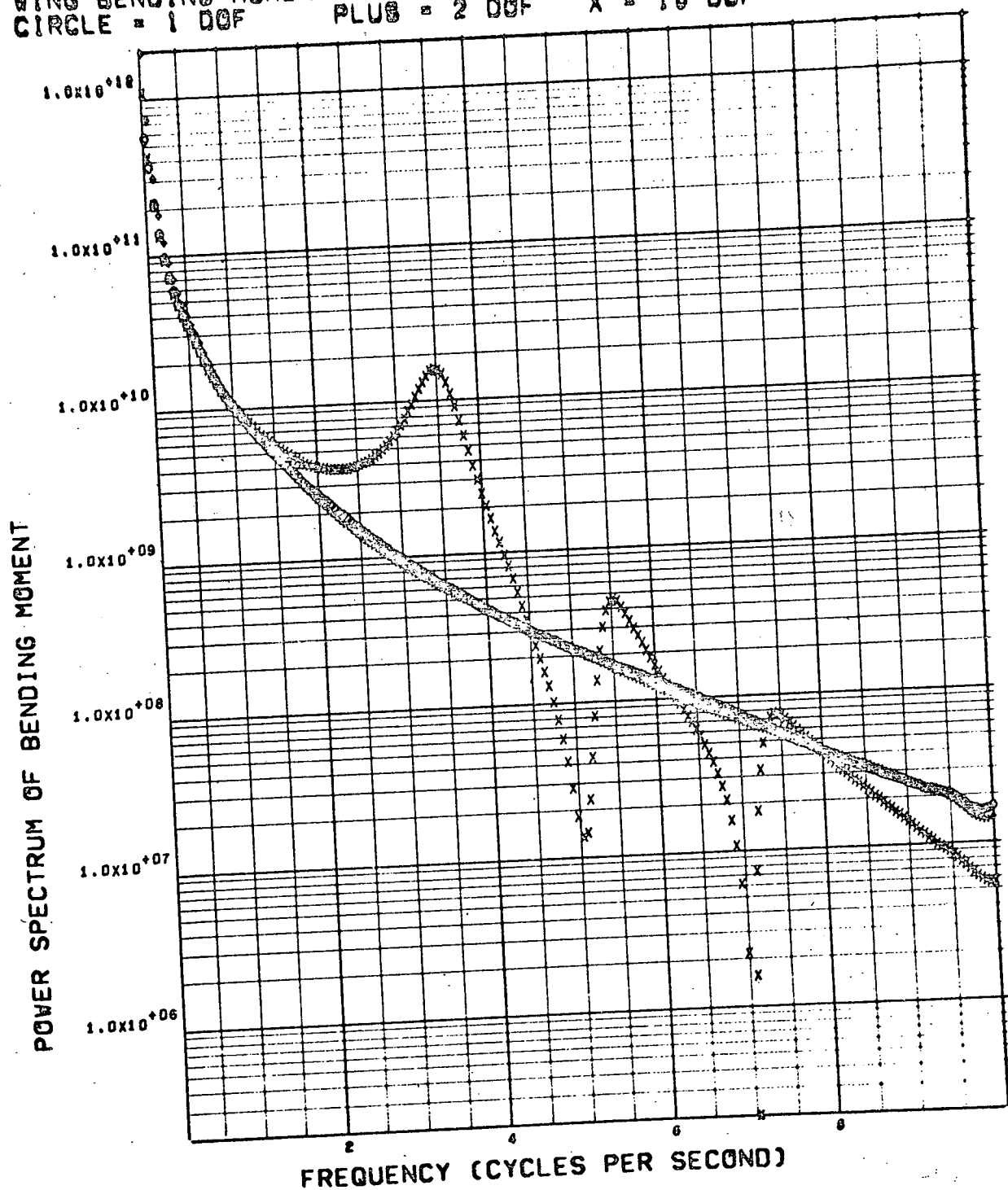


Figure 4-29. Booster Return Flight Wing Root Bending Moment PSD (SAS Off, Symmetric)

WING TORQUE ABOUT F.S. 3488.5 WING ROOT
 CIRCLE = 1 DOF PLUS = 2 DOF X = 10 DOF

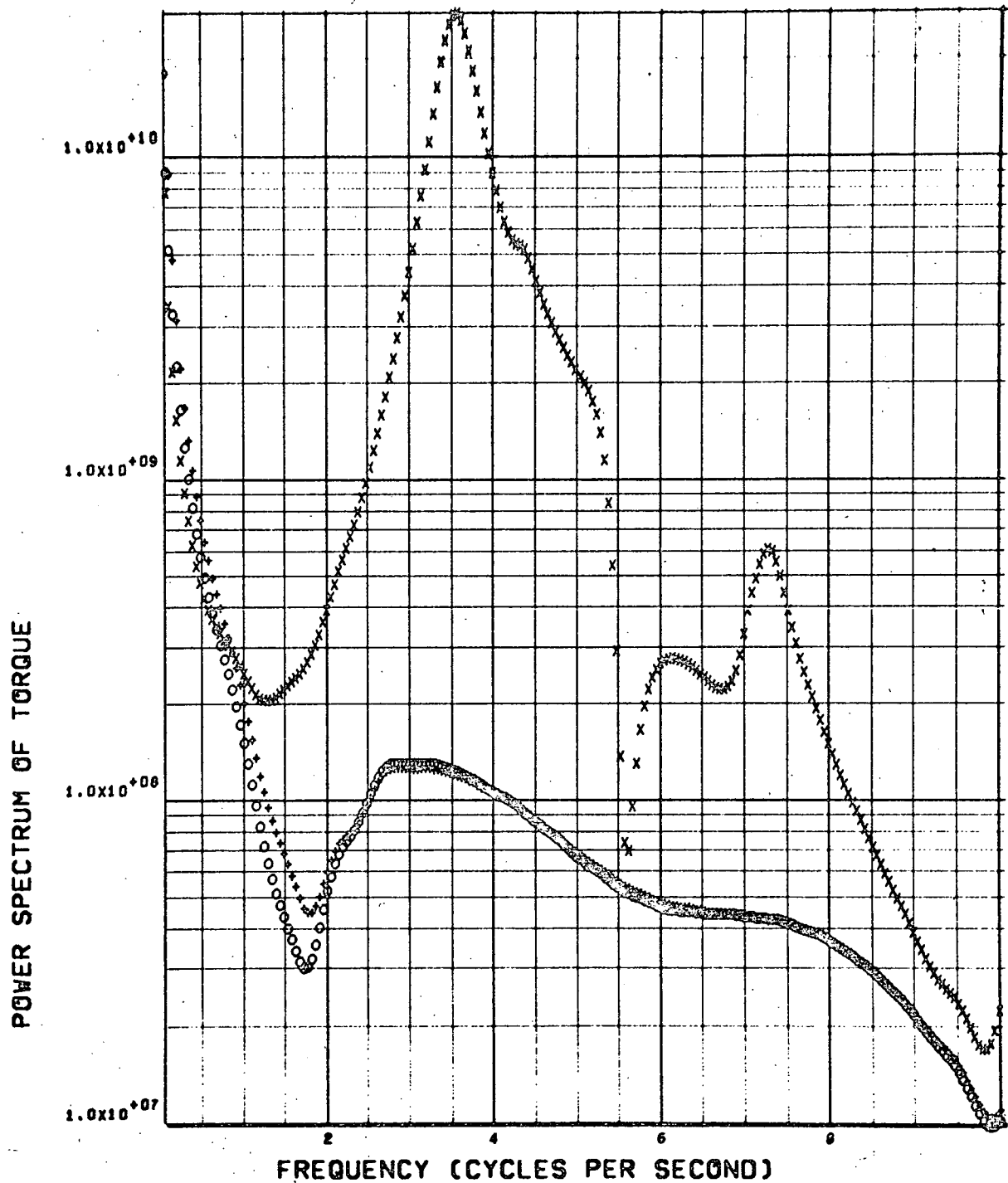


Figure 4-30. Booster Return Flight Wing Root Torque About FS 3488.5 PSD (SAS Off, Symmetric)

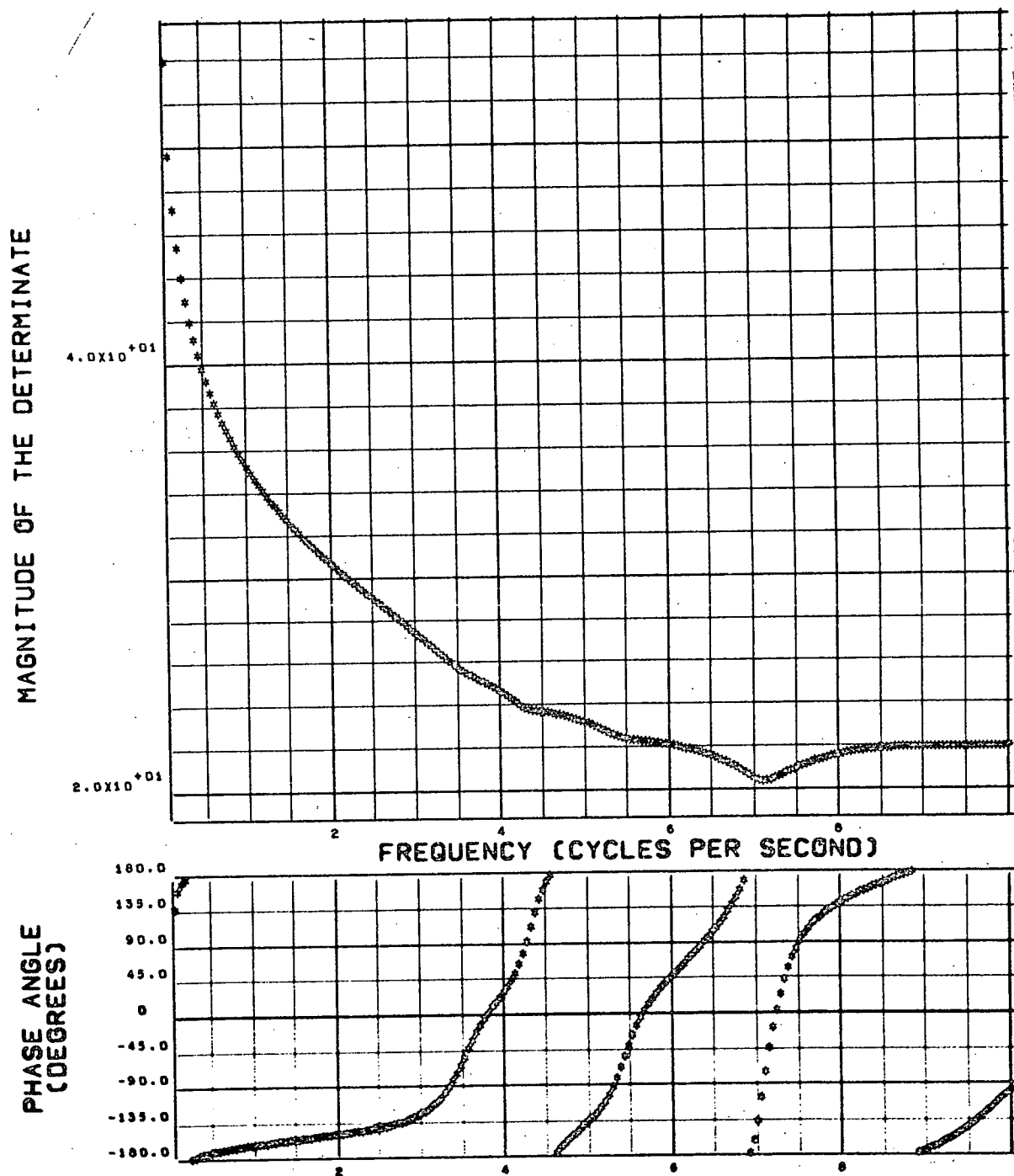


Figure 4-31. Booster Return Flight A-Matrix Determinant Magnitude and Phase Angle (SAS Off, Symmetric)

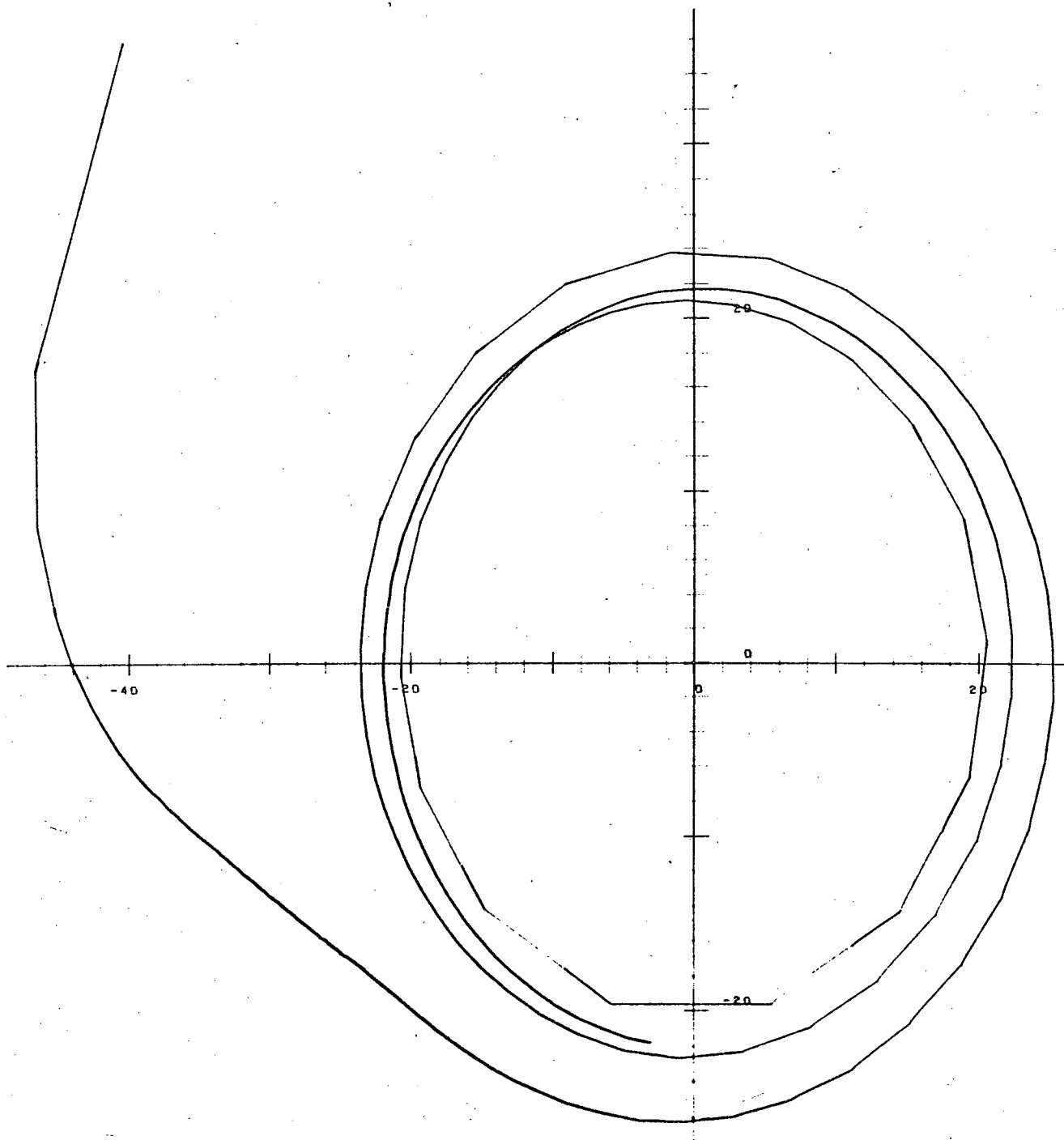


Figure 4-32. Booster Return Flight A-Matrix Determinant
Polar Plot (SAS Off, Symmetric)

PT. 2 ACC. AT F.S. 1150 CREW STATION
 CIRCLE = 1 DOF PLUS = 2 DOF X = 8 DOF

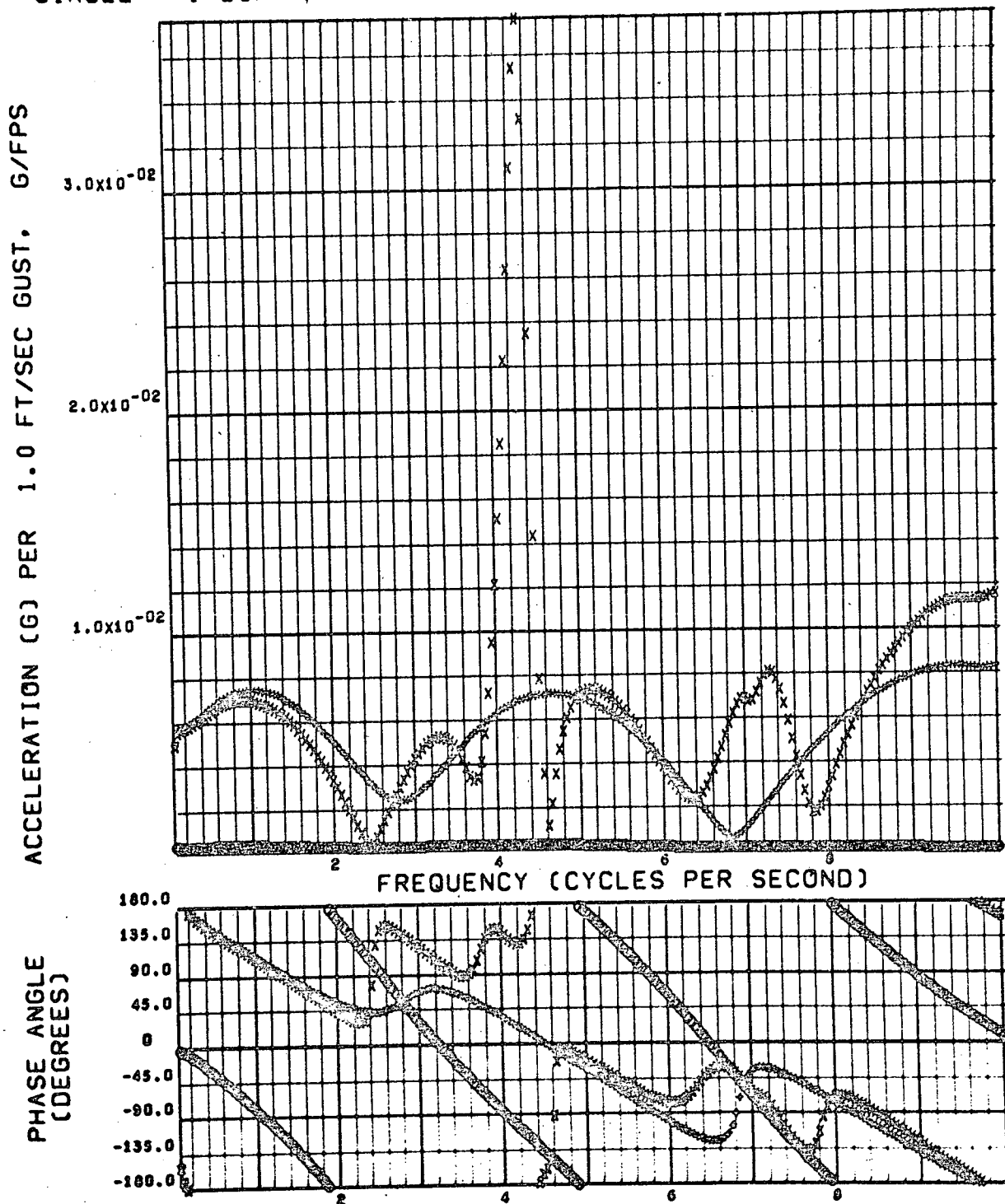


Figure 4-33. Booster Return Flight Fuselage Acceleration Transfer Function (SAS On, Symmetric) at Crew Station

PT. 5 ACC. AT F.S. 1814 LOX TANK - AFT BLK
 CIRCLE = 1 DOF PLUS = 2 DOF X = 8 DOF

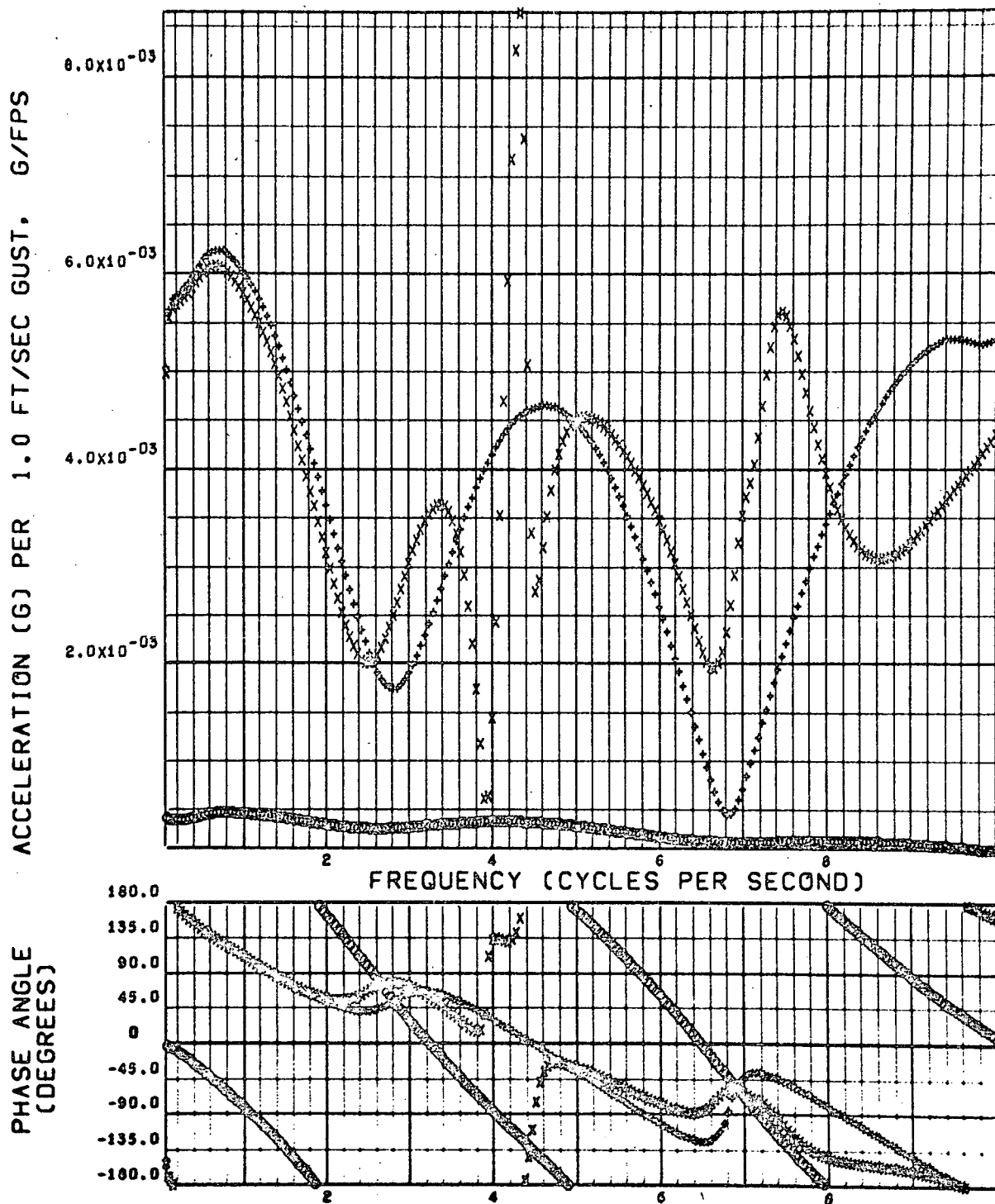


Figure 4-34. Booster Return Flight Fuselage Acceleration Transfer Function (SAS On, Symmetric) at LO₂ Tank

PT. 13 ACC. AT F.S. 3514 LH2 TANK - AFT BLK
 CIRCLE = 1 DOF PLUS = 2 DOF X = 8 DOF

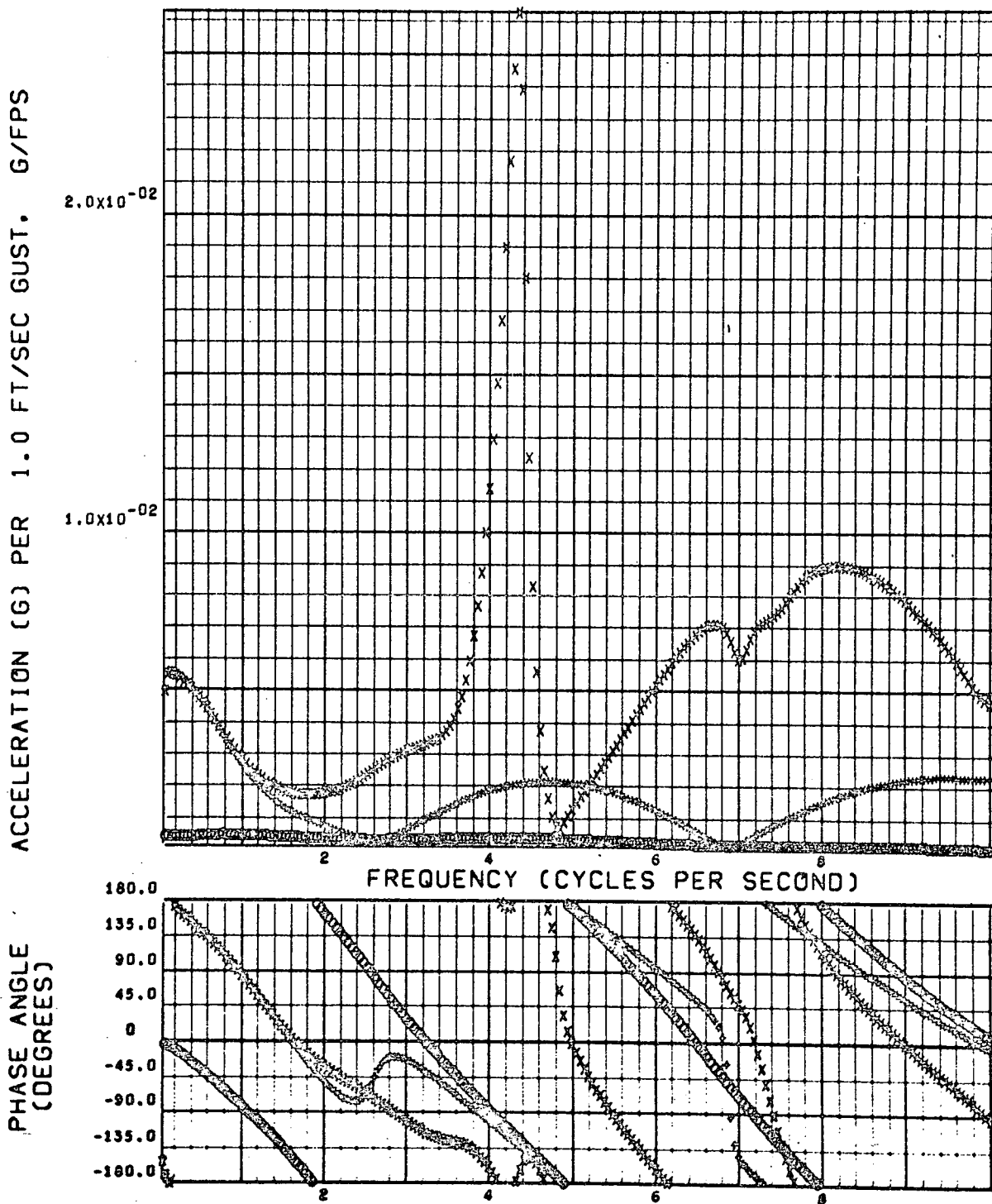


Figure 4-35. Booster Return Flight Fuselage Acceleration Transfer Function (SAS On, Symmetric) at LH₂ Tank

PT. 2 ACC. AT F.S. 1150 CREW STATION
 CIRCLE = 1 DOF PLUS = 2 DOF X = 8 DOF

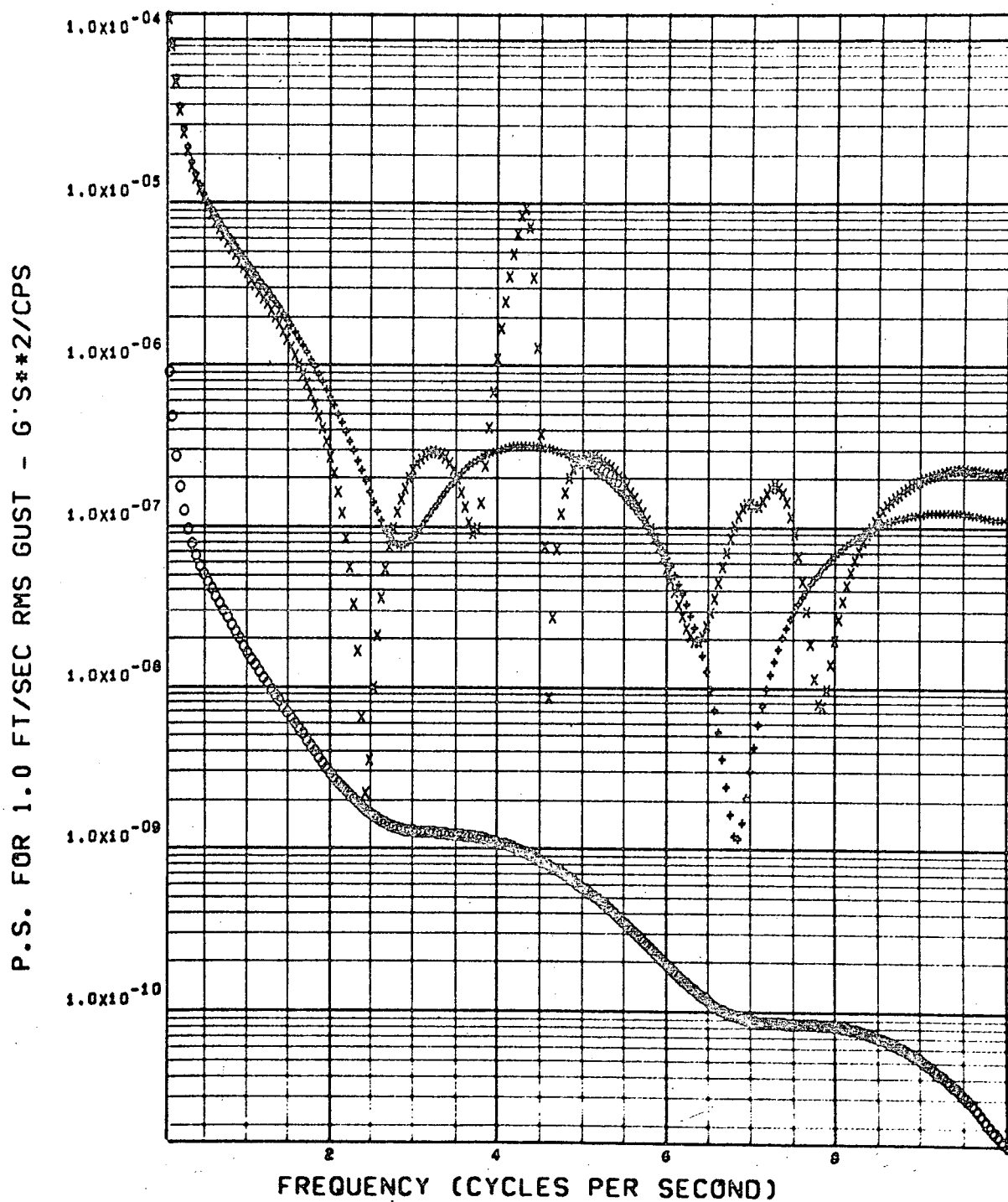


Figure 4-36. Booster Return Flight Fuselage Acceleration
 PSD (SAS On, Symmetric) at Crew Station

PT. 5 ACC. AT F.S. 1814 LOX TANK - AFT BLK
 CIRCLE = 1 DOF PLUS = 2 DOF X = 8 DOF

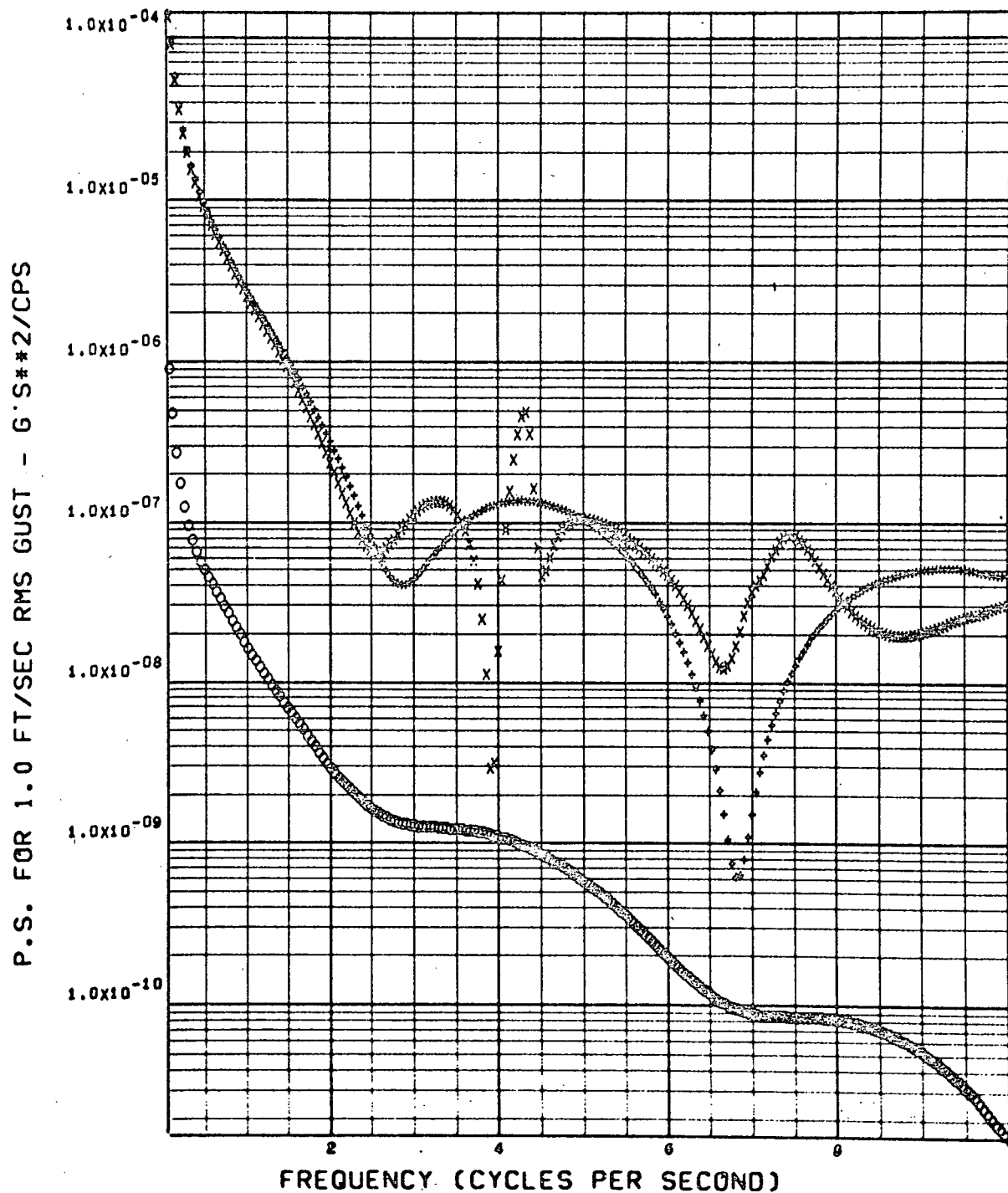


Figure 4-37. Booster Return Flight Fuselage Acceleration
 PSD (SAS On, Symmetric) at LO₂ Tank

PT. 13 ACC. AT F.S. 3514 LH2 TANK - AFT BLK
 CIRCLE = 1 DOF PLUS = 2 DOF X = 8 DOF

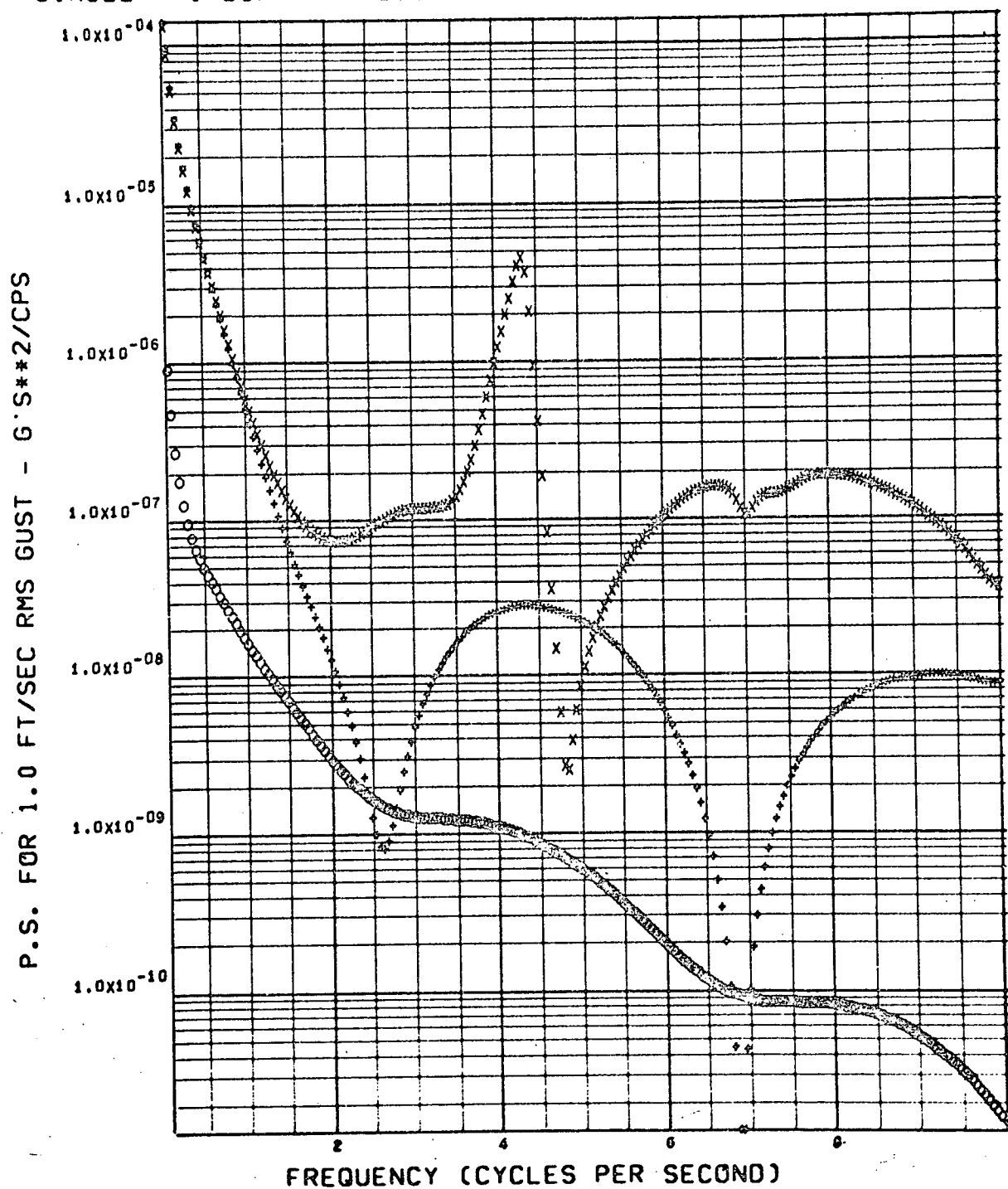


Figure 4-38. Booster Return Flight Fuselage Acceleration
 PSD (SAS On, Symmetric) at LH₂ Tank

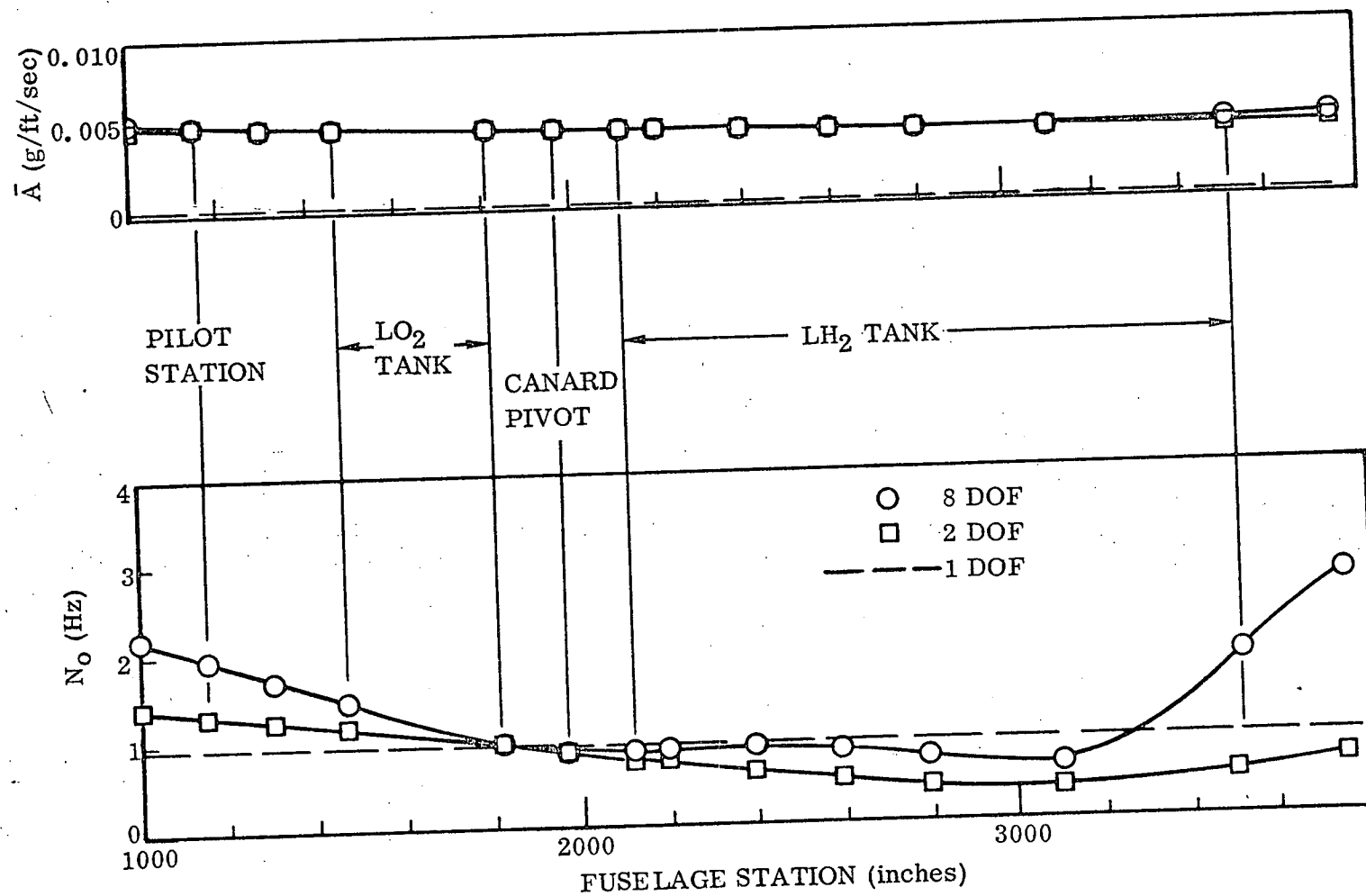


Figure 4-39. Booster Return Flight Fuselage Acceleration \bar{A} and N_0 (SAS On, Symmetric)

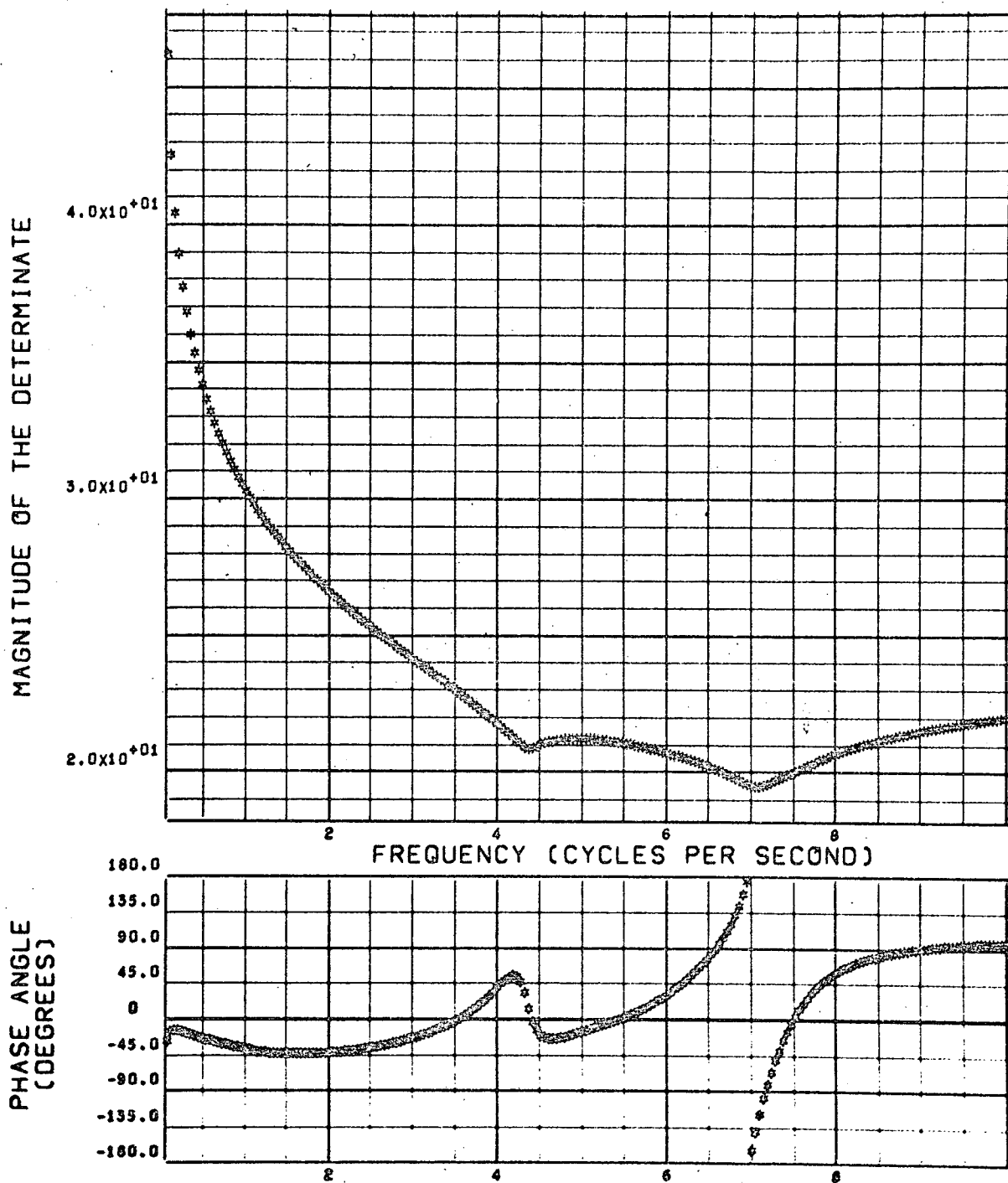


Figure 4-40. Booster Return Flight A-Matrix Determinant Magnitude and Phase Angle (SAS On, Symmetric)

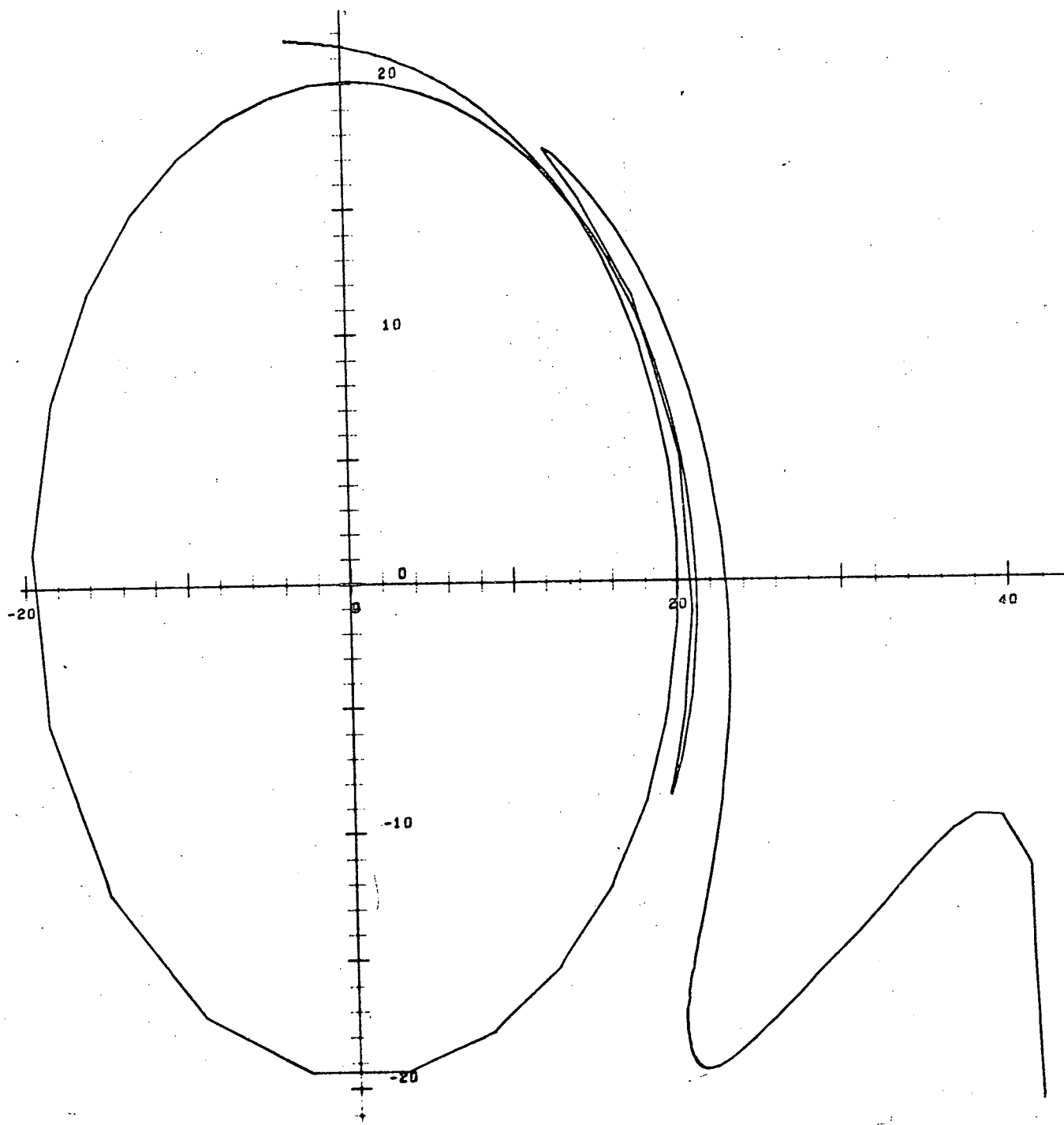


Figure 4-41. Booster Return Flight A-Matrix Determinant
Polar Plot (SAS On, Symmetric)

4.2 ASCENT FLIGHT

Referring to Figure 4-42, the rigid body symmetric equations of motion are:

Sum of forces in z-direction:

$$\sum F_z = -C_{L\alpha} \alpha QS + T \delta_{\text{pitch}} \quad (4-4)$$

Sum of moments about y-axis:

$$\sum M_y = C_{L\alpha} \alpha QS (\bar{x}_{cg} - \bar{x}_{AC}) + T \delta_{\text{pitch}} (\bar{x}_G - \bar{x}_{cg}) \quad (4-5)$$

Pitching acceleration (about y-axis):

$$\dot{q} = \sum M_y / I_{yy} \quad (4-6)$$

Acceleration in z-direction:

$$\dot{w} = \sum F_z / M + qu \quad (4-7)$$

In keeping with standard aircraft notation, u , v , and w are the velocity components in the x , y , and z directions respectively and p , q , and r are the three angular velocity components.

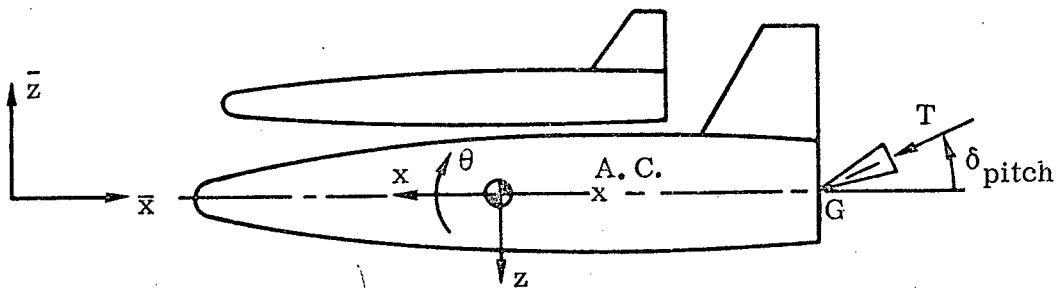


Figure 4-42. Ascent Symmetric Flight Sign Convention

The pitch plane SAS block diagram is shown in Figure 4-43.

The rigid body equations of motion for transient antisymmetric flight using the sign conventions in Figure 4-44 are:

Sum of forces in y-direction:

$$\sum F_y = C_{y\beta} \beta QS - T \delta_{\text{yaw}} \quad (4-8)$$

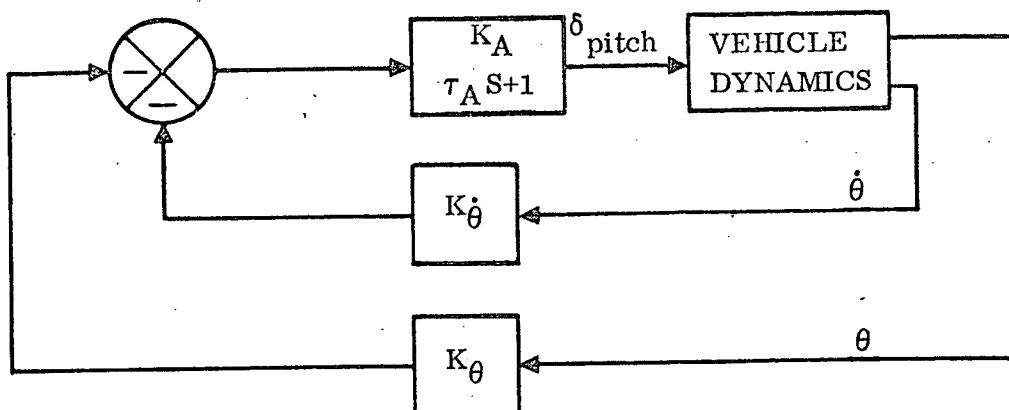


Figure 4-43. Ascent Symmetric Flight SAS Block Diagram

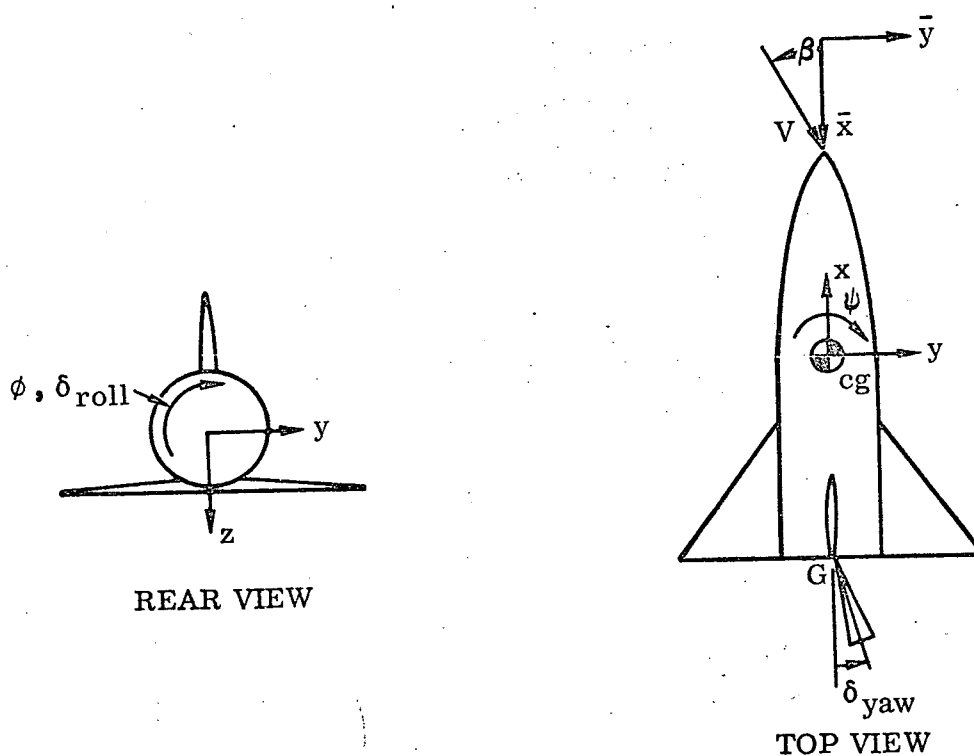


Figure 4-44. Ascent Antisymmetric Flight Sign Convention

Sum of moments about x-axis:

$$\Sigma M_x = \left[(C_{l\beta} B_{ref} + C_{y\beta} Z_1) \beta + C_{l\delta_a} \delta_a \right] Q S + l_{roll} T \delta_{roll} \quad (4-9)$$

Sum of moments about z-axis:

$$\Sigma M_z = (C_{n\beta} B_{ref} + C_{y\beta} X_1) \beta Q S + T \delta_{yaw} (\bar{x}_G - \bar{x}_{cg}) \quad (4-10)$$

Rolling acceleration (about x-axis):

$$\dot{p} = \left(\sum M_x + I_{xz} \dot{r} \right) / I_{xx} \quad (4-11)$$

Yawing acceleration (about z-axis):

$$\dot{r} = \left(\sum M_z + I_{xz} \dot{p} \right) / I_{zz} \quad (4-12)$$

Acceleration in y-direction:

$$\dot{v} = \sum F_y / M - ru \quad (4-13)$$

In Equation 4-9, δ_a is the aileron deflection defined such that a positive value causes positive roll.

The SAS block diagram for ascent antisymmetric flight is shown in Figure 4-45.

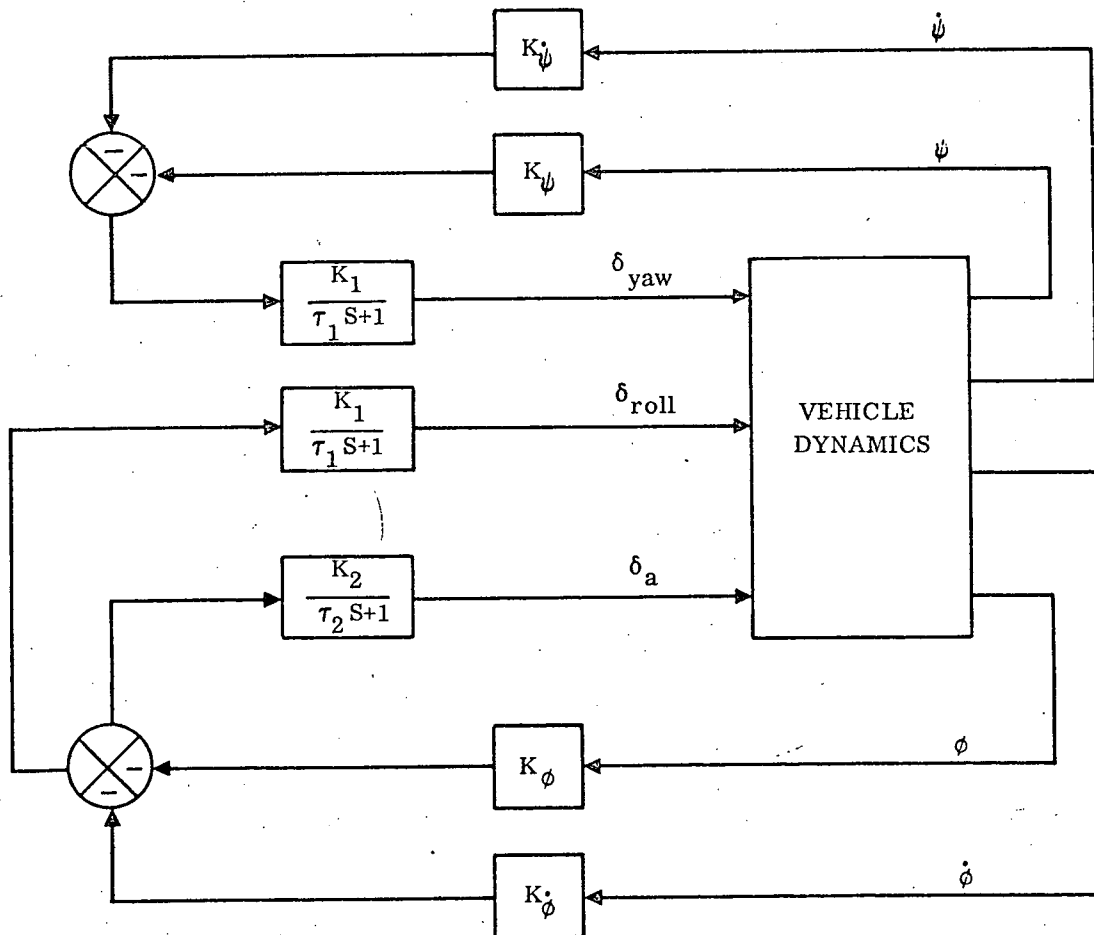


Figure 4-45. Ascent Antisymmetric Flight SAS Block Diagram

Engine thrust and inertia force equations are derived in Section 2.4 for bending modes. The generalized forces produced by engine roll torques are given by:

$$Q_i = l_{\text{roll}} \phi_{x_i}' (m l \delta_{\text{roll}} - T \delta_{\text{roll}})$$

where l_{roll} is the effective roll thrust moment arm and ϕ_{x_i}' is the slope about the \bar{x} axis at the gimbal point due to mode i .

The propellant sloshing analysis results for 59 seconds flight time are summarized in Table 4-3.

Table 4-3. Sloshing Parameters

Tank	Slosh Mass (lb-sec ² /in.)	Slosh Spring (lb/in.)	Slosh cg (Booster Station) (in.)
LH ₂	63.7	373	2863
LO ₂	1030	6020	1622

Basic data for the symmetric and antisymmetric ascent analyses are listed in Tables 4-4 and 4-5, respectively.

Table 4-4. Basic Data - Symmetric Ascent Flight

$t = 59 \text{ sec}$	$T = 6.3 \times 10^6 \text{ lb}$
Mach number = 0.9	$Q = 486 \text{ lb/ft}^2$
Altitude = 40,000 ft	$S = 7797 \text{ ft}^2$
$M = 1.112 \times 10^5 \text{ slugs}$	$C_{L\alpha} = 3.84 \text{ per radian}$
$I_{yy} = 411 \times 10^6 \text{ slug-ft}^2$	$K_A = 1 \text{ rad/rad}$
$\bar{x}_{cg} = 183.1 \text{ ft}$	$\tau_A = 0.0667 \text{ sec}$
$\bar{x}_{AC} = 213.9 \text{ ft}$	$K_{\dot{\theta}} = 1.0 \text{ rad/rad/sec}$
$\bar{x}_G = 312.5 \text{ ft}$	$K_{\theta} = 1.4 \text{ rad/rad}$

For each of the 12 gimballed engines, the mass properties are:

Mass = 165 slugs

Mass moment of inertia about gimbal point = 2505 slug-ft²

Center of gravity distance aft of gimbal point = 20.5 inches

Table 4-5. Basic Data - Antisymmetric Ascent Flight

$t = 59 \text{ sec}$	$C_{\ell\beta} = -0.424 \text{ per radian}$
Mach number = 0.9	$C_{\ell\delta_a} = 0.0658 \text{ per radian}$
Altitude = 40,000 ft	$C_{n\beta} = 1.32 \text{ per radian}$
$M = 1.112 \times 10^5 \text{ slugs}$	$B_{\text{ref}} = 145 \text{ ft}$
$I_{xx} = 32.9 \times 10^6 \text{ slug-ft}^2$	$Z_1 = -6.34 \text{ ft}$
$I_{zz} = 382 \times 10^6 \text{ slug-ft}^2$	$X_1 = 99.7 \text{ ft}$
$I_{xz} = -13.7 \times 10^6 \text{ slug-ft}^2$	$K_1 = 1 \text{ rad/rad}$
$\bar{x}_{cg} = 183.1 \text{ ft}$	$\tau_1 = 0.0667 \text{ sec}$
$\bar{x}_G = 312.5 \text{ ft}$	$K_2 = 3.0 \text{ rad/rad}$
$T = 6.3 \times 10^6 \text{ lb}$	$\tau_2 = 0.0667 \text{ sec}$
$Q = 486 \text{ lb/ft}^2$	$K_\phi = 1.0 \text{ rad/rad}$
$S = 7797 \text{ ft}^2$	$K_{\dot{\phi}} = 0.7 \text{ rad/rad/sec}$
$\ell_{\text{roll}} = 15 \text{ ft}$	$K_\psi = 1.4 \text{ rad/rad}$
$C_{y\beta} = -2.40 \text{ per radian}$	$K_{\dot{\psi}} = 1.0 \text{ rad/rad/sec}$

The booster structural idealization for the modal analysis was the same as that for the booster return flight symmetric analysis, with the addition of the vertical tail for the antisymmetric analysis. Tail idealization is shown in Figure 4-46, where the solid circles represent locations of masses.

The rigid orbiter was attached to the booster by springs located at Stations 1829 and 2657, as indicated in Figure 4-47. It was assumed that all axial load is transmitted at the forward attachment point, as is all yawing moment.

The first six symmetric modes for ascent flight at 59 seconds are shown in Figures 4-48 through 4-53. The orbiter center line is depicted by the line parallel to and above the booster fuselage center line. The first mode is body first bending; the second is wing first bending. The orbiter pitch mode is the fourth symmetric mode.

Figures 4-54 through 4-60 show the first seven antisymmetric modes. The fundamental mode is orbiter yaw, and the second and third are first body bending and first wing bending, respectively. The fourth mode is tail first bending.

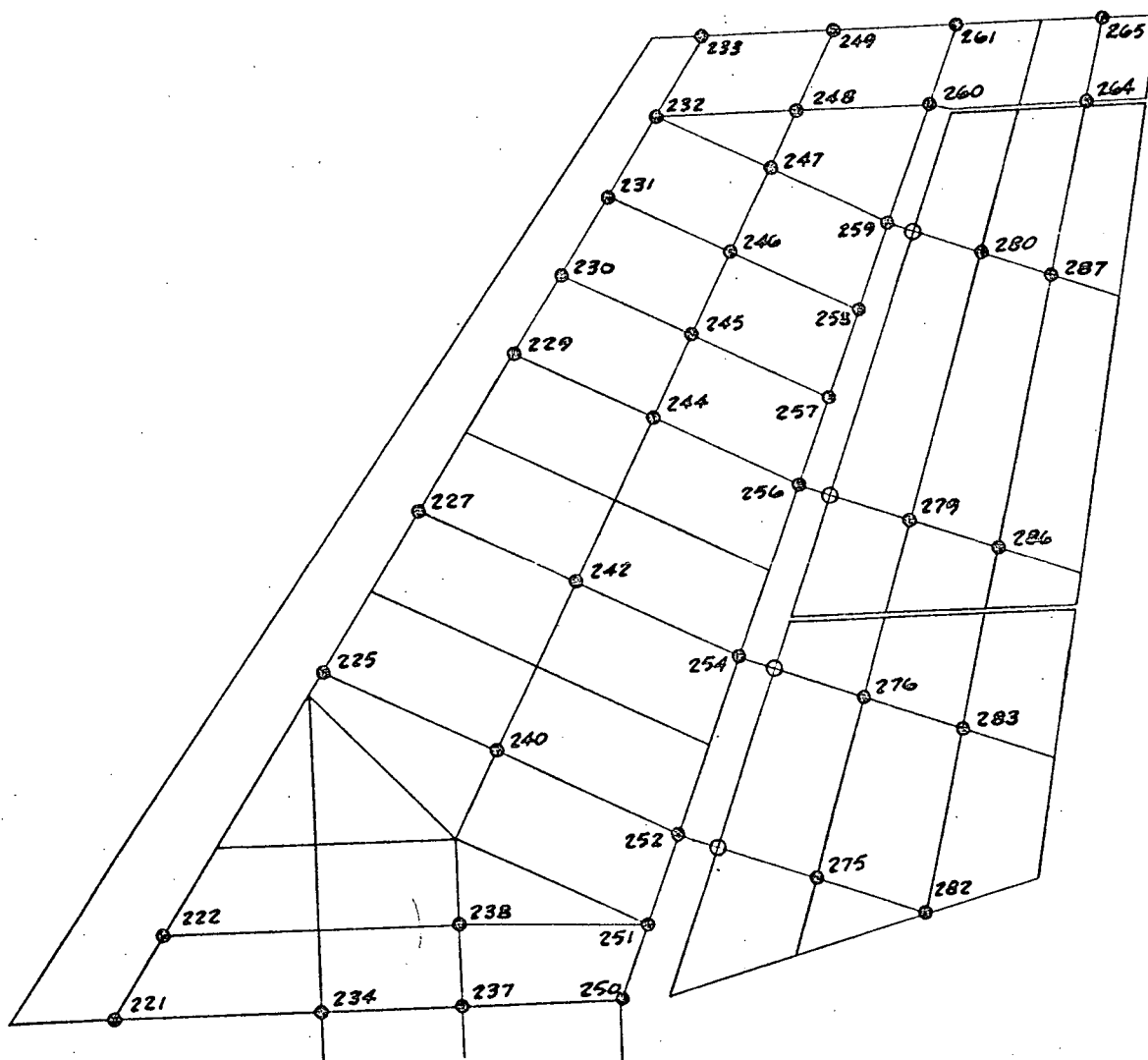
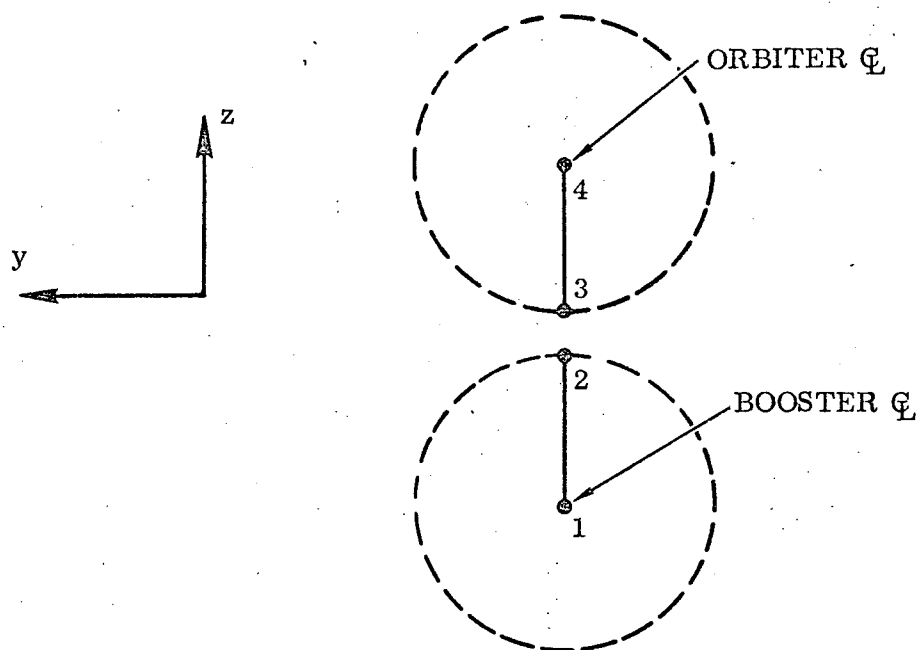


Figure 4-46. Booster Vertical Stabilizer Structural Idealization



TYPICAL CROSS-SECTION LOOKING AFT

The following stiffnesses relate Point 2 to Point 3.

	FWD (STATION 1829)	AFT (STATION 2657)
K_x	2.06×10^6	0 lb/in.
K_y	0.223×10^6	0.274×10^6 lb/in.
K_z	2.65×10^6	1.06×10^6 lb/in.
K_{θ_x}	5.97×10^6	2.56×10^{10} in.-lb/rad
K_{θ_y}	0	0 in.-lb/rad
K_{θ_z}	4.50×10^{10}	0 in.-lb/rad

Note: Links 1-2 and 3-4 are assumed rigid

Figure 4-47. Booster/Orbiter Attachment Stiffnesses

Frequency = 2.66 Hz

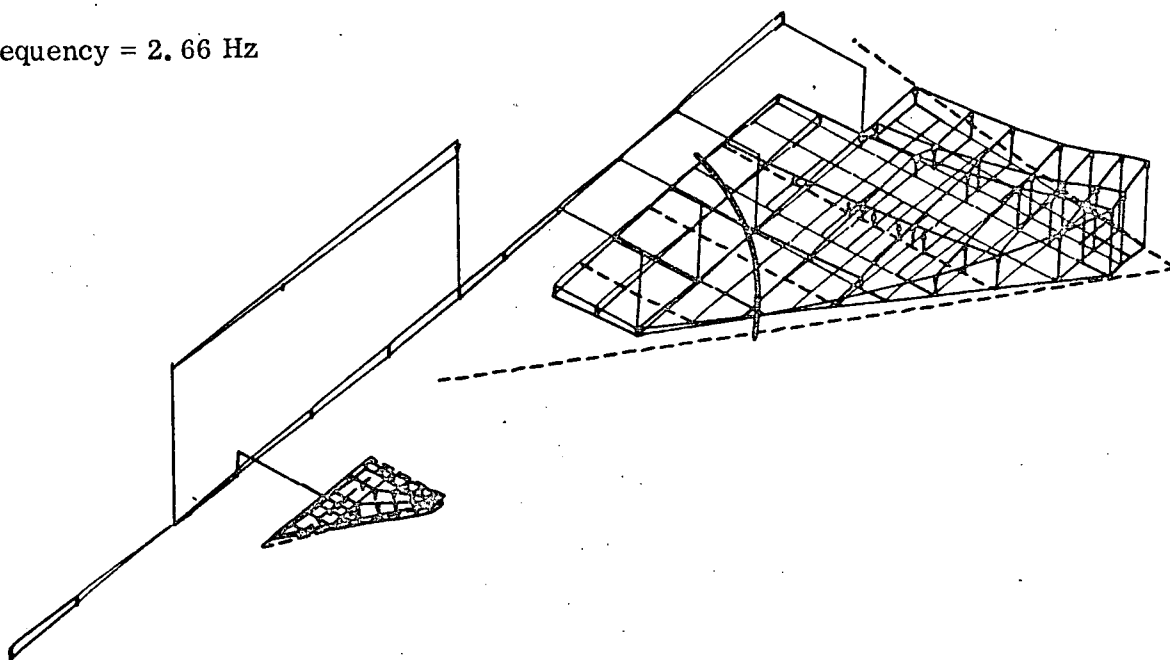


Figure 4-48. Ascent Flight First Symmetric Mode

Frequency = 3.26 Hz

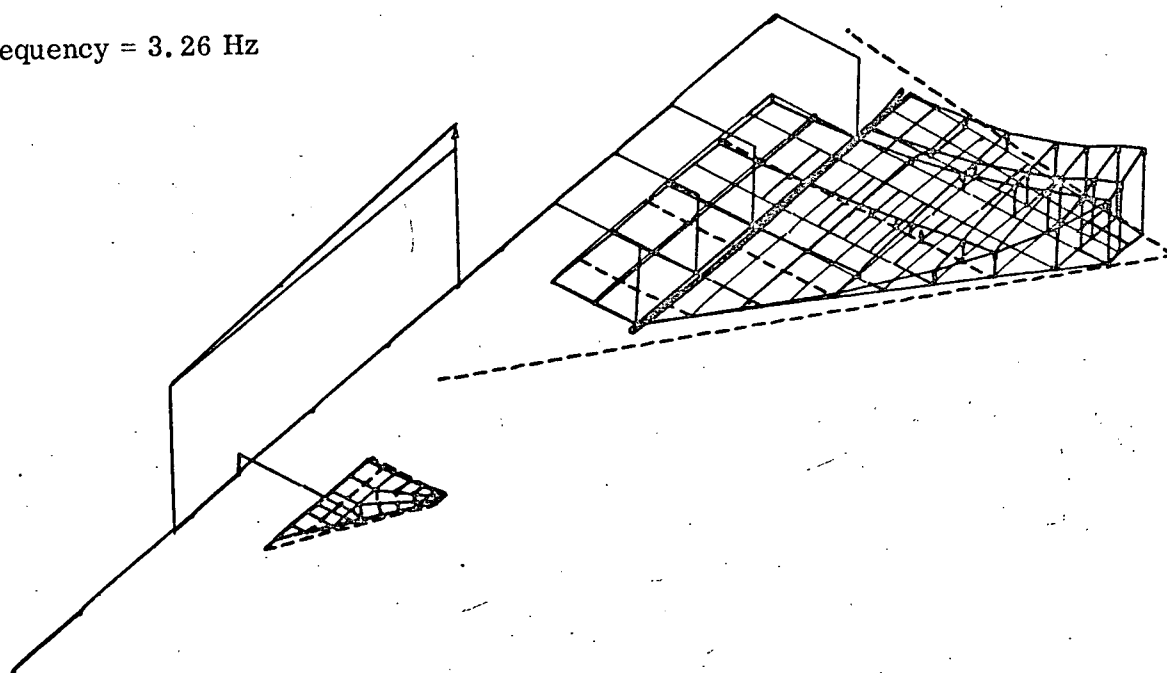


Figure 4-49. Ascent Flight Second Symmetric Mode

Frequency = 4.42 Hz

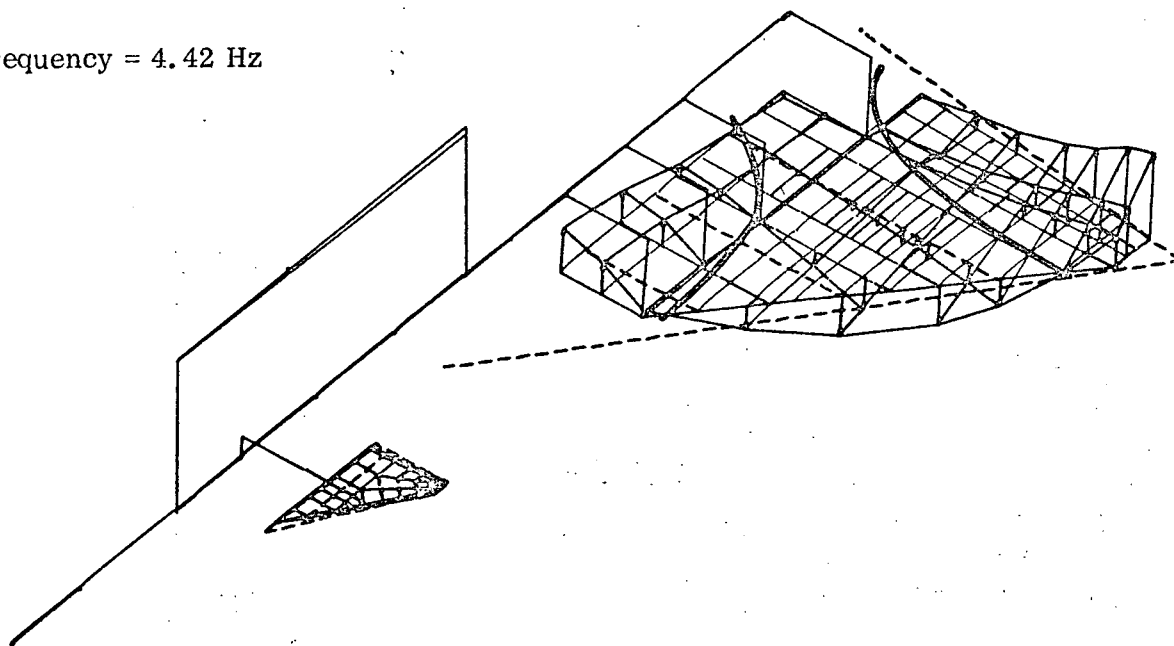


Figure 4-50. Ascent Flight Third Symmetric Mode

Frequency = 5.07 Hz

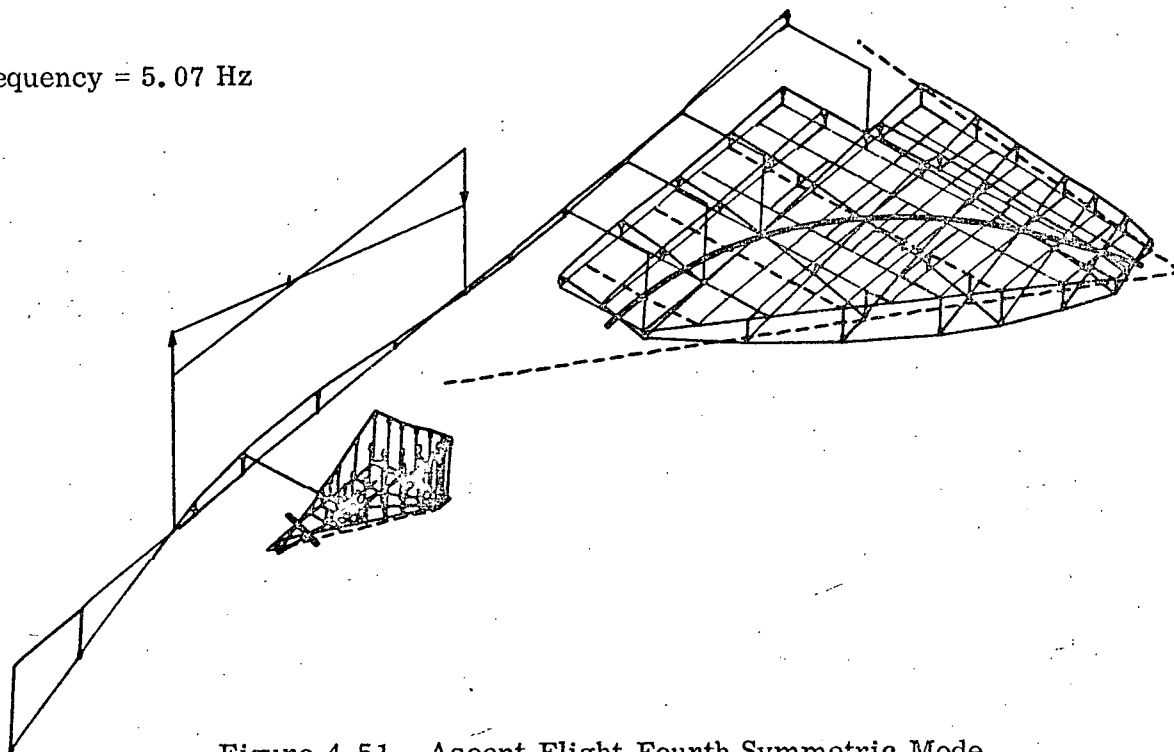


Figure 4-51. Ascent Flight Fourth Symmetric Mode

Frequency = 6.18 Hz

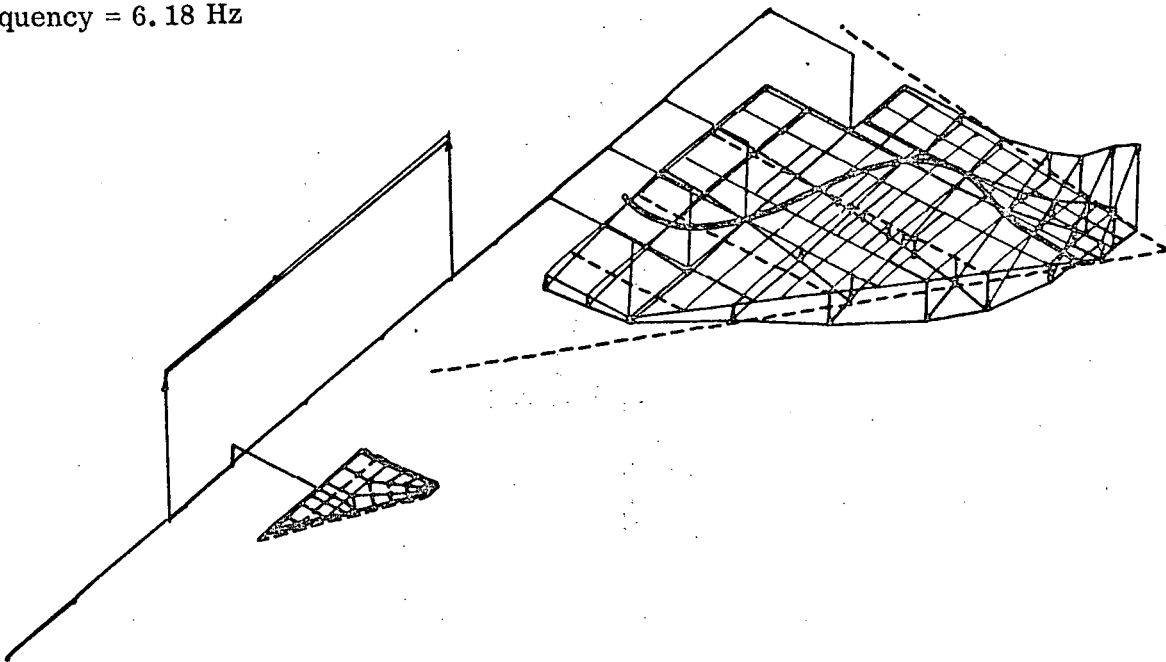


Figure 4-52. Ascent Flight Fifth Symmetric Mode

Frequency = 6.29 Hz

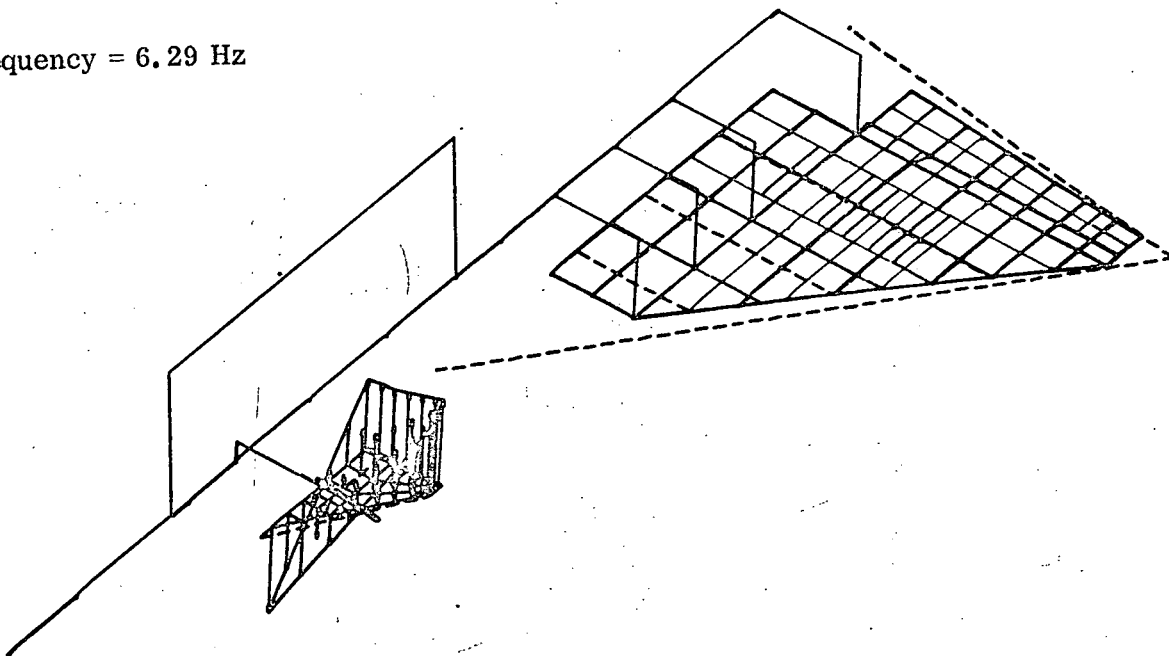


Figure 4-53. Ascent Flight Sixth Symmetric Mode

Frequency = 1.77 Hz

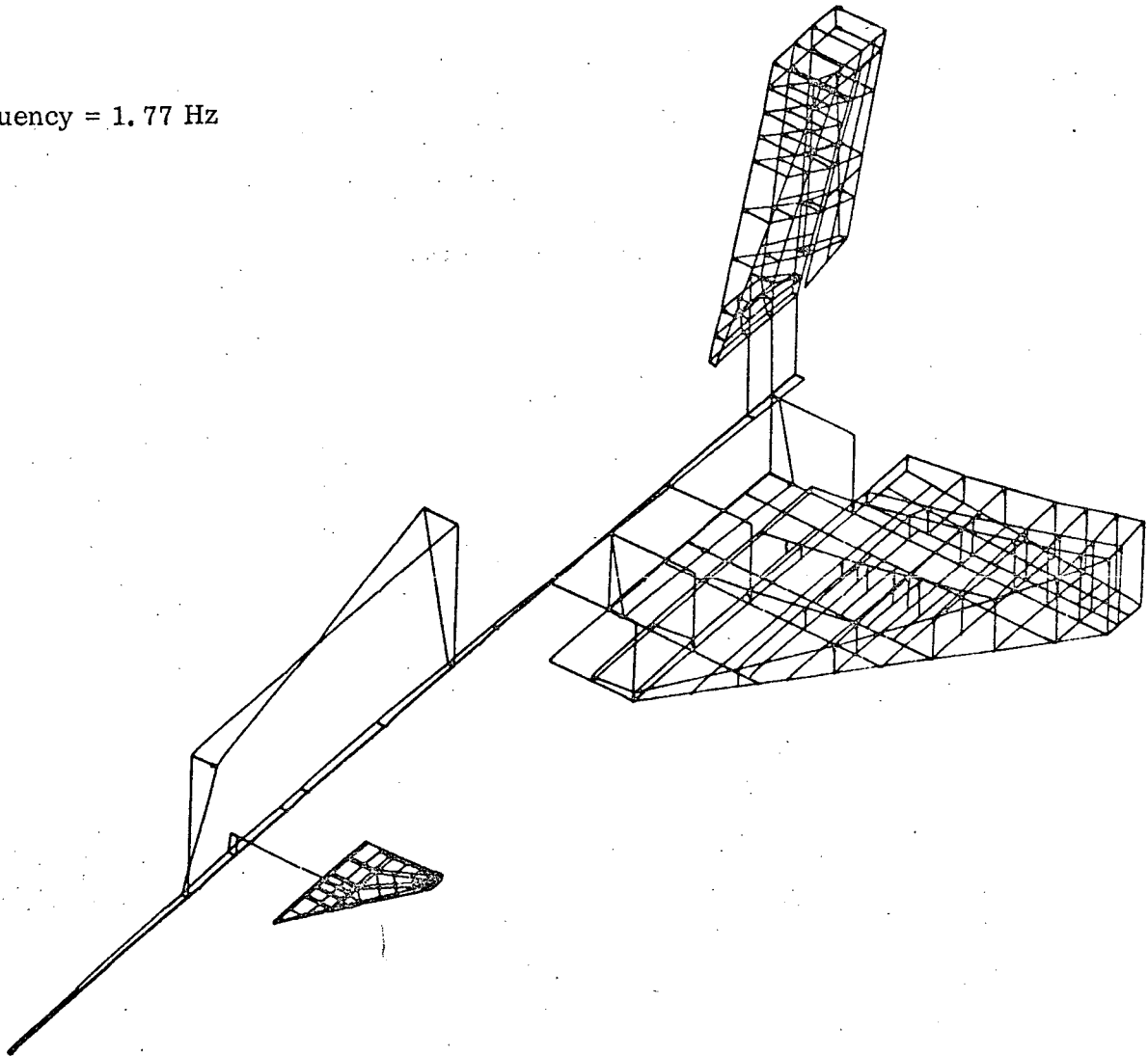


Figure 4-54. Ascent Flight First Antisymmetric Mode

Frequency = 2.19 Hz

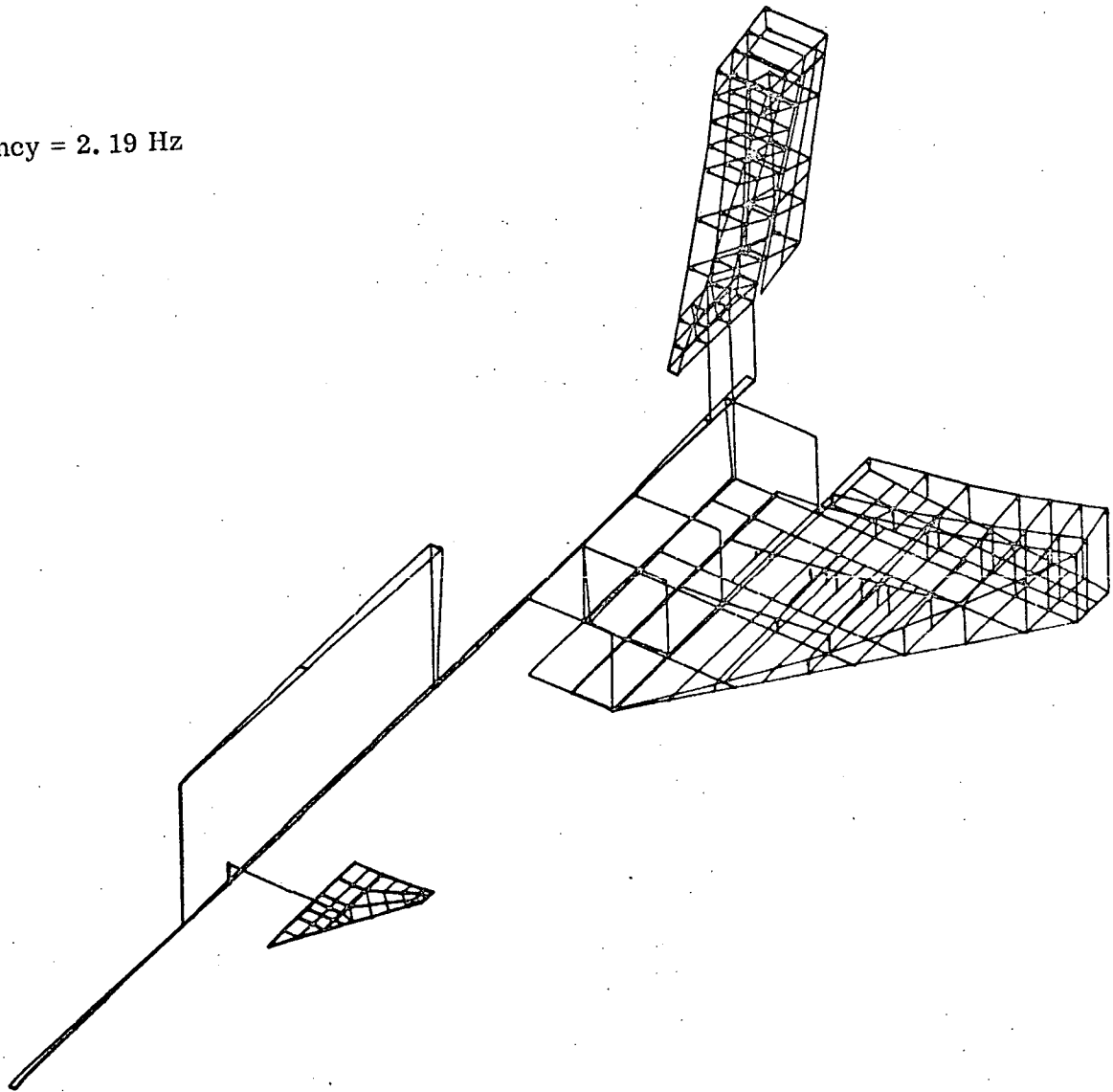


Figure 4-55. Ascent Flight Second Antisymmetric Mode

Frequency = 3.32 Hz

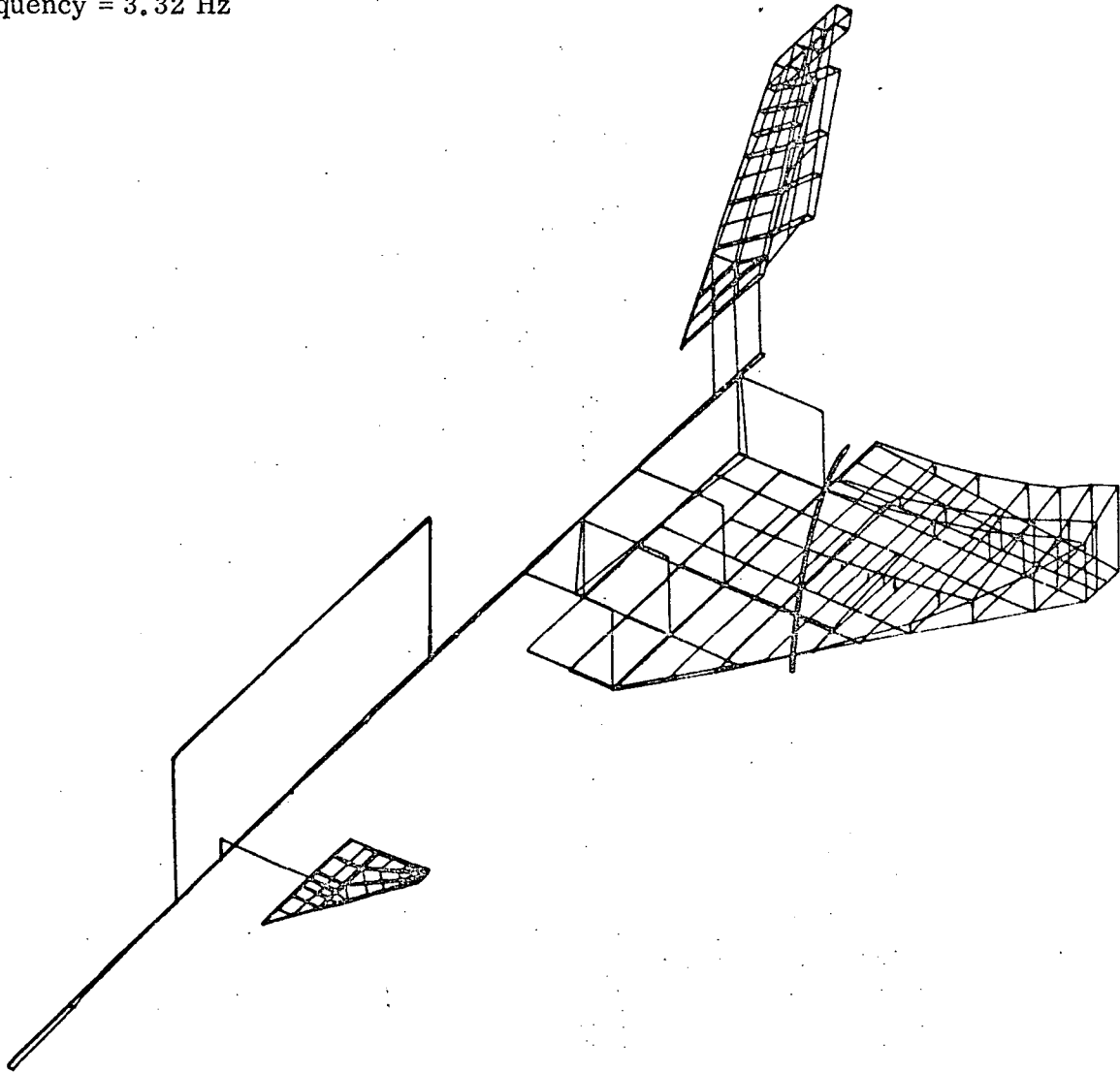


Figure 4-56. Ascent Flight Third Antisymmetric Mode

Frequency = 3.56 Hz

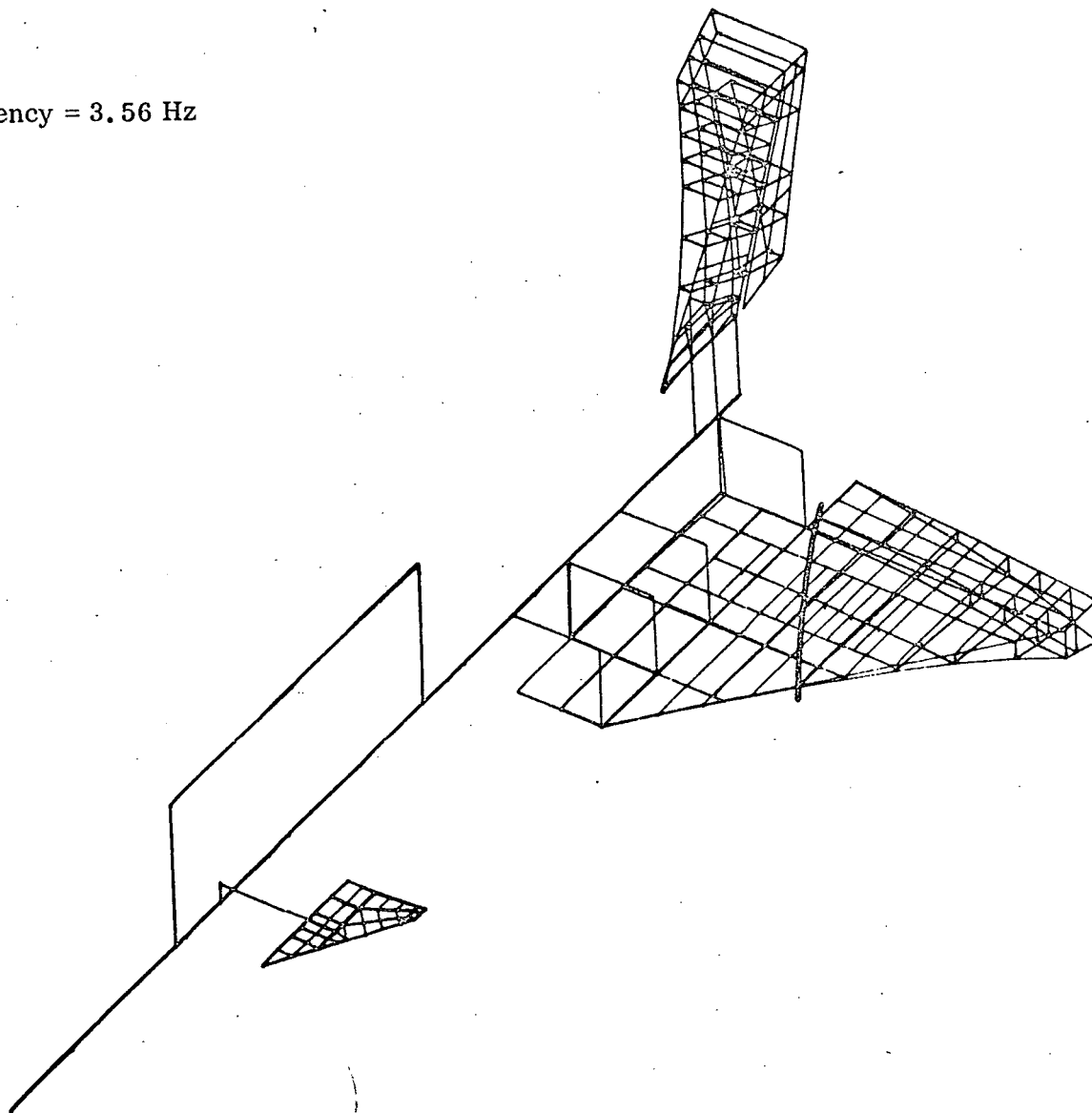


Figure 4-57. Ascent Flight Fourth Antisymmetric Mode

Frequency = 3.70 Hz

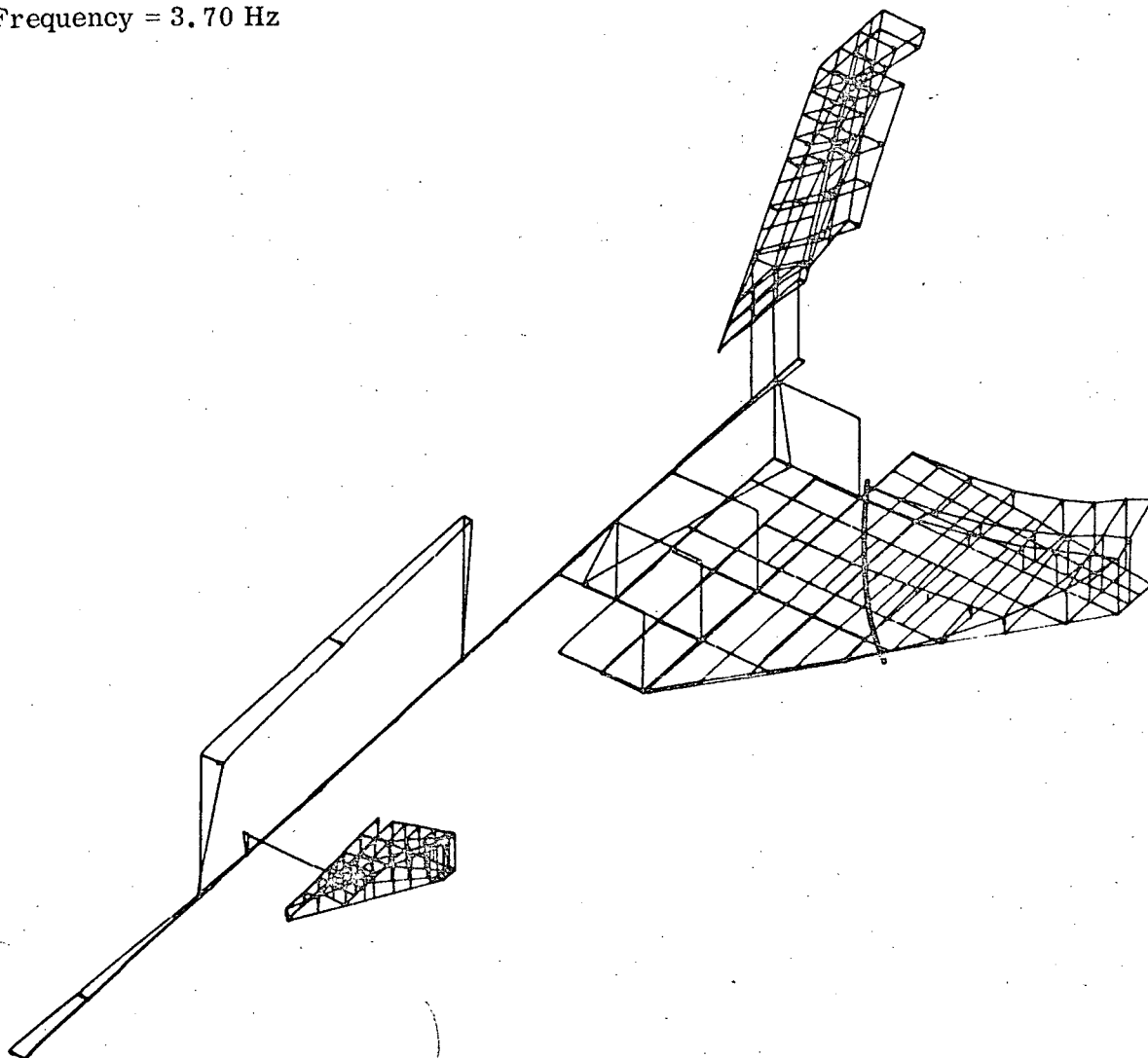


Figure 4-58. Ascent Flight Fifth Antisymmetric Mode

Frequency = 4.37 Hz

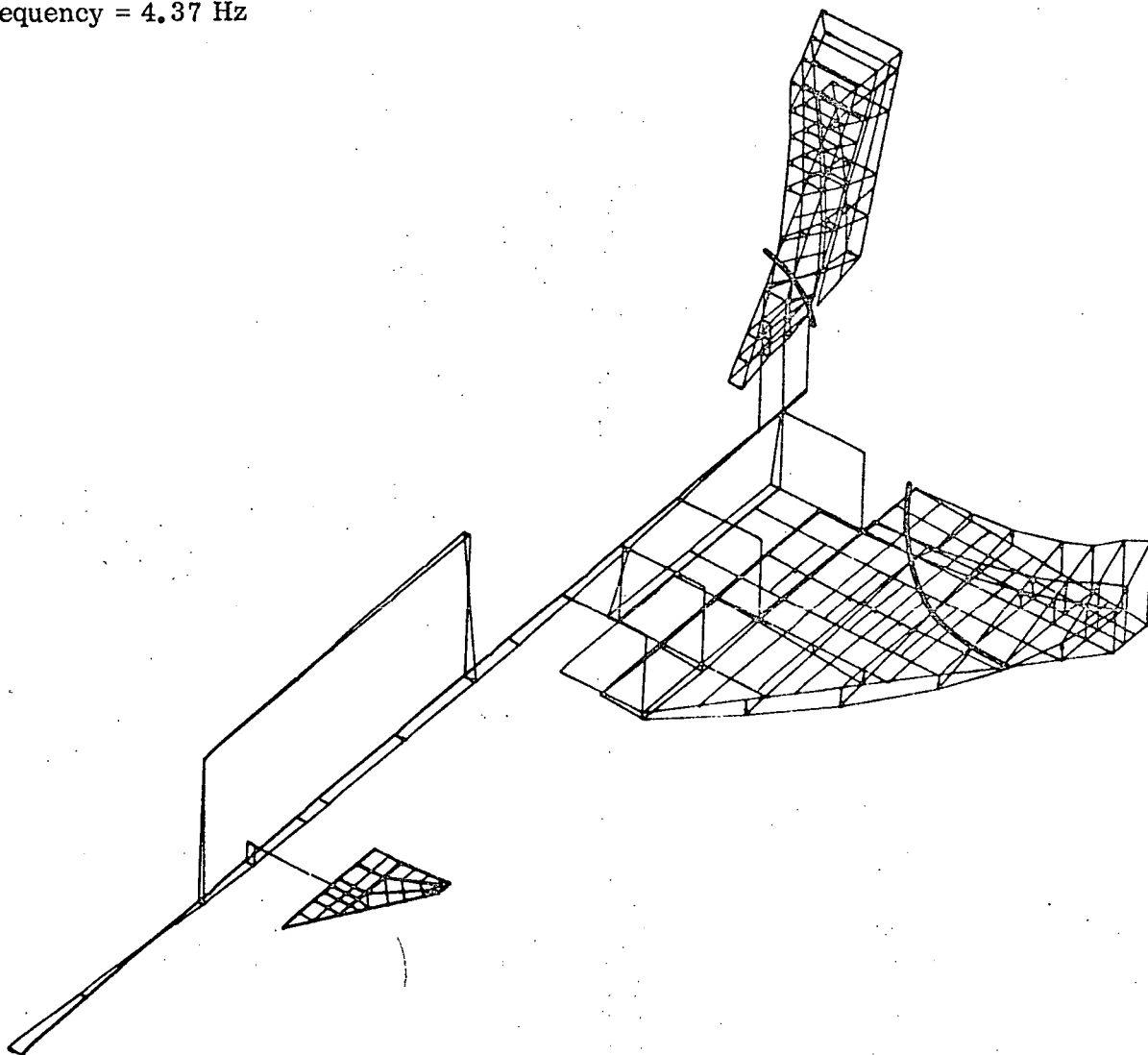


Figure 4-59. Ascent Flight Sixth Antisymmetric Mode

Frequency = 4.76 Hz

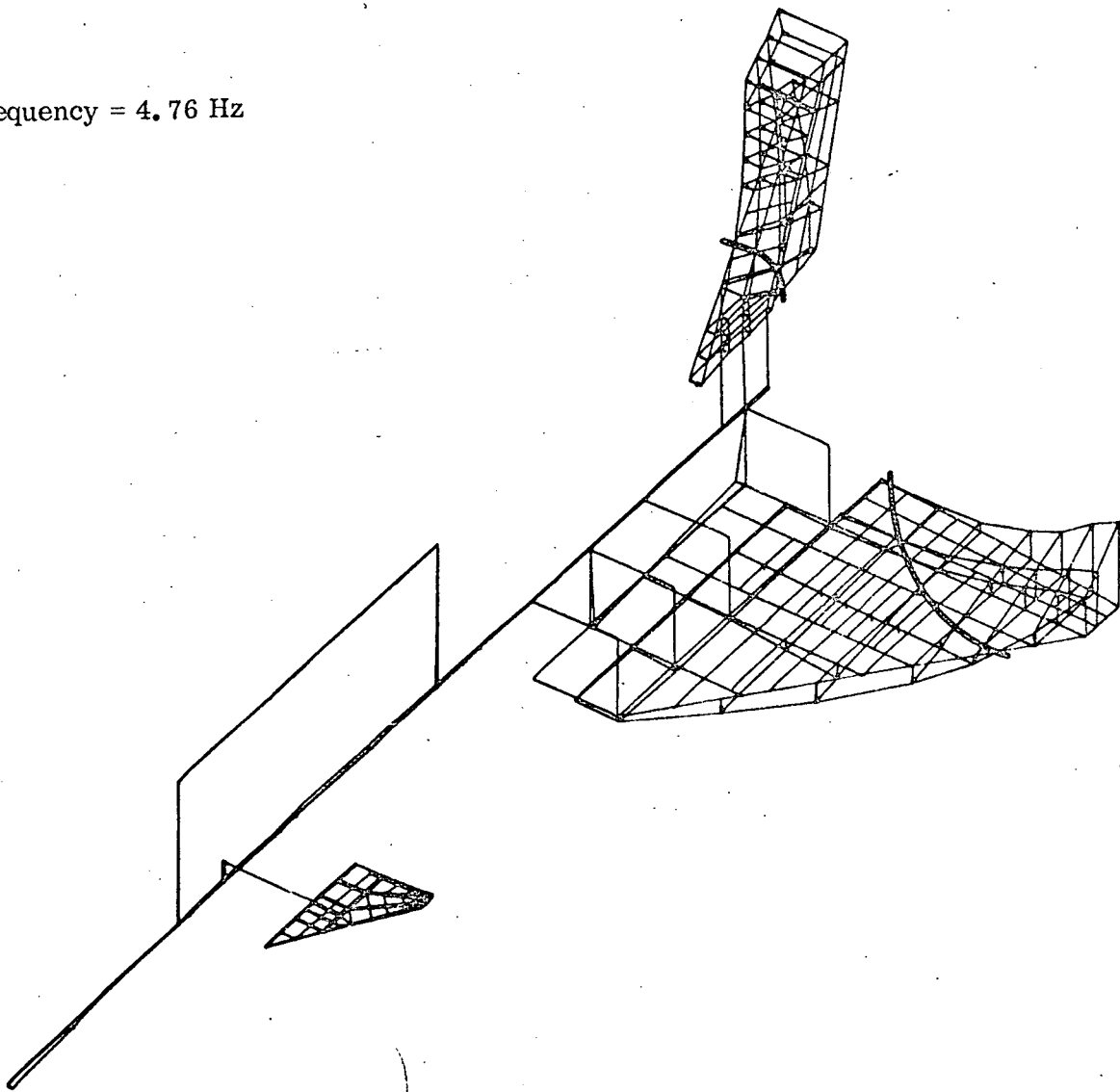


Figure 4-60. Ascent Flight Seventh Antisymmetric Mode

Symmetric turbulence response analysis results for the ascent configuration at $t = 59$ seconds are summarized in Table 4-6 for the SAS-off condition. The 3-DOF case considers rigid body vertical translation plus the two slosh modes. Rigid body pitch is added in the 4-DOF case and the 12-DOF case includes the first eight elastic modes. Figure 4-61 shows the booster normal acceleration \bar{A} and N_0 variations along the fuselage. Comparing these results with those for the booster return configuration shown in Figure 4-14 indicates that rms acceleration is generally higher during ascent but the characteristic frequency over the forward half of the booster is lower. Figures 4-62 and 4-63 show the fuselage crew compartment vertical acceleration transfer function and PSD plots. The A-matrix determinant magnitude and phase angle plots are shown in Figure 4-64 and in polar form in Figure 4-65.

The load summary for the ascent flight, symmetric, SAS-on case is given in Table 4-7. The rms loads are generally higher with SAS on than SAS off for the reasons previously mentioned. However, the loads are still well within the structural capabilities of the vehicle for design turbulence levels. For example, Figure 4-66 shows that to exceed the design limit values of wing root bending moment and shear, the rms turbulence velocity would have to be greater than 300 feet per second. The SAS-on crew station acceleration transfer function and PSD plots are contained in Figures 4-67 and 4-68, respectively. The A-matrix determinant is shown in Figures 4-69 and 4-70.

Table 4-8 contains the load summary for the ascent flight, antisymmetric, SAS-off case. The 3-DOF case consists of the two slosh modes and rigid body lateral translation. The 5-DOF case includes rigid body yaw and roll, and the 12-DOF condition includes the first seven elastic antisymmetric modes. The lateral acceleration \bar{A} and N_0 values for the booster fuselage are shown in Figure 4-71. Figures 4-72 and 4-73 show the crew station lateral acceleration transfer function and PSD, respectively. The A-matrix determinant is shown in Figures 4-74 and 4-75.

The SAS-on results for the antisymmetric ascent condition are summarized in Table 4-9. The lateral acceleration transfer function and PSD for the crew station are shown in Figures 4-76 and 4-77, and the A-matrix determinant is shown in Figures 4-78 and 4-79.

Table 4-6. Booster Ascent Flight Load Summary (SAS Off, Symmetric)

Response Item	3 DOF		4 DOF		12 DOF	
	\bar{A}	N_o (Hz)	\bar{A}	N_o (Hz)	\bar{A}	N_o (Hz)
Wing Root Shear (lb)	1,435	0.800	1,726	0.674	1,680	0.928
Wing Root Bending Moment (in. -lb)	0.407×10^6	0.846	0.492×10^6	0.707	0.477×10^6	0.980
Wing Root Torque About Station 3488.5 (in. -lb)	0.110×10^6	1.545	0.164×10^6	1.033	0.314×10^6	3.864
Fuselage Vertical Shear at Station 2800 (lb)	1,225	1.923	1,487	1.612	2,605	2.731
Fuselage Vertical Bending Moment at Station 2800 (in. -lb)	0.76×10^6	1.956	0.729×10^6	2.080	2.26×10^6	2.660
Forward Attachment Link Vertical Load (lb)	18,515	0.866	20,740	0.767	20,361	0.860
Aft Attachment Link Vertical Load (lb)	6,023	1.283	5,116	1.519	5,863	2.061

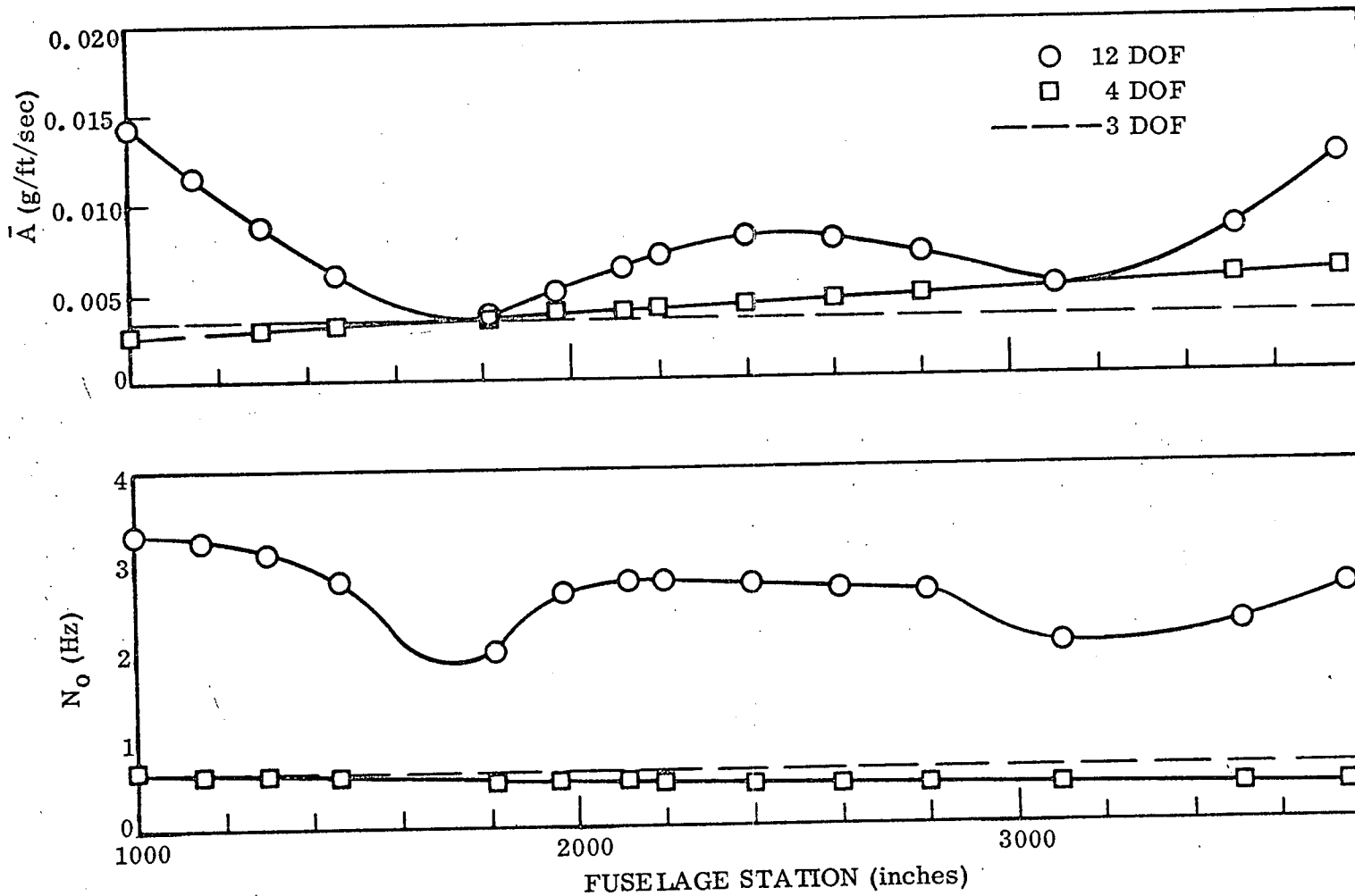


Figure 4-61. Ascent Flight, Fuselage Normal Acceleration \bar{A} and N_O (SAS Off, Symmetric)

PT. 2 ACC. AT F.S. 1150 CREW STATION
 LEGEND 0= TR+SLOSH += RB+SL X= RB+ 8 MDS +SL

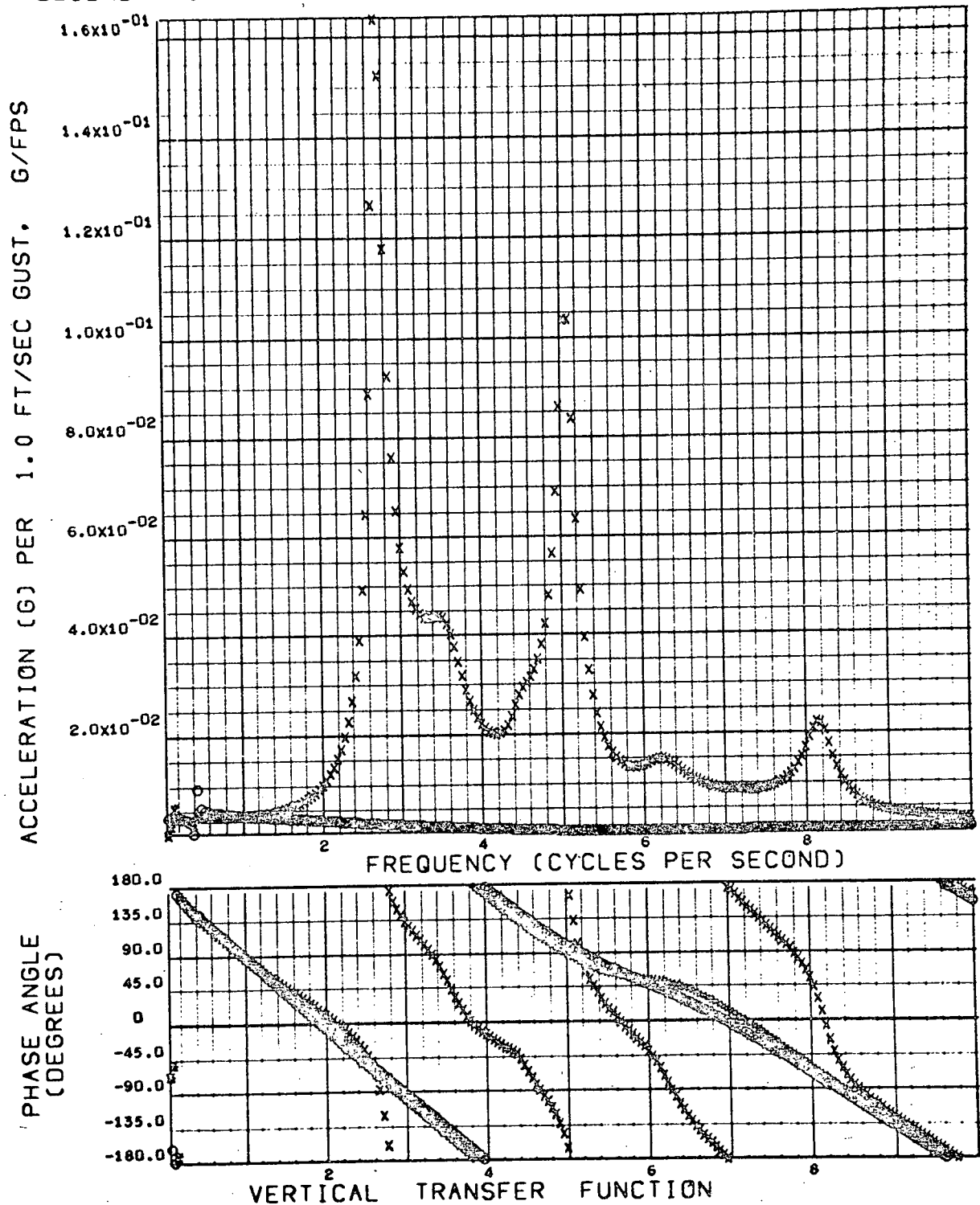


Figure 4-62. Ascent Flight Fuselage Normal Acceleration Transfer Function (SAS Off, Symmetric)

PT. 2 ACC. AT F.S. 1150 CREW STATION
 LEGEND 0= TR+SLOSH += RB+SL X= RB+ 8 MDS +SL

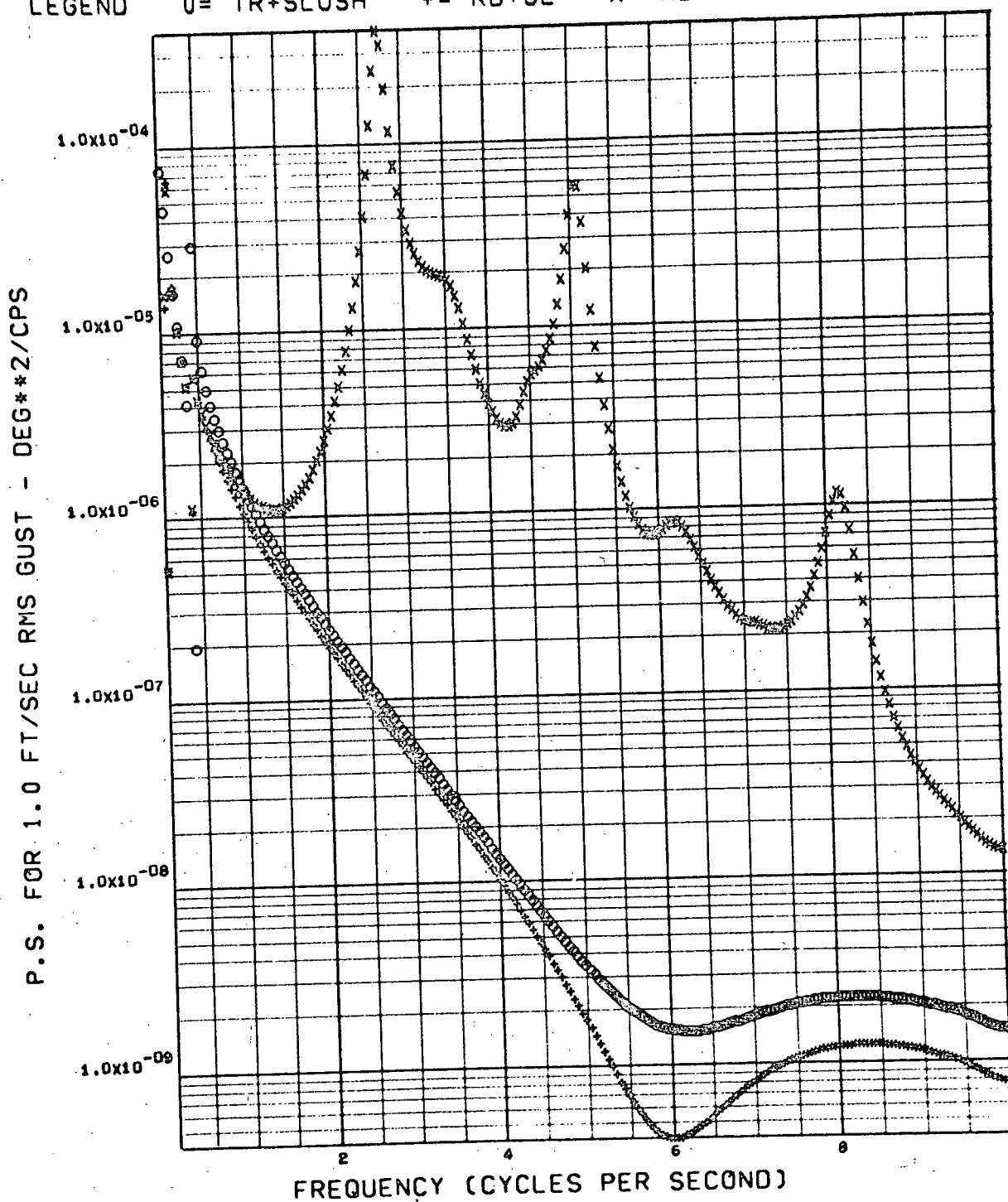


Figure 4-63. Ascent Flight Fuselage Normal Acceleration
 PSD (SAS Off, Symmetric)

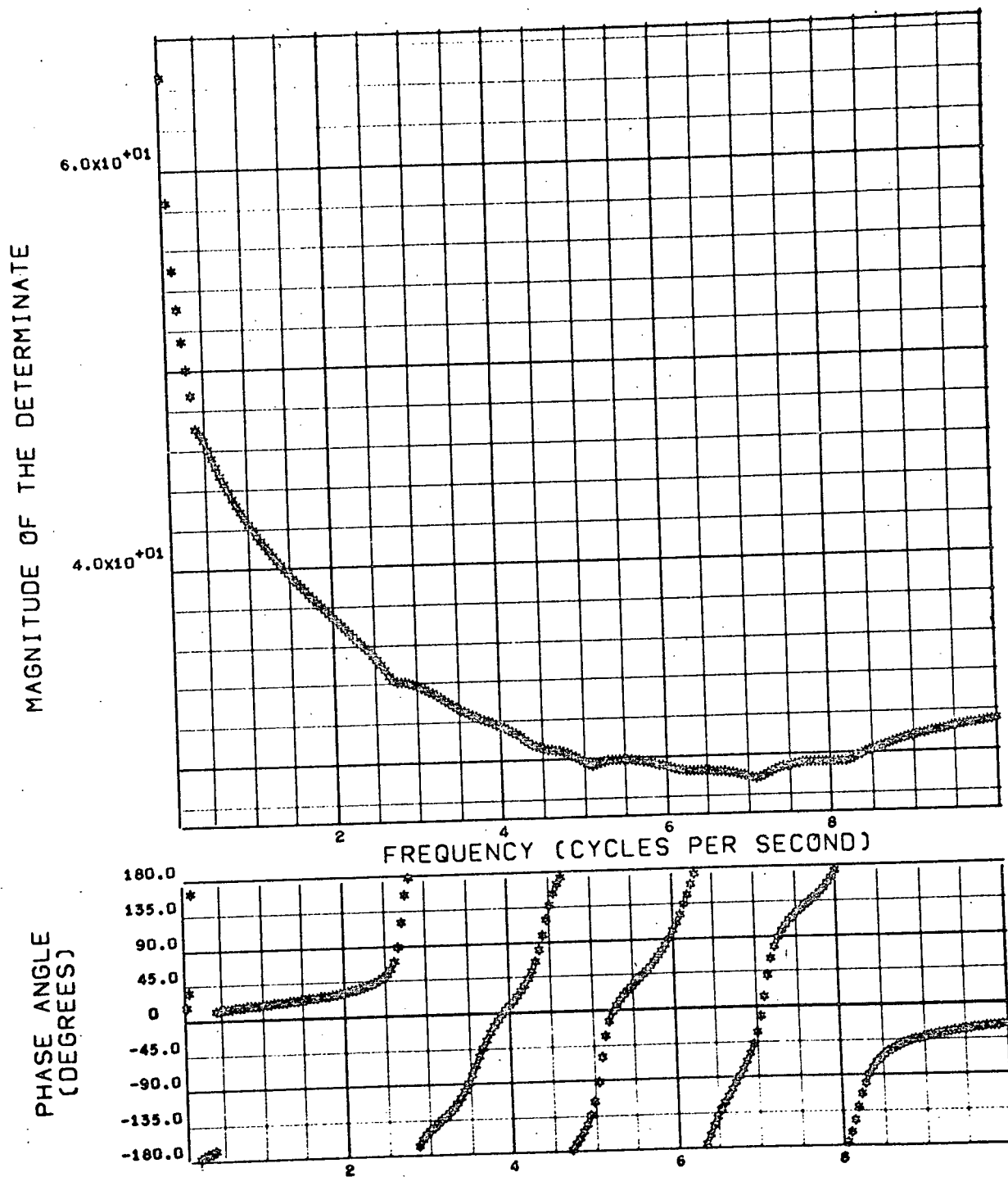


Figure 4-64. Ascent Flight A-Matrix Determinant Magnitude and Phase Angle (SAS Off, Symmetric)

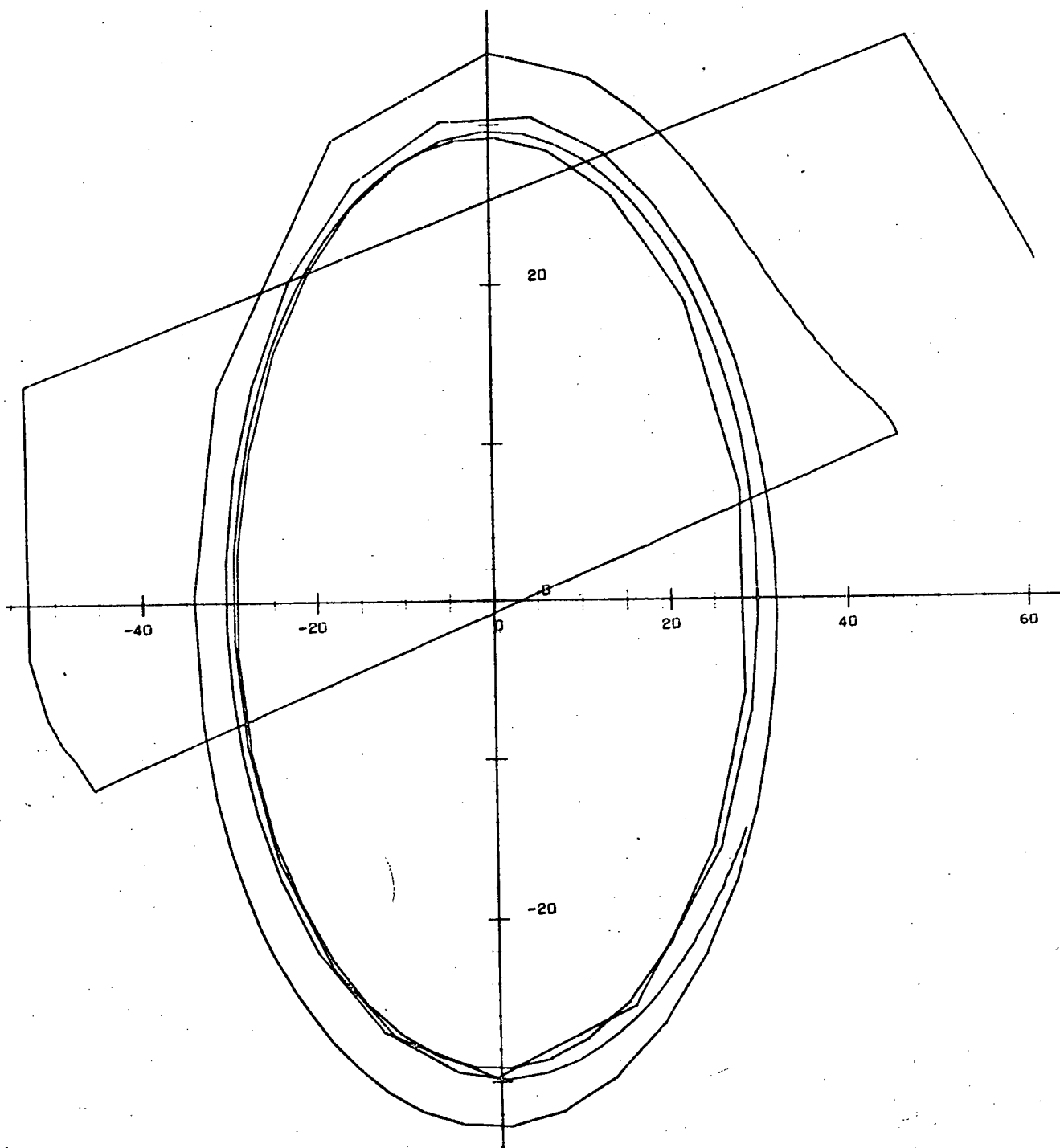


Figure 4-65. Ascent Flight A-Matrix Determinant
Polar Plot (SAS Off, Symmetric)

Table 4-7. Booster Ascent Flight Load Summary (SAS On, Symmetric)

Response Item	3 DOF		4 DOF		12 DOF	
	\bar{A}	N_O (Hz)	\bar{A}	N_O (Hz)	\bar{A}	N_O (Hz)
Wing Root Shear (lb)	1,435	0.800	1,486	0.783	1,568	1.316
Wing Root Bending Moment (in.-lb)	0.407×10^6	0.846	0.417×10^6	0.831	0.440×10^6	1.350
Wing Root Torque About Station 3488.5 (in.-lb)	0.110×10^6	1.545	0.548	0.704	1.623×10^6	1.783
Fuselage Vertical Shear at Station 2800 (lb)	1,225	1.923	7,955	0.708	8,870	1.841
Fuselage Vertical Bending Moment at Station 2800 (in.-lb)	0.760×10^6	1.956	4.23×10^6	0.731	3.924×10^6	2.348
Forward Attachment Link Vertical Load (lb)	18,515	0.866	21,413	0.835	32,193	1.349
Aft Attachment Link Vertical Load (lb)	6,023	1.283	14,522	0.769	15,039	1.636

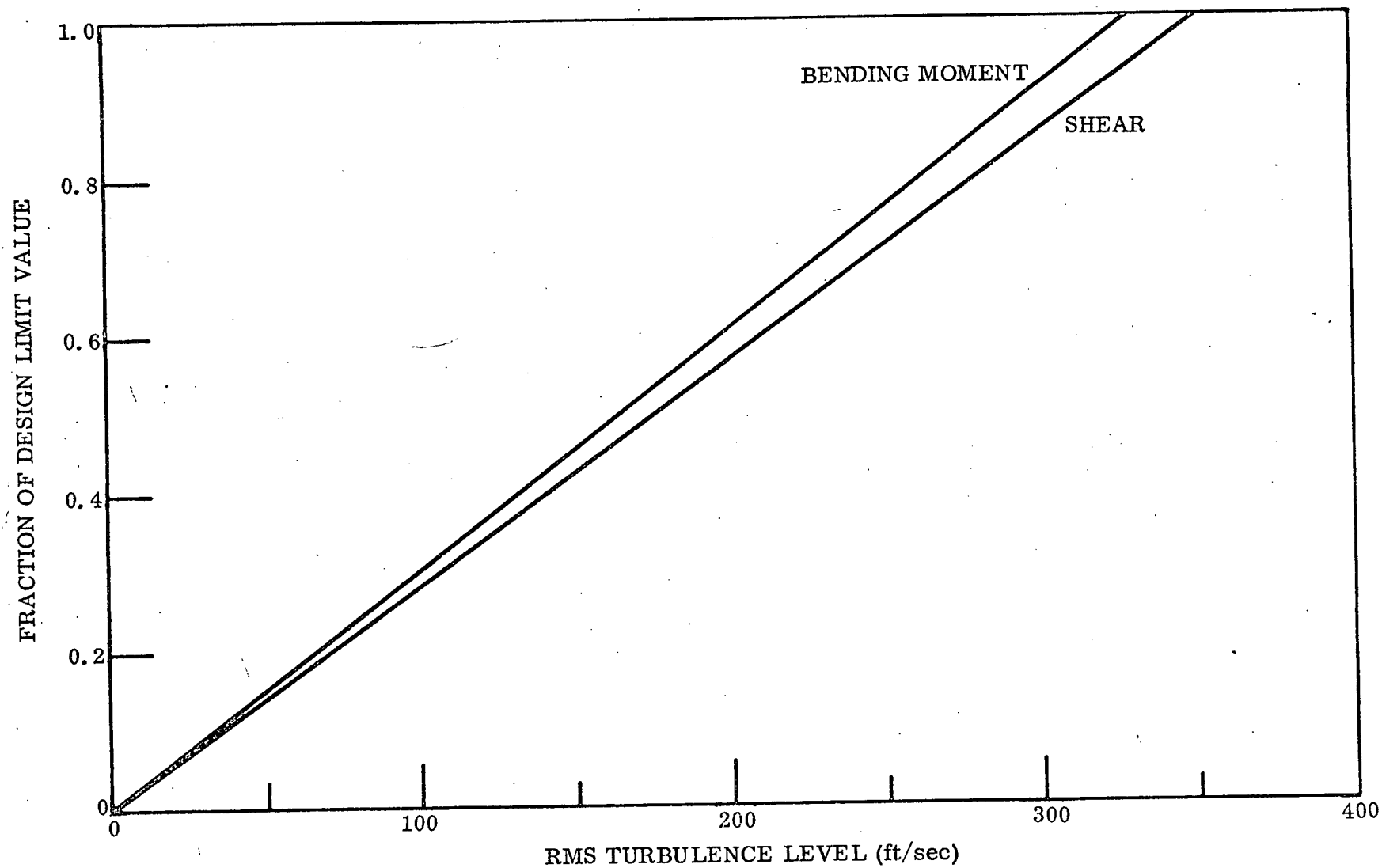


Figure 4-66. Ascent Flight Wing Root RMS Shear and Bending Moment Versus RMS Turbulence Level (SAS On, Symmetric)

PT. 2 ACC. AT F.S. 1150 CREW STATION
 LEGEND 0= TR+SLOSH += RB+SL X= RB+ 8 MDS +SL

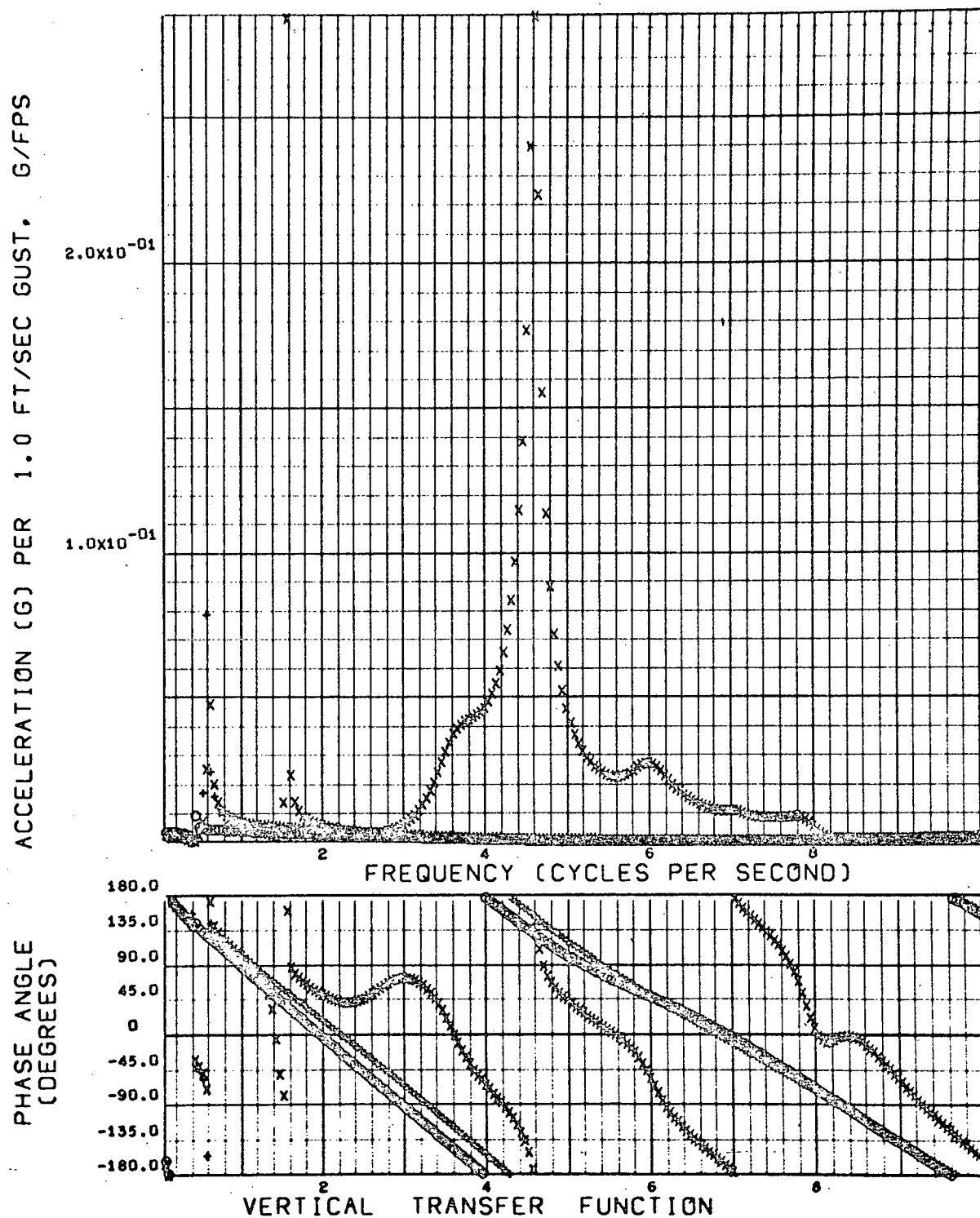


Figure 4-67. Ascent Flight Fuselage Normal Acceleration Transfer Function (SAS On, Symmetric)

PT. 2 ACC. AT F.S. 1150 CREW STATION
 LEGEND 0= TR+SLOSH += RB+SL X= RB+ 8 MDS +SL

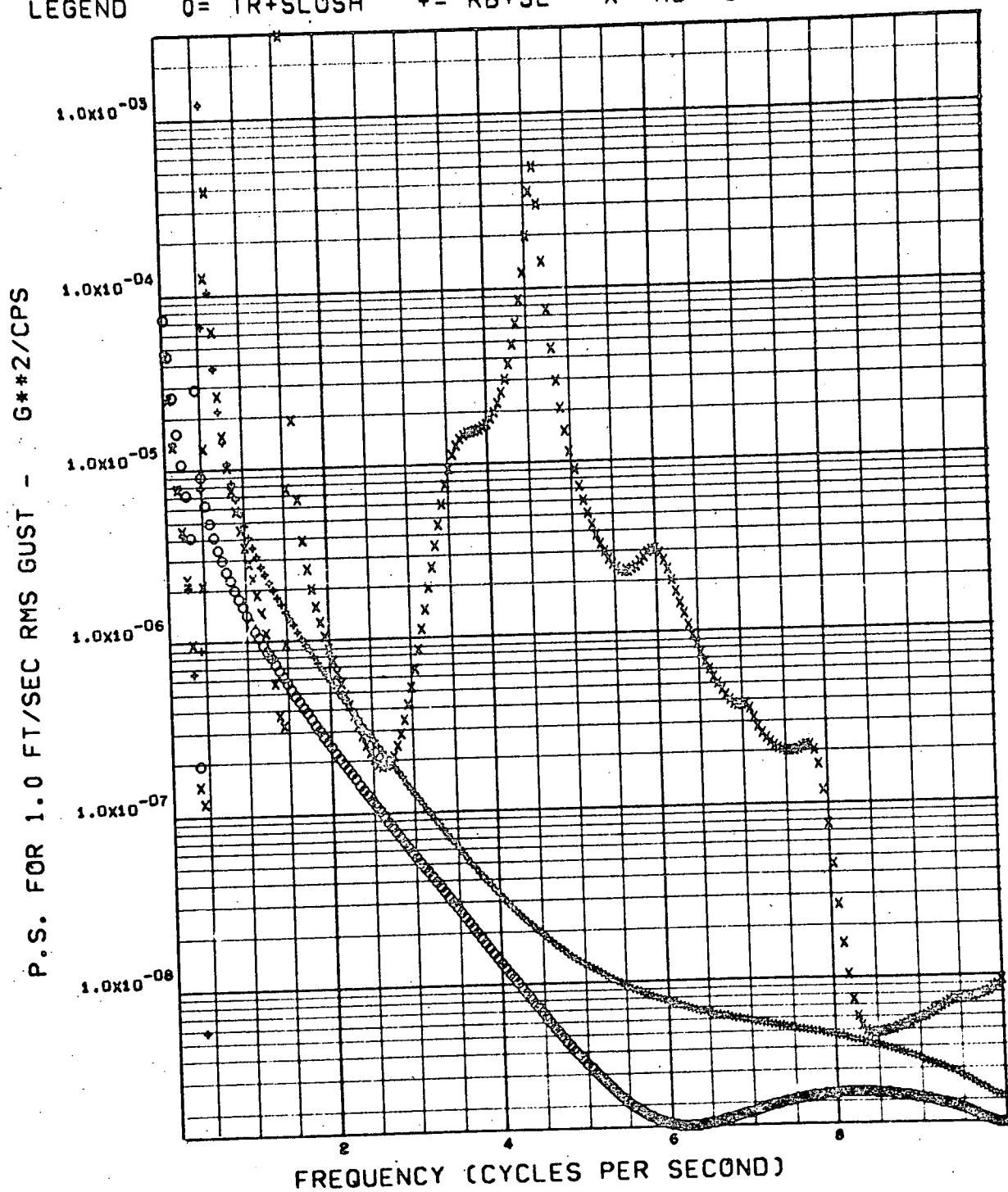


Figure 4-68. Ascent Flight Fuselage Normal Acceleration
 PSD (SAS On, Symmetric)

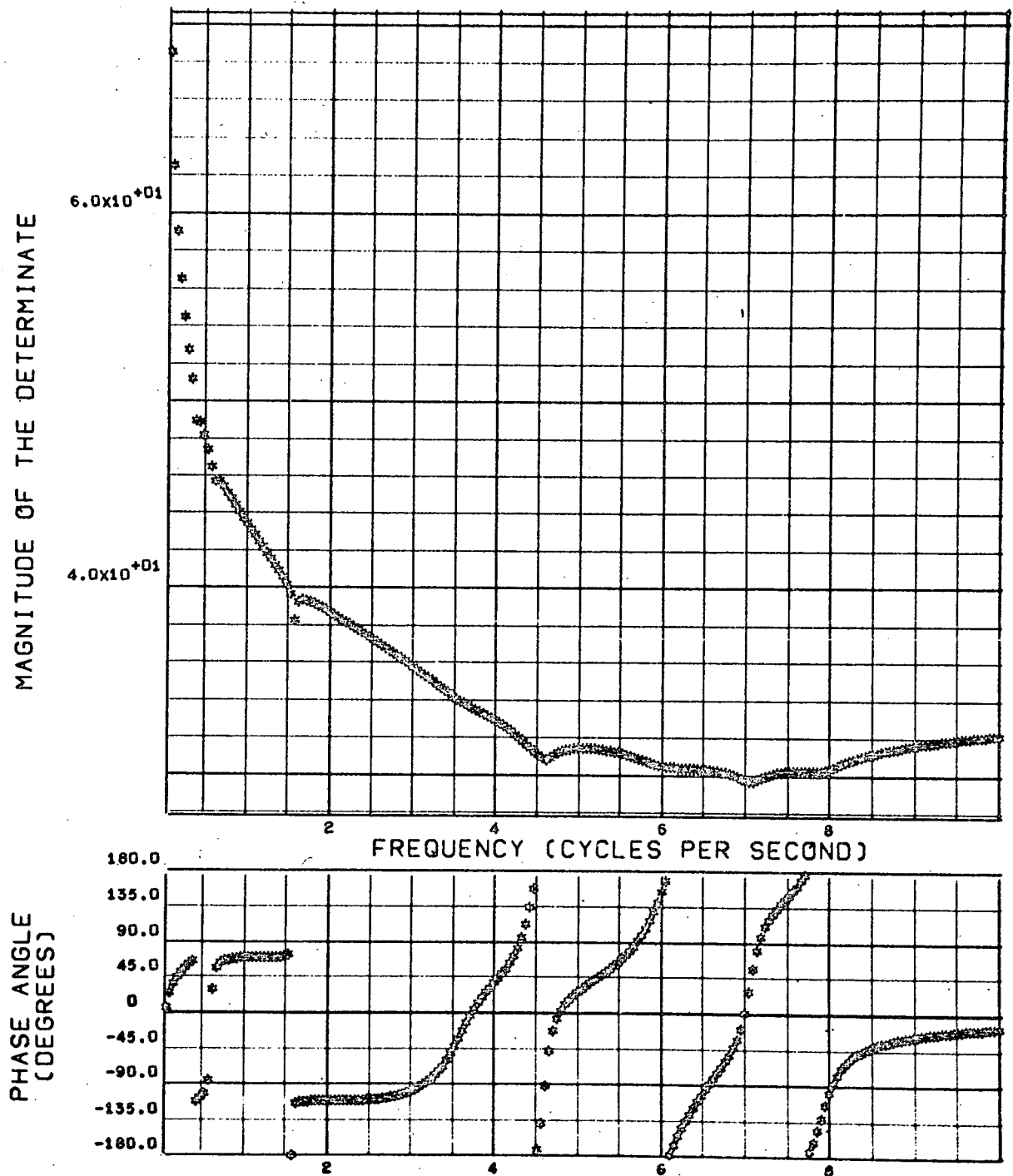


Figure 4-69. Ascent Flight A-Matrix Determinant Magnitude and Phase Angle (SAS On, Symmetric)

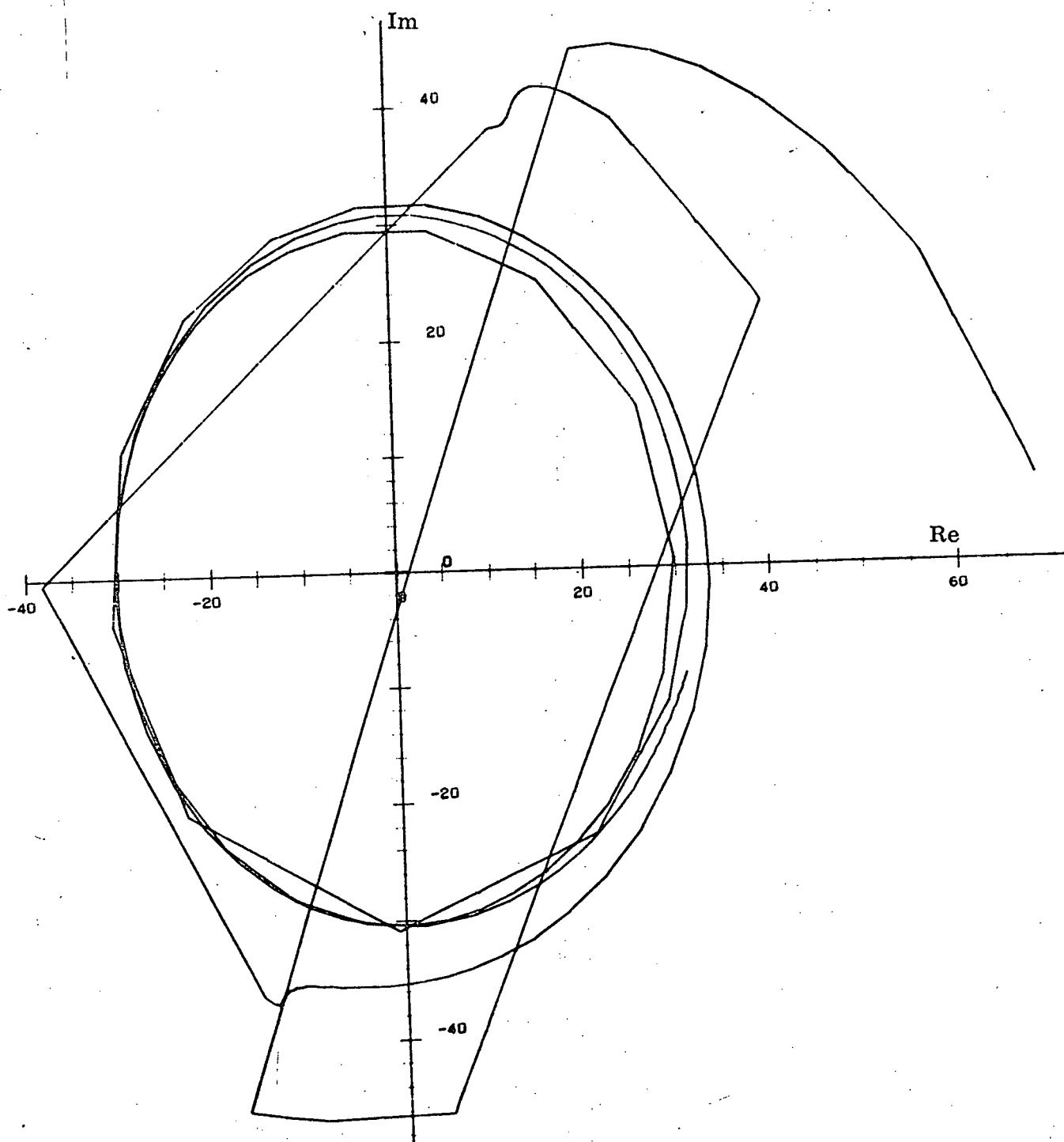


Figure 4-70. Ascent Flight A-Matrix Determinant
Polar Plot (SAS On, Symmetric)

Table 4-8. Booster Ascent Flight Load Summary (SAS Off, Antisymmetric)

Response Item	3 DOF		5 DOF		12 DOF	
	\bar{A}	N_O (Hz)	\bar{A}	N_O (Hz)	\bar{A}	N_O (Hz)
Wing Root Shear (lb)	0	0	384	0.313	372.0	1.858
Wing Root Bending Moment (in.-lb)	0	0	0.137×10^6	0.251	0.114×10^6	1.598
Wing Root Torque About Station 3488.5 (in.-lb)	0	0	32,308	0.702	50,198	2.567
Fuselage Lateral Shear at Station 2800 (lb)	1,399	1.177	3,096	0.718	3,378	1.166
Fuselage Lateral Bending Moment at Station 2800 (in.-lb)	1.67×10^6	0.922	3.22×10^6	0.812	3.59×10^6	1.429
Forward Attachment Link Lateral Load (lb)	3,134	1.074	2,908	0.849	3,611	1.444
Aft Attachment Link Lateral Load (lb)	2,484	1.536	653	2.318	1,470	2.118

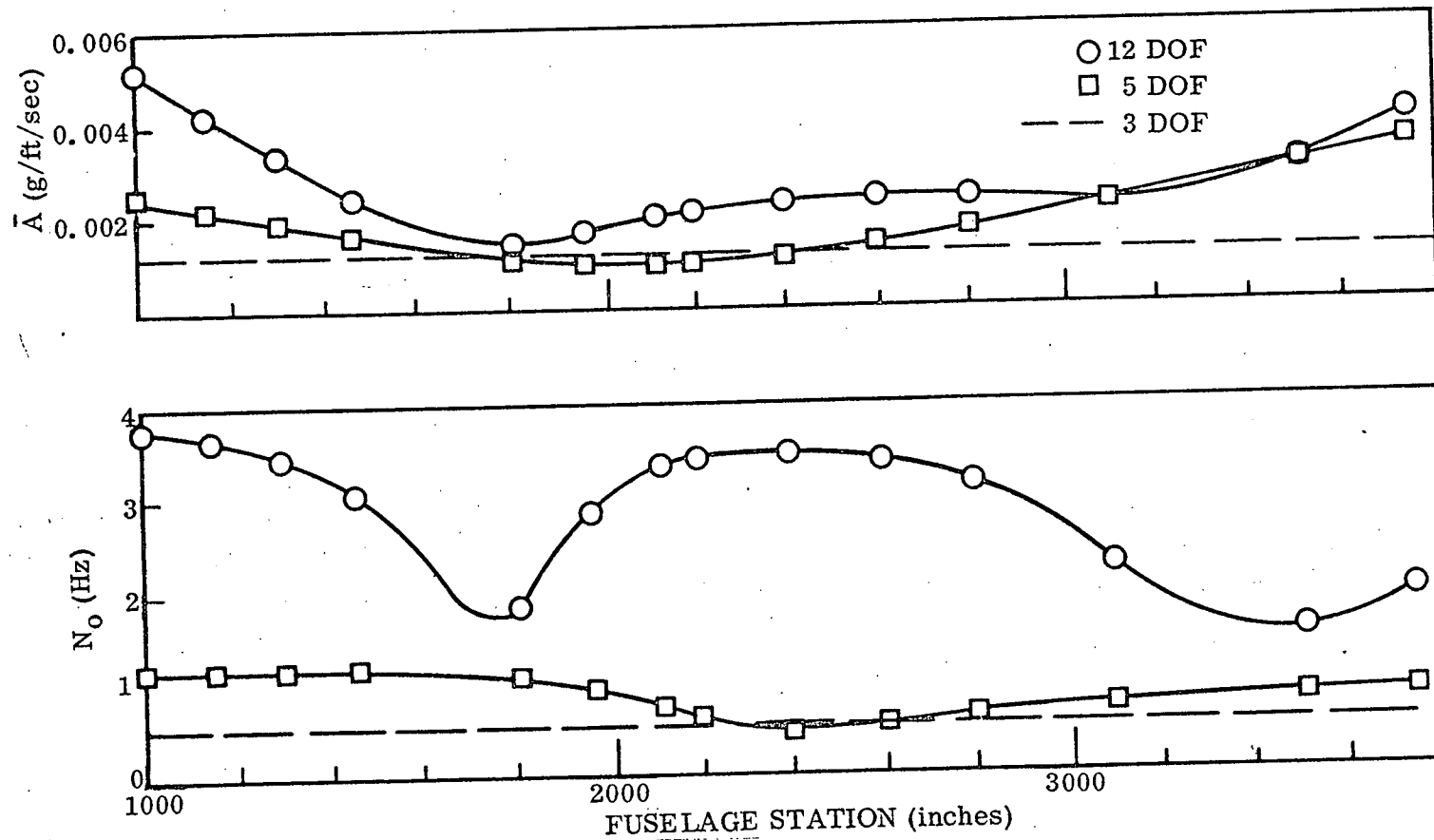


Figure 4-71. Ascent Flight Fuselage Lateral Acceleration \bar{A} and N_O (SAS Off, Antisymmetric)

PT. 2 ACC. AT F.S. 1150 CREW STATION
 CIRCLE 1 RB + SLOSH PLUS 3 RB + SLOSH X = 10 DOF

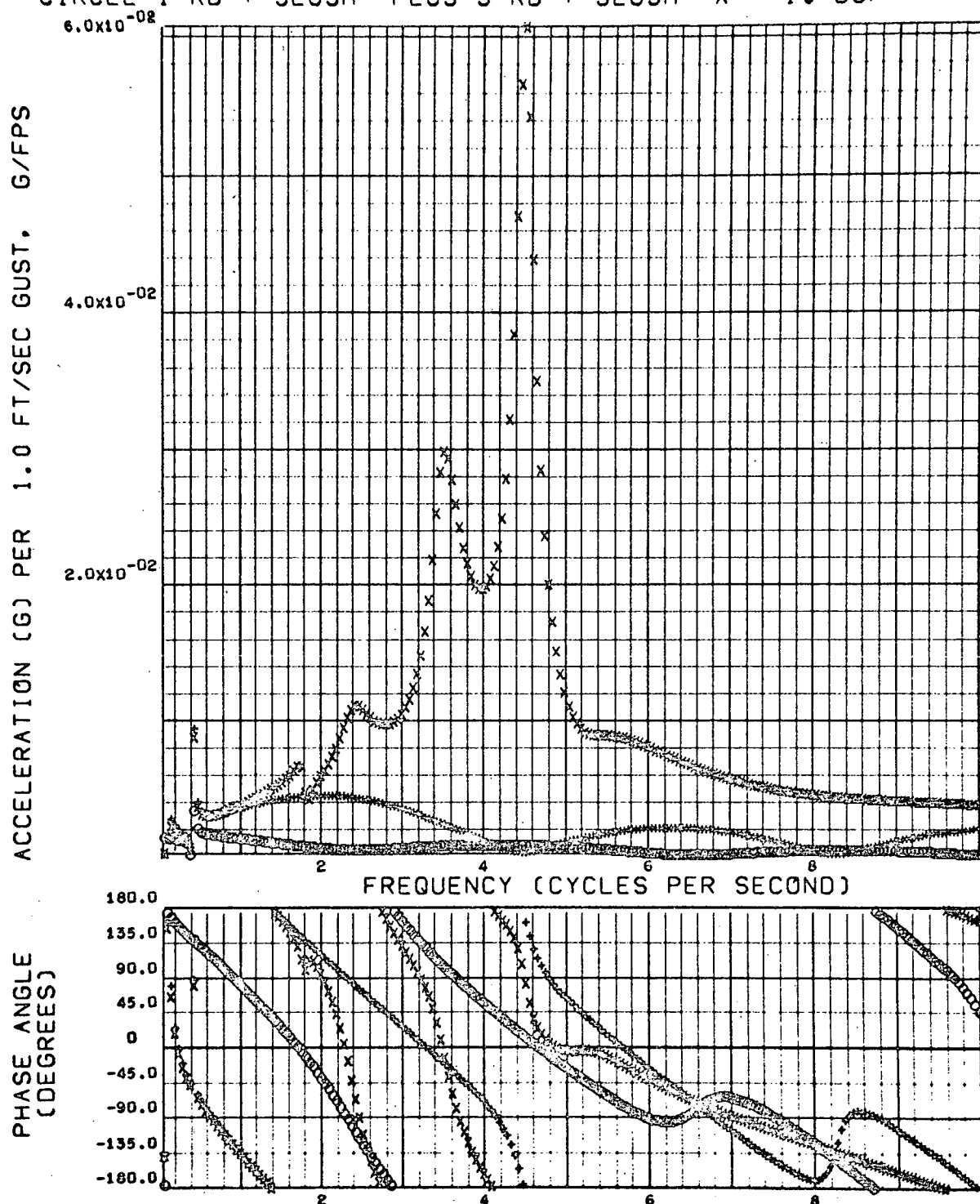


Figure 4-72. Ascent Flight Fuselage Lateral Acceleration Transfer Function (SAS Off, Antisymmetric)

PT. 2 ACC. AT F.S. 1150 CREW STATION
 CIRCLE 1 RB + SLOSH PLUS 3 RB + SLOSH X = 10 DOF

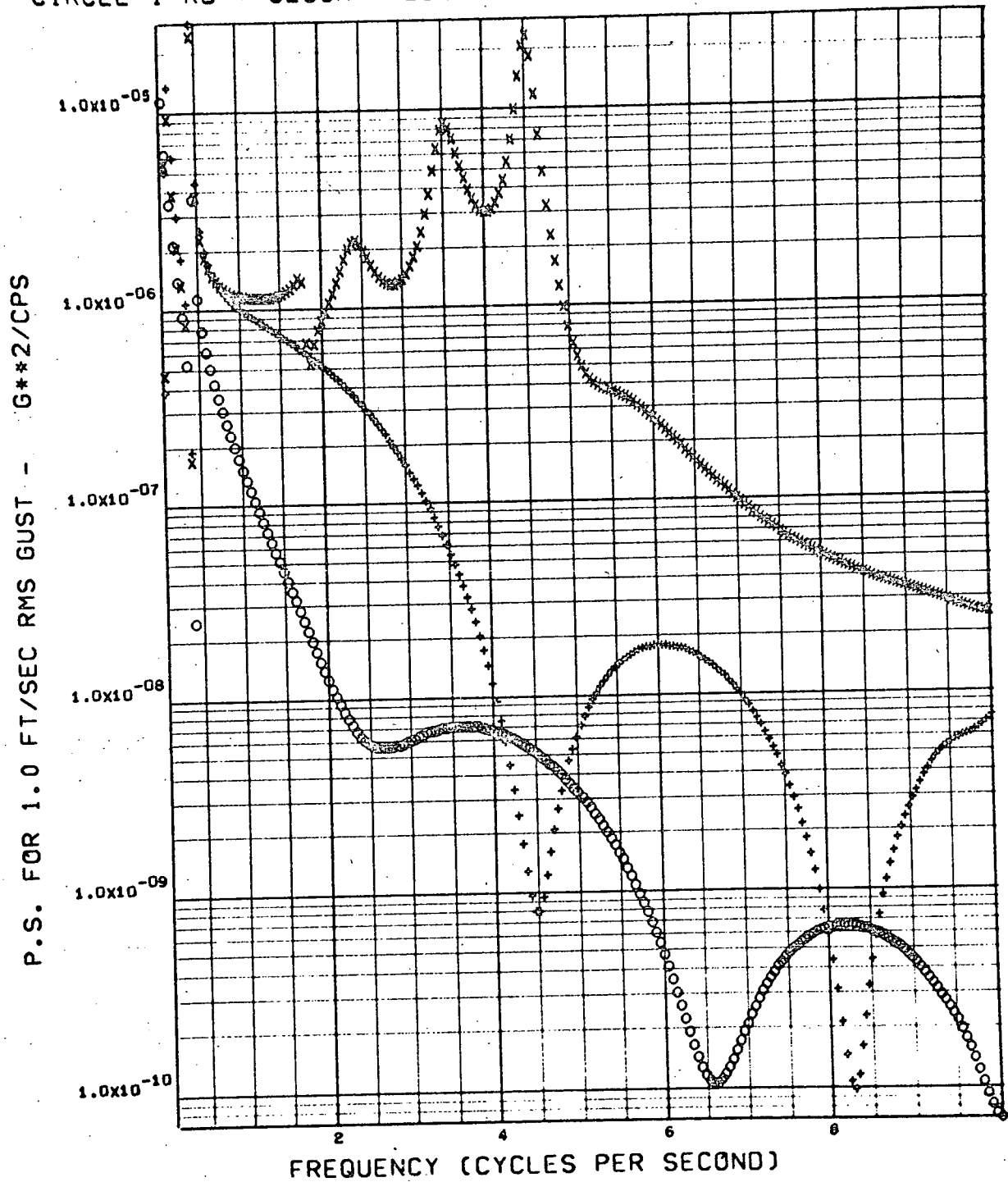


Figure 4-73. Ascent Flight Fuselage Lateral Acceleration
 PSD (SAS Off, Antisymmetric)

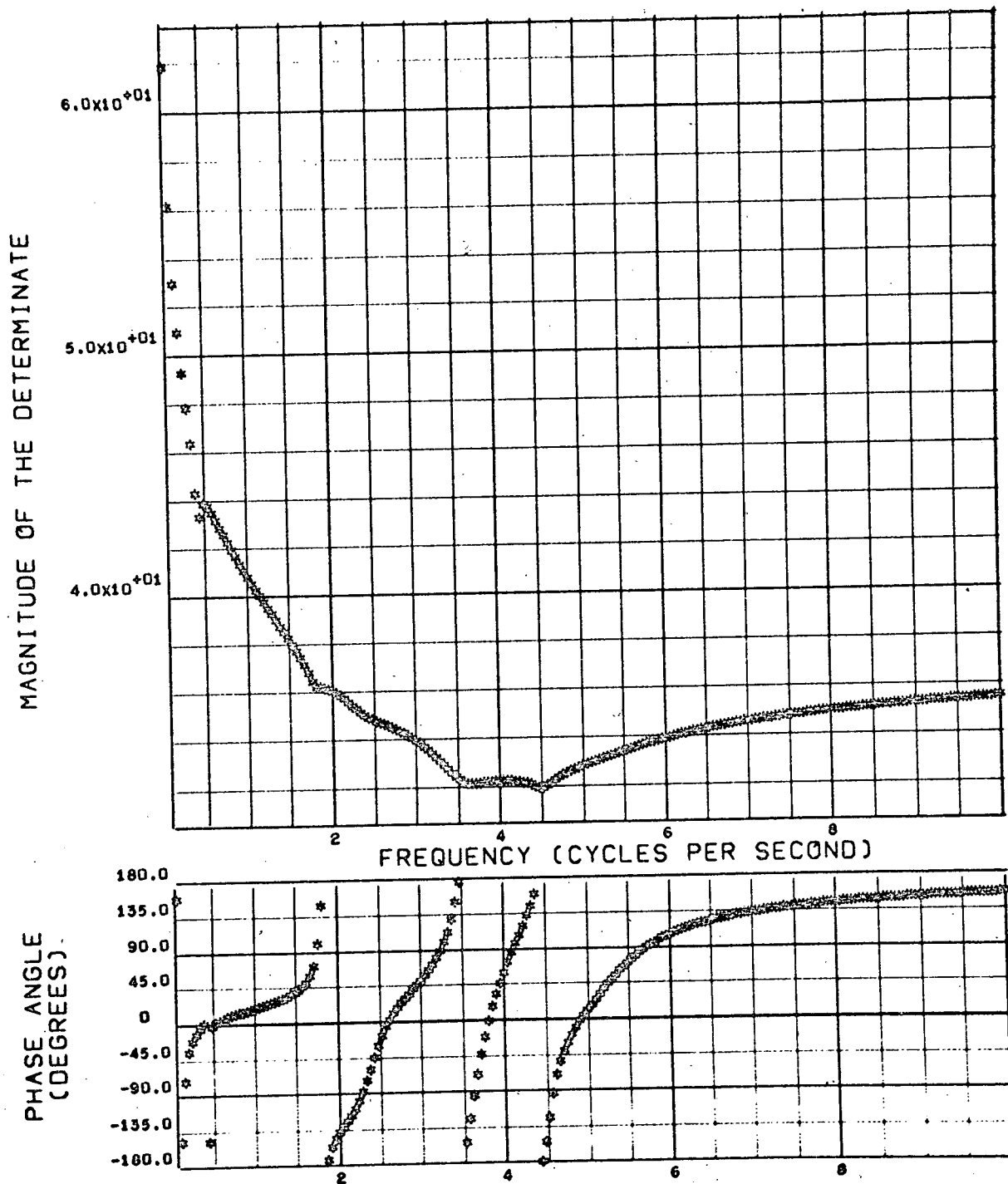


Figure 4-74. Ascent Flight A-Matrix Determinant Magnitude and Phase Angle (SAS Off, Antisymmetric)

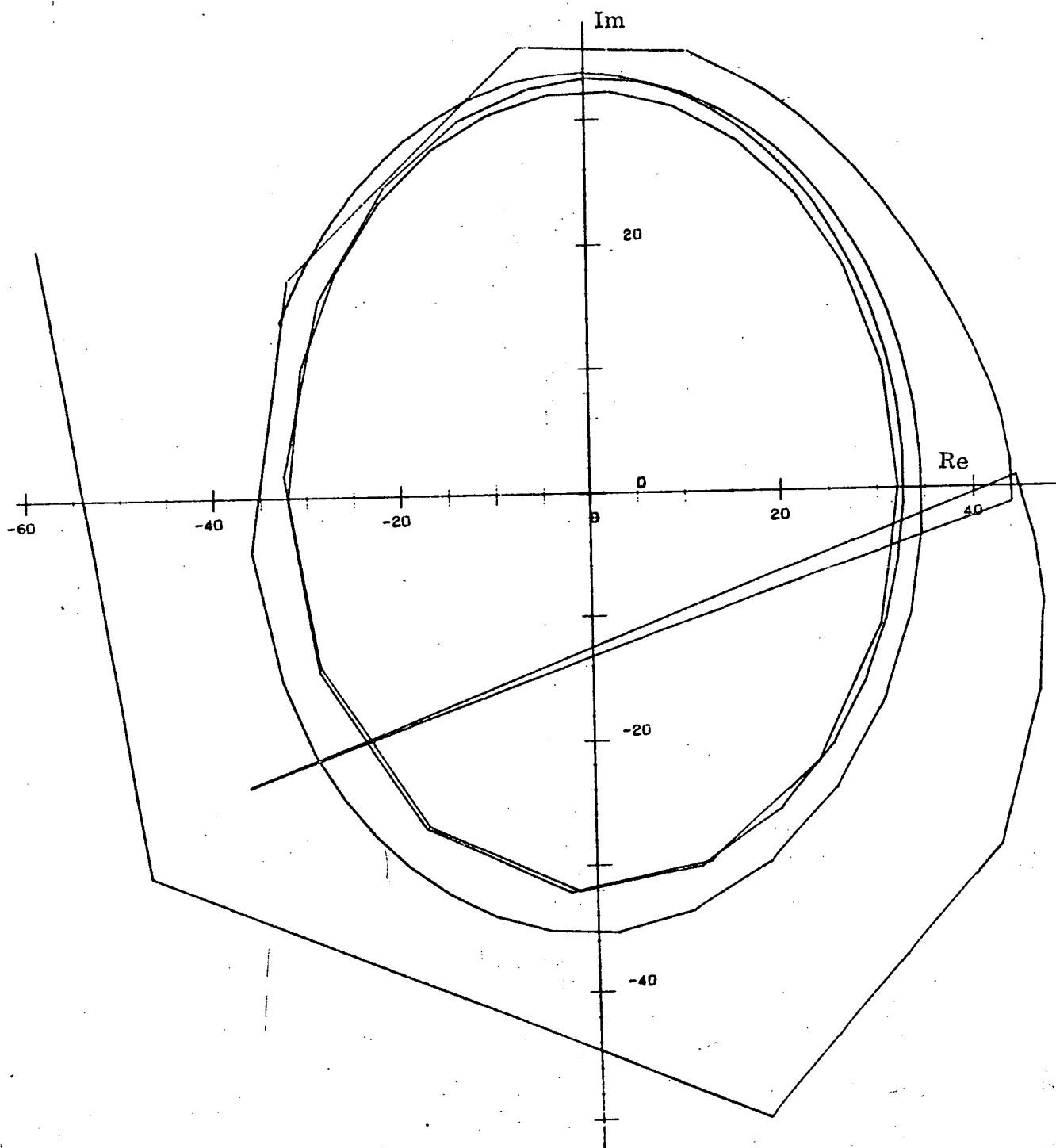


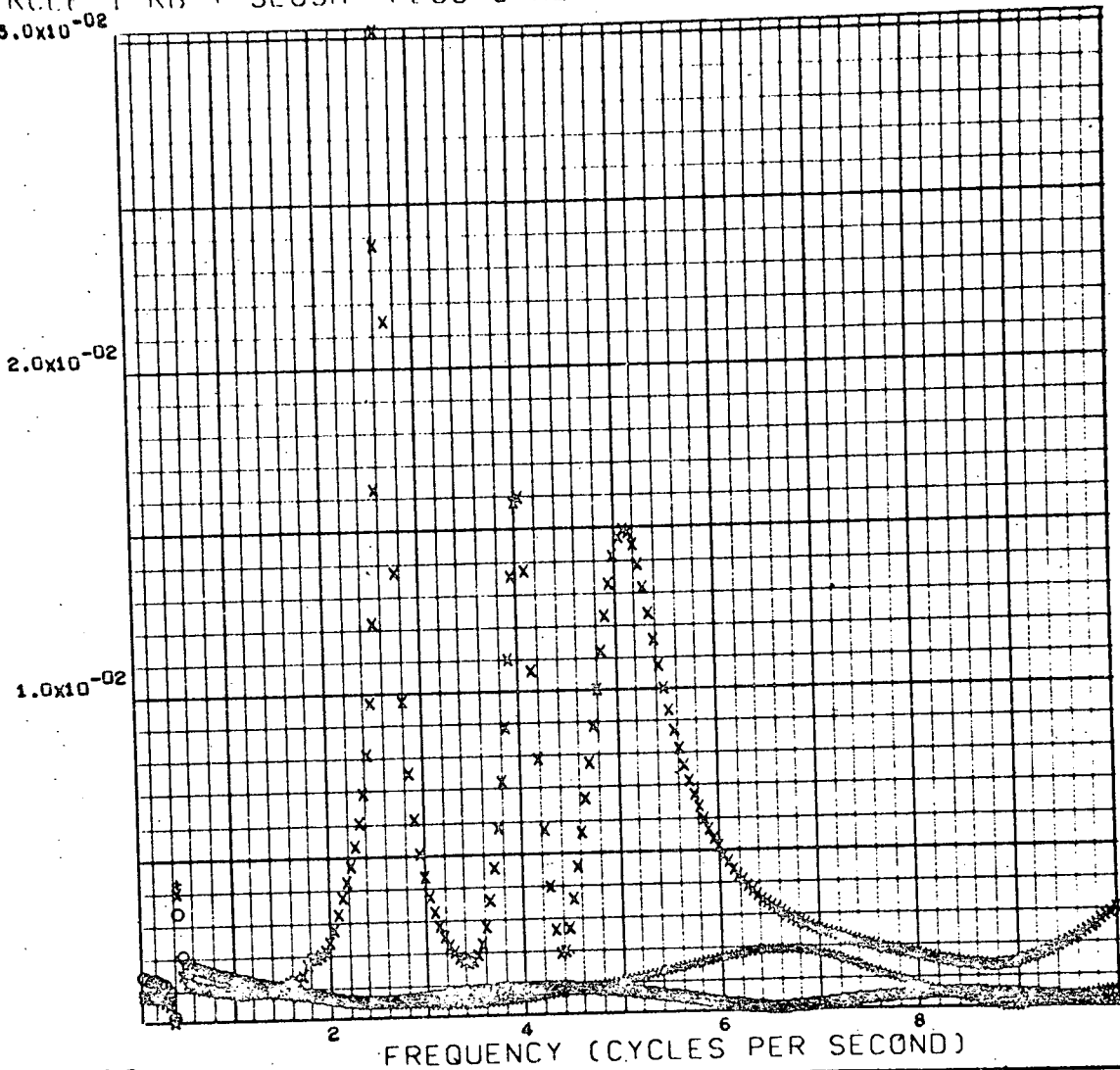
Figure 4-75. Ascent Flight A-Matrix Determinant
Polar Plot (SAS Off, Antisymmetric)

Table 4-9. Booster Ascent Flight Load Summary (SAS On, Antisymmetric)

Response Item	3 DOF		5 DOF		12 DOF	
	\bar{A}	N_o (Hz)	\bar{A}	N_o (Hz)	\bar{A}	N_o (Hz)
Wing Root Shear (lb)	0	0	2.40	3.712	433	2.985
Wing Root Bending Moment (in. -lb)	0	0	611	3.651	0.109×10^6	3.000
Wing Root Torque About Station 3488.5 (in. -lb)	0	0	518	3.800	57,600	3.980
Fuselage Lateral Shear at Station 2800 (lb)	1,399	1.177	910	0.898	1,315	2.078
Fuselage Lateral Bending Moment at Station 2800 (in. -lb)	1.67×10^6	0.922	1.08×10^6	0.842	1.56×10^6	2.110
Forward Attachment Link Lateral Load (lb)	3,134	1.074	2,475	0.899	4,720	3.341
Aft Attachment Link Lateral Load (lb)	2,484	1.536	3,233	1.167	9,369	3.358

PL. 2 ACC. AT I.S. 1150 CREW STATION
 CIRCLE 1 RB + SLOSH PLUS 3 RB + SLOSH X 10 001
 3.0×10^{-02}

ACCELERATION (G) PER 1.0 FT/SEC GUST, G/FPS



PHASE ANGLE
(DEGREES)

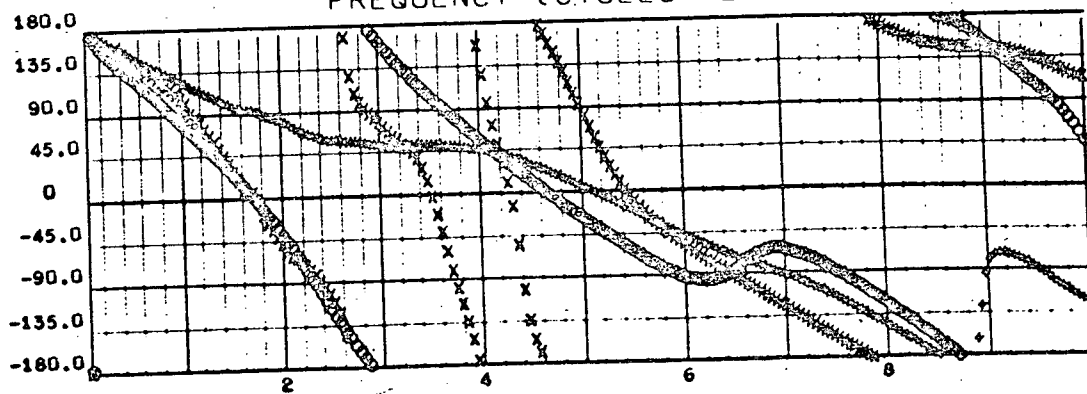


Figure 4-76. Ascent Flight Fuselage Lateral Acceleration Transfer Function (SAS On, Antisymmetric)

PL 2 ACC. AT I.S. 1150 CREW STATION
 CIRCLE 1 RB + SLOSH PLUS 3 RB + SLOSH X 10 001

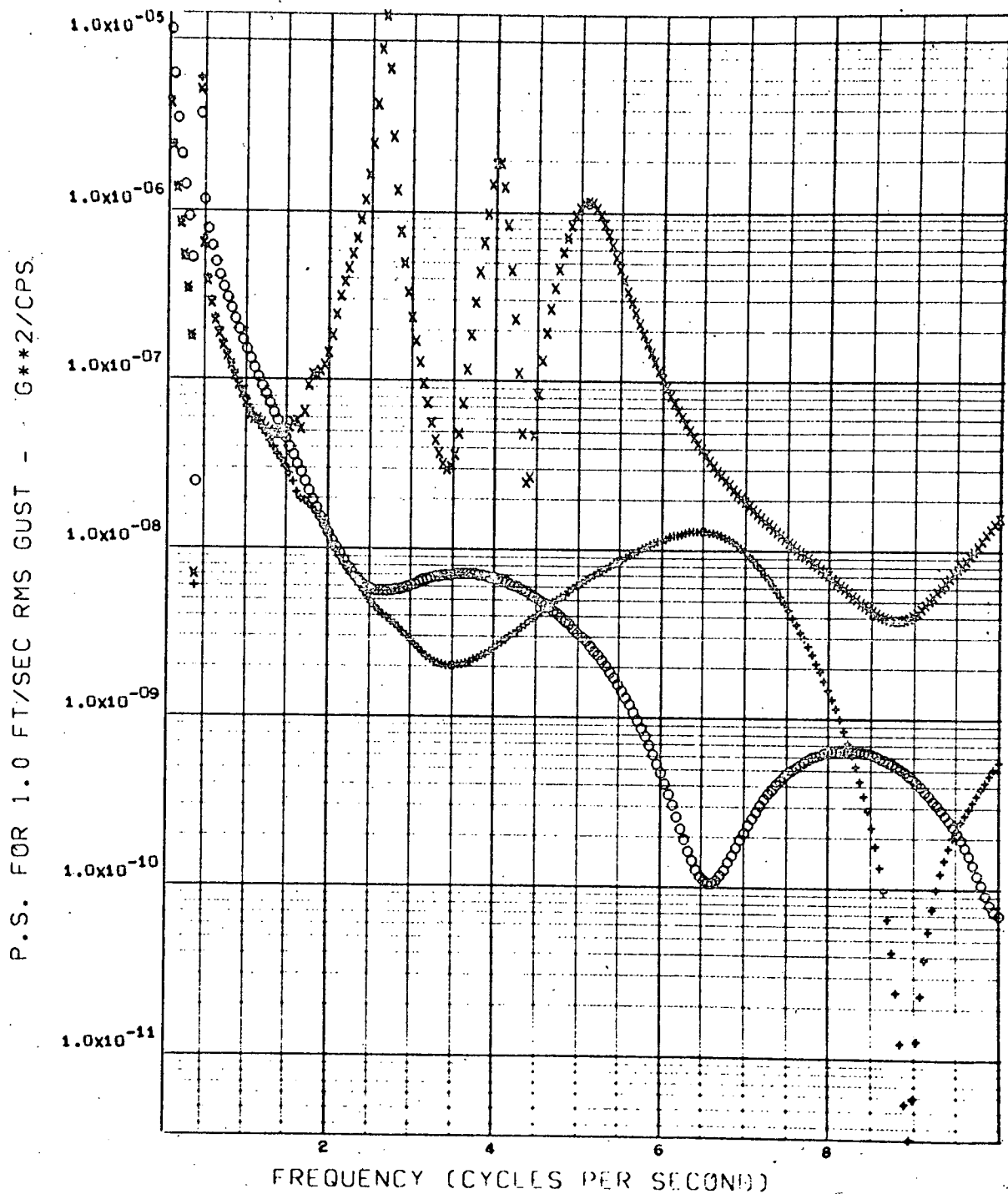


Figure 4-77. Ascent Flight Fuselage Lateral Acceleration
 PSD (SAS On, Antisymmetric)

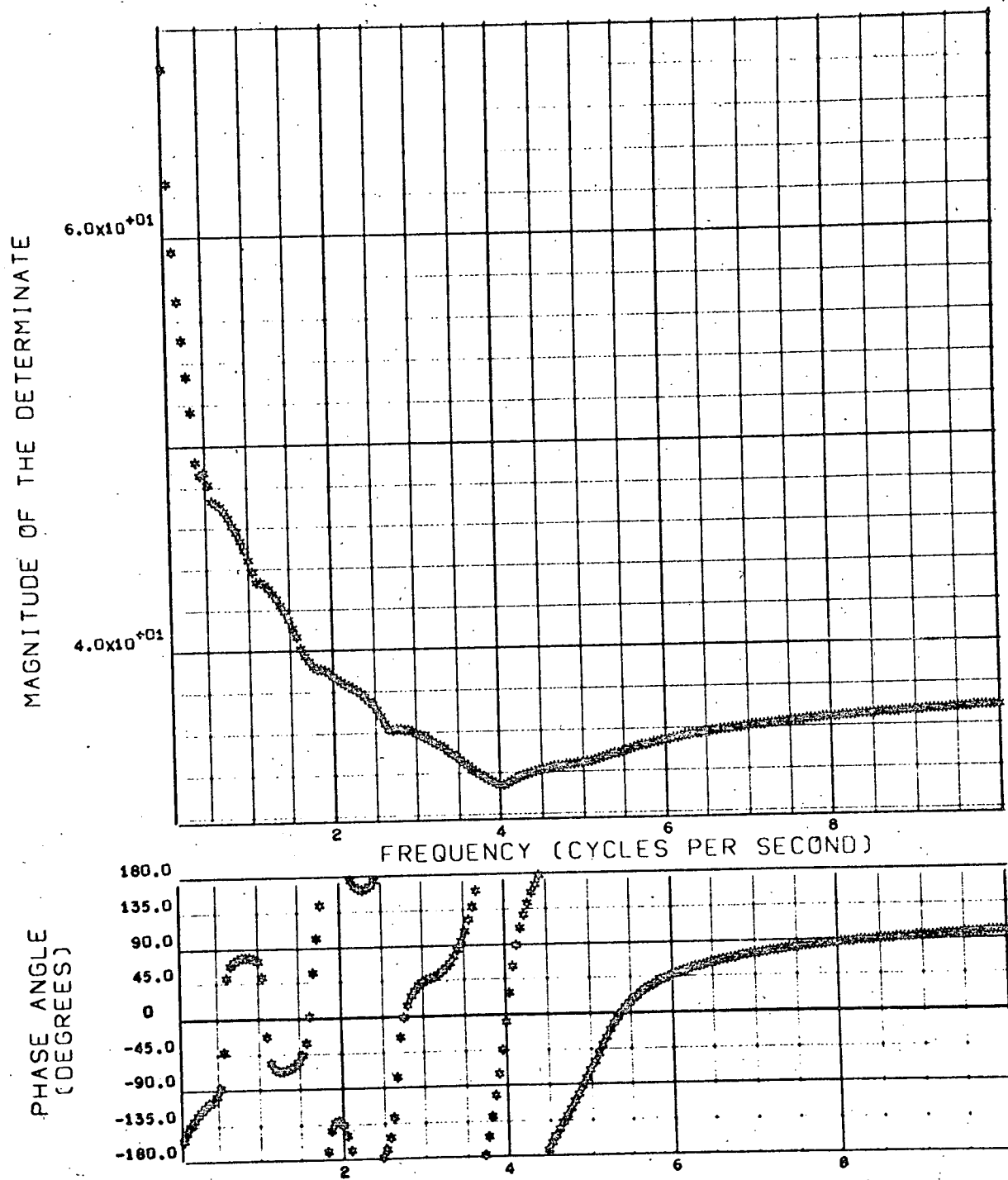


Figure 4-78. Ascent Flight A-Matrix Determinant Magnitude and Phase Angle (SAS On, Antisymmetric)

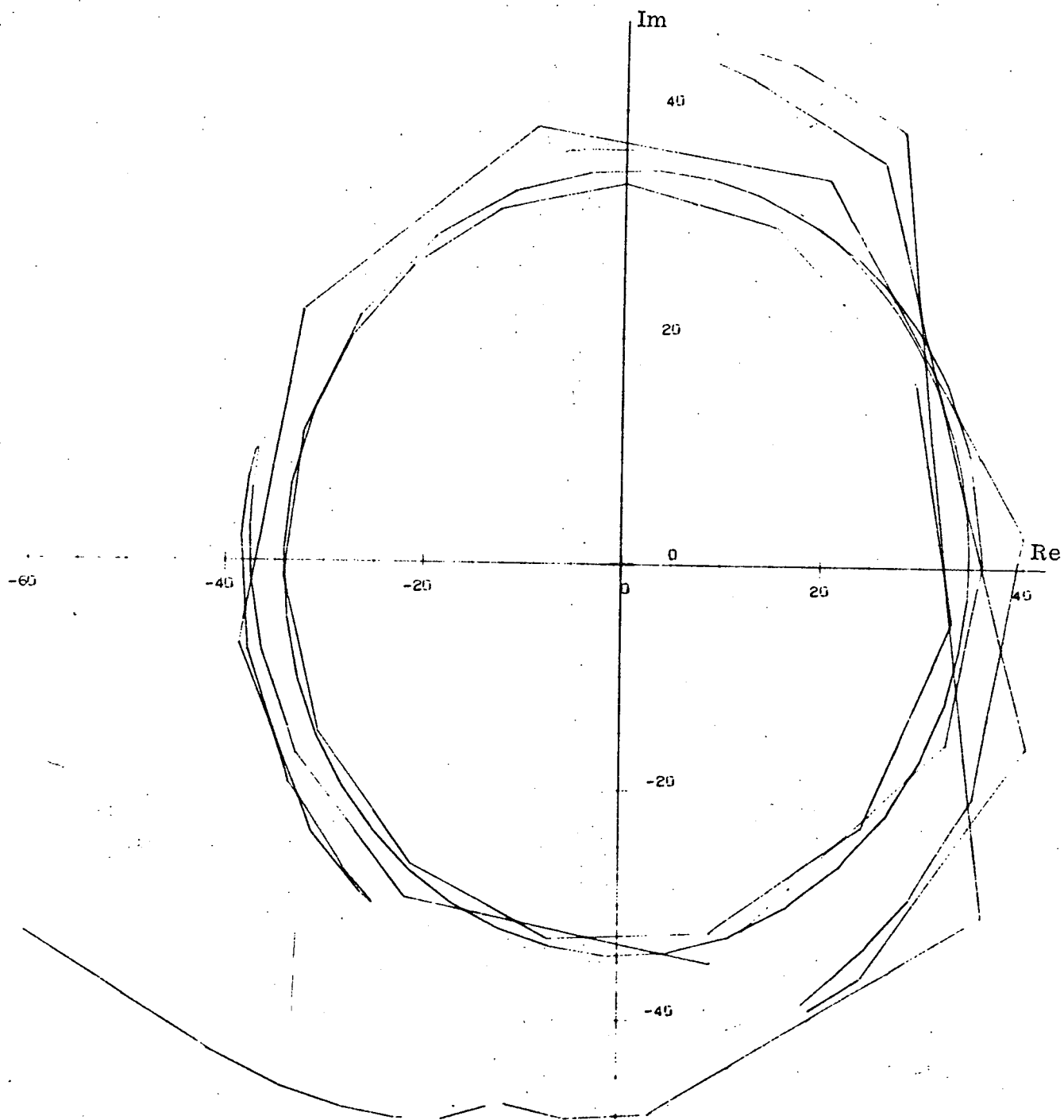


Figure 4-79. Ascent Flight A-Matrix Determinant Polar Plot (SAS On, Antisymmetric)

SECTION 5

CONCLUSIONS AND RECOMMENDATIONS

A computer program that can analyze the response of space shuttle to atmospheric turbulence has been developed and demonstrated. The method developed accounts for propellant slosh, gimbaled engine, and stability augmentation system (SAS) coupling with the rigid body and elastic modes of the mated or separated vehicles. Statistical outputs relating vehicle loads and accelerations to the level of random turbulence are generated. Time histories due to discrete disturbances can also be obtained.

By formulating the problem in the frequency domain, the capability is achieved to use any unsteady or quasi-steady aerodynamic theory based on harmonic motion for generating aerodynamic forces due to both the turbulence and the vehicle response. Gust penetration effects are accounted for. The quasi-steady aerodynamics approach based on the method of Woodward appears to have good potential for the space shuttle turbulence response problem because of its ability to account for aerodynamic interference and body flow effects. It is recommended that Woodward theory be applied in future space shuttle turbulence response studies.

Although load and acceleration responses calculated in the present analysis are well within vehicle design limits, the autopilot gains caused apparent instabilities that essentially invalidate the results of the SAS-on conditions. It is recommended that an elastic-vehicle/SAS-stability analysis precede the turbulence response calculated in future studies to ensure that autopilot parameters are realistic.

In the present analysis, only one ascent and one booster flyback flight condition were analyzed. This work should be extended to other flight times, concentrating on ascent flight where the complex aerodynamic and elastic problems are expected.

SECTION 6
REFERENCES

1. R. G. Huntington and R. L. Haller, A Method for Determining the Response of Space Shuttle to Atmospheric Turbulence - Volume II, Computer Program Description and Usage Instructions, Convair Aerospace Division of General Dynamics report GDC-71-006, December 1971.
2. Theodore Theodorsen, General Theory of Aerodynamic Instability and the Mechanism of Flutter, NACA report 496, 1935.
3. C. E. Watkins, H. L. Runyan, and D. S. Woolston, On the Kernel Function of the Integral Equation Relating the Lift and Downwash Distributions of Oscillating Finite Wings in Subsonic Flow, NACA report 1234, 1955.
4. E. Albano and W. P. Rodden, "A Doublet Lattice Method for Calculating Lift Distributions on Oscillating Surfaces in Subsonic Flows", AIAA paper No. 68-73, AIAA 6th Aerospace Sciences Meeting, New York, January 22-24, 1968.
5. T. E. Stenton and L. V. Andrew, Transonic Unsteady Aerodynamics for Planar Wings with Tailing Edge Control Surfaces, AFFDL-TR-67-180, August 1968.
6. Vincent W. Donato and Charles R. Huhn, Jr., Supersonic Unsteady Aerodynamics for Wings with Trailing Edge Control Surfaces and Folded Tips, AFFDL-TR-68-30, August 1968.
7. H. Ashley and G. Zartarian, "Piston Theory - A New Aerodynamic Tool for the Aeroelastician", Journal of the Aeronautical Sciences, Volume 23, No. 12, December 1956.
8. F. A. Woodward, "Analysis and Design of Wing-Body Combinations at Subsonic and Supersonic Speeds", Journal of Aircraft, Vol. V, No. 6, 1968.
9. E. Carson Yates, Jr., "Modified-Strip-Analysis Method for Predicting Wing Flutter at Subsonic to Hypersonic Speeds", Journal of Aircraft, Volume 3, No. 1, January - February 1966.
10. W. J. Brignac, and D. A. Shelton, "Quasi-Steady Supersonic Flutter Analysis of a Low Aspect Ratio Surface", paper presented at Aerospace Flutter and Dynamics Council Meeting, Dallas, Texas, 3 December 1970.
11. L. N. Lydick and F. W. Shelton, Correlation of Computer Procedure AT5 with B-58 Wind Tunnel Data, Convair Aerospace Division of General Dynamics report AIM No. 172, 17 March 1969.

12. D. O. Lomen, Analysis of Fluid Sloshing, Convair Aerospace Division of General Dynamics report GDC-DDE66-018, June 1966.
13. P. G. Waner, Jr., Analysis of Gust Alleviation Devices, Part I, Convair Aerospace Division of General Dynamics report ERR-FW-1018, 31 December 1969.